ANALYSIS OF

PROGRAMMABLE MOLECULAR ELECTRONIC SYSTEMS

A Dissertation

by

YUEFEI MA

Submitted to the Office of Graduate Studies of
Texas A&M University
in partial fulfillment of the requirements for the degree of

DOCTOR OF PHILOSOPHY

May 2006

Major Subject: Electrical Engineering

ANALYSIS OF

PROGRAMMABLE MOLECULAR ELECTRONIC SYSTEMS

A Dissertation

by

YUEFEI MA

Submitted to the Office of Graduate Studies of
Texas A&M University
in partial fulfillment of the requirements for the degree of

DOCTOR OF PHILOSOPHY

Approved by:

Chair of Committee,	Jorge Seminario
Committee Members,	Fred Strieter
	Christi Madsen
	Zhengdong Cheng
Head of Department,	Costas Georghiades

May 2006

Major Subject: Electrical Engineering

ABSTRACT

Analysis of Programmable Molecular Electronic Systems. (May 2006)

Yuefei Ma, B.S., Fudan University, China;

M.S., University of South Carolina

Chair of Advisory Committee: Dr. Jorge M. Seminario

The continuing scaling down in size of microelectronics devices has motivated the development of molecular electronic devices, often called moletronics, which use molecules to function as electronic devices. One of the moletronics is the programmable molecular array. In this device, disordered arrays of metallic islands are interlinked by molecules. It is addressed by a small number of input/output leads located on the periphery of the device.

In this dissertation, a thorough investigation of the programmable molecular array is performed. First, theoretical calculations for single molecules are carried out. The effect of bias voltage on the electron transmission through the molecule is reported. Next, electrical measurements are conducted on programmable molecular arrays. Negative differential resistance and memory phenomena are found. The electrical characteristics of the programmable molecular array populated with different molecules indicate that the metallic islands contribute to the above phenomena. The electrical

conductance through the metallic islands is investigated, and conformational change of the metallic islands under bias is reported.

Furthermore, a scenario is proposed to use molecular vibronics and electrostatic potential to transport and process signals inside the programmable molecular array. Simulated results are presented.

献给我的妈妈和爸爸

ACKNOWLEDGEMENTS

I would like, first, to express my great gratitude and deep appreciation to my advisor, Professor Jorge Seminario, for giving me this great opportunity to join in the research on this interesting topic and encouraging me all the time. The tremendous knowledge I gained from the research work will benefit me throughout my life.

I would also thank my PhD committee members, Dr. Fred Strieter, Dr. Christi Madsen, and Dr. Zhengdong Cheng, for contributing their brilliant ideas and expertise in this research.

In addition, I wish to express my special appreciation to Dr. Bob Biard who shared me with his profound knowledge about electrical engineering. I learned a lot from him.

A number of members in the Moletronics group have helped me out and offered their support. I would like to thank all of them. Particularly, I am very grateful to Dr. Liuming Yan, who gave me great support.

Finally, I want to thank my family and my friends, who provided me with deep love and unconditional support.

TABLE OF CONTENTS

Page

CHAPTER Page

LIST OF FIGURES

Figure Page

Figure Page

Figure Page

Figure Page

CHAPTER I

HIGH SPEED ELECTRONICS

In this chapter, the importance of high speed electronics is described, and the current status of microelectronics is explained. Then, the limitations faced by microelectronics due to device fabrication and physical limits are analyzed. Afterwards, challenging new techniques are described that may complement conventional microelectronics and permit the attainment of higher computing speed. Finally, the goals and objectives of this research work are stated.

1.1 Importance and current status of high-speed electronics

In 1965, only 7 years after Jack Kilby invented the integrated circuit, Gordon Moore made his famous observation popularly known as "Moore's Law".[1,2] Moore's law predicted that the number of transistors per integrated circuit, would double every 18 month, leading to exponential growth in the complexity of devices. Amazingly, this empirical rule is still holding true. The number of transistors in the 4004 processor was 2,250 in 1971. This number increased to 275,000 for the Intel386™ processor in 1985. By 2003, it grew to 410,000,000 in the Intel® Itanium® 2 processor. Then, on January 25th, 2006, Intel demonstrated a fully functional 45nm SRAM chip with more than a billion transistors.

This dissertation follows the style of *Journal of Physical Chemistry B.*

The fundamental driving force behind Moore's law is the constant craving for ultrafast computing. It is always said, "Time is money"; in fact time is everything. As the technology grows, the need for faster computation is demanded in many disciplines, such as mathematics, chemistry, physics, meteorology, etc. Faster computation facilitates the research and makes it more productive and efficient. It would be better to finish a computation in a shorter time, because it will shorten the time needed for feedback and thus for completion of a project. Also, faster computing means faster communication, which will bring people closer together, all around the world. In the meantime, the information being processed is growing exponentially, which requires a larger number of memory devices and faster speed to process and deliver all the information. All these computational and memory functions require more and more transistors in a smaller space. Thus, the sizes of transistors in a single chip shrink tremendously.

1.1.1 Limitations in device fabrication

The continuous growth resulting from following Moore's law on the other hand, creates obstacles in device fabrication in

- Lithography
- Doping

a. Lithography

Since the resolution of lithography depends on the wavelength of the light source, a light source with shorter wavelength is needed to create smaller images. New

techniques such as phase-shift masks and optical proximity correction make it possible to print smaller patterns than those normally expected from the wavelength of the light source. For example, currently, 193 nm light is used to produce a minimum feature size of 45 nm. However, the goal of feature sizes of 30 nm or less is still pushing us to seek new light sources with shorter wavelength. As researchers search for new light sources, technologies for improved photo resist, mask, and aligner system need to be developed simultaneously. Some alternatives have been found, such as E-beam and X-ray lithography, which can yield nano-sized features, but these alternatives are not suitable for mass production;[3] large scale production with feature sizes smaller than 45 nm is extremely difficult.

b. Doping

Semiconductor materials become conductive by adding certain impurities into the bulk. This process of doping is done by diffusion or ion implantation. Both processes face a limitation of solid solubility, meaning that the maximum number of impurity atoms that can exist in a solid is limited. Thus, as the size of the device is decreased, it might be possible in the future that only one or a few doping atoms will exist in the source/drain area, resulting in fuzzy boundaries and therefore bad performance.

1.1.2 Limitations in device operation

The building blocks of current electronic circuit are Complementary Metal Oxide Semiconductor (CMOS) Field Effect Transistors (FET), in which both NMOSs and

PMOSs are used to implement the logic functions. In NMOS, electrons are majority carriers in the channel region; while in PMOS, holes are majority carriers. According to the International Technology Roadmap for Semiconductors (ITRS), CMOS technology will still be around until 2015.[4] Even if some of the difficulties in device fabrication are overcome, there will still be a number of intractable issues in solid-state physics as follows:

- Velocity saturation in MOSFET
- Punch through
- Parasitic capacitance
- Gate leakage

a. Velocity saturation in MOSFET

The speed of carriers in a MOSFET is related to the mobility of the majority carriers in the channel, i.e., the electron/hole mobility. The mobility is inversely related to the lateral electric field across the channel.[5,6] As the device is scaled down, the electric field increases, which results in decreasing mobility. Therefore it restricts the MOSFET current and the speed of the device.[6]

b. Punch through

During normal operation, the current in a MOSFET is carried through the channel, which is induced by the voltage applied to the gate. However, if the device is scaled down so that the channel is extremely short, the depletion region of the drain expands, because of the application of the drain voltage. Eventually it will touch the

source depletion region. Thus, the electrons will "punch through" from the source to the drain, resulting in leakage current.[6]

c. Parasitic capacitance

As the device is scaled down, the surface-to-bulk ratio increases. This may increase the parasitic capacitance of the Gate-Drain capacitor, the Gate-Source capacitor, the Drain-Bulk capacitor, the Source-Bulk capacitor, etc. The general problem is that large capacitors decrease the speed of the device.[6]

d. Gate leakage

Scaling of the MOSFET results in an extremely thin gate oxide and due to the "uncertainty principle" between the velocity and the momentum of the electron, it is impossible to find an electron in an exact position.[7] As is predicted by quantum mechanics, electrons tunnel through the thin gate resulting in a reduced gate field. To maintain the same channel depth as well as the same channel current, larger voltages must be applied to the gate, which increase the power consumption.[6]

1.2 Future perspective of electronics

All these limitations urge us to search for new solutions for further expanding Moore's Law. Amazingly, three years before the publication of Moore's Law, Richard P. Feynman gave a talk "There is plenty of room at the bottom". He spoke about the problem of manipulating and controlling things on a small scale. This seminal talk laid the foundation for the development of nanotechnology and molecular electronics; thus, a number of possible solutions have been found for the end of the Silicon-era:

(a) Single molecular transistor

The fundamental idea behind the single molecular transistor is to use a single molecule to function as an electronic device. This will decrease the size of a device tremendously. Since the seminal paper describing a molecular rectifier was published in 1974,[8] the field of molecular electronics has grown rapidly. However, fine lithography remains as a limitation for its realization as single molecules need to be addressed precisely.

(b) Programmable molecular array

A programmable molecular array is a two-dimensional structure made of chemically arranged molecules. Microsized metallic input and output leads are located on the periphery of the structure. Thus, there are tens or hundreds of single molecular devices connected in series-parallel between input and output. This intriguing feature further shrinks the dimensions of devices. However, programmable molecular array has to be programmed by applying a sequence of voltage pulses on the metallic leads in order to perform specific post-fabrication functions.

(c) Use of molecular vibrational modes and molecular potential to transmit and process information

When an atom in a molecule is displaced, the displacement signal will be transmitted through the molecule by the molecular vibrational modes. It is similar to the case of a mass-and-spring system. Furthermore, the displacement introduces a change in

the distribution of the molecular electrostatic potential (MEP). By combining these two methods, the signals can be transmitted and processed without any electron current.

(d) Spintronics

Spintronics is a technology that uses electron spin (and sometimes the spin of the nucleus), instead of using electron charge to store and transfer information.[9,10] The spin can be detected as a weak magnetic energy state characterized as “spin up” or “spin-down”. Spintronics has been successfully applied to a device called a spin valve, which utilizes a layered structure made of thin films of magnetic materials to change the electrical resistance which depends on the direction of magnetic field being applied. Currently, researchers are developing new magnetic semiconductors based on room temperature ferromagnetism.

(e) Cross bar approach

In a cross bar structure, two layers of regularly arranged nanowires (or nanotubes) are crossing each other and are interconnected with electrically switchable molecules. By applying a sequence of voltage impulses to the nanowires and using switches of opposite polarities, the device can perform specific logic functions. In addition, it can restore a logic level in a circuit to its ideal voltage value, allowing a designer to chain many simple gates together to perform an arbitrary computation.

1.3 Goals and objectives

In order to build faster, more economical and denser computers, a programmable molecule array device has been proposed to complement the conventional silicon based

microelectronic devices. Several aspects of the implementation of the programmable molecule array are addressed in this research work as follows:

a. Single-molecule conductance

Since a molecule is the fundamental component of a programmable molecular array, the electrical characteristics of the molecule, especially the current-voltage characteristic, are the major design parameters for the programmable molecular array. Our group has previously demonstrated that a good "candidate" molecule should have a negative differential resistance. The study of electrical conductance in a single molecule has been reported in several papers.[11-16] Significant discrepancies have been found based on the observed phenomena.[16] Here, theoretical methods based on density functional theory (DFT) calculations will be used to precisely calculate the electrical conductance of the molecules.

b. Electrical characteristics of programmable molecular array

In order to implement the programmable molecular array into real circuits, the current-voltage characteristics and the transient behavior of the device need to be known. Memory and switching phenomena, start-up transitional behavior, and the effects of different molecular depositions as well as programmability are investigated in this work.

c. Electron transport through thin discontinuous metallic film

Since the proposed programmable molecular array is constructed on a thin discontinuous metallic film, the electrical characteristics of the film are of great interest. The reason is that at nano-scale, the behavior of the film may change radically compared

to the bulk material, i.e., a continuous thin film. The electron transport is studied both theoretically and experimentally.

d. Application of vibronics and molecular potential on programmable molecular arrays

To further solve the problems of power consumption and heat dissipation, transmission of a signal can be accomplished by molecular vibrational modes instead of electron charge transfer. In addition, molecular potentials can process signals transferred by vibronics. These two methods can be used together in programmable molecular arrays. The results of molecular simulation for signal transport and signal processing are reported. The feasibility of applying these methods to a programmable molecular array is also discussed.

CHAPTER II

SINGLE-MOLECULE ELECTRONICS TECHNIQUES

In this chapter, first a number of experimental techniques for molecule conductance measurements will be reviewed. Then, the theoretical method to calculate molecule conductance is explained in detail. And then the theoretical calculated results of the molecule OPE, including structure optimization, molecular orbitals and their energies, transmission function, density of states and current-voltage characteristics are presented. Finally, the calculated and experimental results are compared.

2.1 Review of molecule conductance measurement techniques

In order to allow today's microelectronics to further scale-down, molecules have been assembled into electronic circuits instead of the standard electronic devices. Several efforts have been carried out to measure the current-voltage characteristics of the molecules of interest. However, large discrepancies exist between the results from different groups.

The concept of using molecules as electronic devices is simple: one can connect a single molecule between metallic contacts and metal-molecule-metal junction is formed. However, it is rather difficult to implement them because of the small size of the molecule. Fortunately, in recent years numerous seeding research investigations have developed methods to electrically measure the single molecule conductance.

2.1.1 Scanning tunneling microscope

Scanning tunneling microscope (STM) provides a straightforward approach to measure single-molecule conductance. By monitoring the tunneling current between the STM probe tip and the substrate, and properly adjusting the distance between the probe tip and the substrate, the nano-sized probe tip is manipulated to make contact with a monolayer of molecules sitting on a conducting substrate. Thus electrical measurement could be conducted.[13,17-22] To further isolate the single molecule, the molecule of interest is "inserted" into a monolayer of insulating molecules.[23,24] Nano-sized gold particles are also attached to the monolayer to make better contact for the STM probe tip.[14,25,26]

2.1.2 Break junction

To achieve relatively stable contacts, Reed et al. proposed break-junction contacts to probe the molecular conductivity.[27] In this method, the metal wire is mounted on a flexible substrate and is broken by mechanically bending the substrate. Subsequently, the molecules of interest are self-assembled onto the formed metal electrodes. Thus a metal-molecule-metal junction is formed and the electrical measurement was performed.[27] Park et al. developed an approach to electrically "break" the metal wire by a controlled passage of current. Thus a nano-sized gap is achieved.[28] They performed an experiment to form the junction after the molecules were self-assembled onto the metal wire and electrical characteristics were obtained.[12,29]

2.1.3 Mercury drop electrode

Electrical measurements have also been conducted on mercury drop electrodes. In one of the methods, a monolayer of molecule 1 is self-assembled on to a small drop of mercury. Then the molecule covered mercury drop is manipulated to gently contact with a planar gold electrode which has a self-assembled monolayer (SAM) of molecule 2. Thus a Au-SAM(1)//SAM(2)-Hg junction is formed.[30-33] Notice that van der Waals interactions exist between the terminal groups of the two molecules. In another method, two mercury drops were driven micrometrically to contact each other.[34]

2.1.4 NanoPore

Standard semiconductor device fabrication techniques have been extensively utilized to measure the electrical conductance through single molecules. Reed et al. proposed a device structure in which a nano-sized pore is formed in a silicon wafer using the lithography and reactive ion etching techniques. A gold contact is evaporated on one side of the nanopore, in which the molecules are self-assembled onto the gold. Then gold is evaporated on the other side of the nanopore in a cooling stage. Thus an Au-molecule-Au junction is formed.[35-40]

2.1.5 In-wire junctions

The metal electrode also can be fabricated after the deposition of molecules. In the in-wire junction approach, molecules are self-assembled on one end of a gold nanowire, which is deposited on a membrane substrate. The other electrode is electrodeposited on the molecules.[15,41,42] The formed in-wire junctions are isolated from

the membrane substrate and assembled onto a lithographically patterned testing structure using an AC electric field.[16,43]

2.2 Theoretical calculation of single molecule conductance

Besides the large disparities in conductivities reported for identical[11,44] or similar[27,45] molecules, some other questions are also a subject for debate. It is hard to tell which experimental method is superior to correctly provide the information of electron transport through single molecules.

In quantum mechanics, the state of a molecular system is described by wave function $\Psi(\vec{r},t)$, which is function of particle coordinates $\vec{r}$ and time t. For a one-particle, one-dimensional system, the change of wave function with time can be found by solving time-dependent Schrödinger equation

$$i\hbar\frac{\partial\Psi(\vec{r},t)}{\partial t}=\hat{H}\Psi(\vec{r},t) \tag{2.1}$$

in which $\vec{H}$ is the Hamiltonian operator, which acts on the state space and can be written as

$$\hat{H}=-\frac{\hbar^2}{2m}\nabla^2+\vec{V}(\vec{r},t) \tag{2.2}$$

where the constant $\hbar$ is defined as $\hbar=h/2\pi$, h is the Planck constant, m is the mass of the particle, and $\vec{V}(\vec{r},t)$ is the potential energy function of the system.

Unlike the states of a classical-mechanical system, the wave function $\Psi(x,t)$ can not provide definite responses because of the uncertainty principle. However, it gives the probability P at time t of finding the particle in the region in a region dx

$$P = |\Psi(x,t)|^2 dx \tag{2.3}$$

where the square of the function $|\Psi(x,t)|^2$ is the probability density.

Before calculating the electron transmission characteristics of the molecule, a geometry optimization is performed to find the most stable structure for the molecule. In this step, the geometry will be adjusted until a stationary point on the potential surface is found. Kohn-Sham density functional theory (KS-DFT) techniques as implemented in Gaussian 03 program are used to calculate the molecular and electronic structures. DFT does not attempt to calculate the molecular wave function, but it calculates the molecular electron probability density and molecular electronic energy from the molecular electron probability density.

The electron transmission characteristics of the molecule are calculated using the Green function approach based on quantum transport theory. The effect of the external voltage applied to the molecule is implemented as an external field applied in the direction along the molecule. The details of the calculation process are explained by Seminario et al.[46-49] The system under calculation consists of a molecule, and two metal contacts. Thus the Hamiltonian for the molecular device $\hat{H}device$ is the sum of the Hamiltonians of the $\hat{H}molecule$, the left contact $\hat{H}_L$, the right contact $\hat{H}_R$, coupling

between the molecule and the left contact $\hat{H}_{ML}$ and coupling between the molecule and the right contact $\hat{H}_{MR}$.

The effect from the terminals is represented by a self-energy term $\Sigma_j(j=1,2)$. Therefore the Hamiltonian of the molecular device is written as

$$\hat{H}device = \hat{H}_{MM} + \Sigma_1 + \Sigma_2 \tag{2.4}$$

The $\hat{H}_{MM}$ is the Hamiltonian submatrix of the molecule. The Green function for the molecular device is

$$\vec{G}_M = \left[EI - \hat{H}device\right]^{-1} \tag{2.5}$$

From the Green function, the electron transmission function can be obtained based on

$$T(E) = \frac{1}{N} tr\left(\Gamma_1 G_M \Gamma_2 G_M^+\right) \tag{2.6}$$

and the density of states (DOS) of the molecular device can also be obtained

$$DOS = tr\left[i\left(G_M - G_M^+\right)\right] \tag{2.7}$$

where $\Gamma_j = i\left(\Sigma_j - \Sigma_j^+\right)(j=1,2)$ is the imaginary part of the self-energy Σ_j, G_M^+ is the adjoint of G_M, and N is the number of atomic basis sets.

The current as a function of the external bias is obtained according to the Landauer-Büttiker equation:

$$I(V) = \frac{2e}{h}\int_{-\infty}^{\infty} T(E,V)\left[f_1(E,V_1) - f_2(E,V_2)\right]dE \tag{2.8}$$

where $f_j(E,V_j)$ is the Fermi function, V_1 and V_2 are the electric potentials of the terminal.

Using the Gaussian 03 program, the effect of the bias electric field on the molecule is evaluated by a series ab initio calculations with different electric fields applied to the molecule. Next the DOS for bulk Au is calculated using Crystal 98 program, thus the self-energy is obtained. Then a series of Green functions corresponding to different applied electric fields are calculated, and finally, the DOS, electron transport probabilities, and current-voltage characteristics of the entire molecular system are calculated using the Green functions.

2.3 Results of theoretical calculation of the OPE

Since the molecule 4,4'-(diethynylphenyl)-2'-nitro-1-benzenethioacetyl, which belongs to the mononitrooligo (phenylene ethynylene) (OPE) is of great interested in the field of molecular electronics ever since its successful synthesis by Tour et al. Several publications have shown the experimental measured current voltage characteristics of the molecule. Nevertheless, not any two of them agree with each other. Therefore, it is necessary to seek the correct results.

2.3.1 Structure optimization

The electronic structure of the molecule is optimized using the Becke three-parameter hybrid exchange function with the Perdew-Wang correlation function (B3PW91). The geometry is first optimized using LANL2DZ basis sets and effective

core potential. Then a larger basis set is used – the 6-31G (d, p) basis set for H, C, N, S and O atoms. The optimized geometry is shown in Figure 2.1b and c.

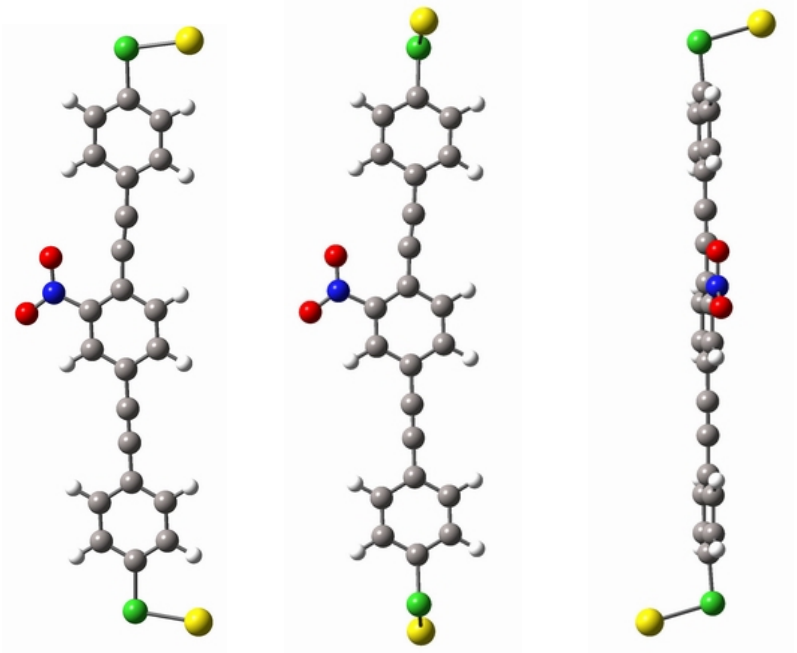

Figure 2.1. Molecular structure before optimization. (a) and after optimization, front view (b) and the side (c).

2.3.2 Transmission function and density of states

The density of states, electron transport probability and current-voltage characteristics are calculated using Green function methods.

Any molecule contains atoms and electrons. Sometimes, it is not possible to accurately determine the position of the electron, but it is possible to calculate the probability of finding the electron at any point around the nucleus. This fixed spatial

distribution around the molecule is molecular orbital. Solutions of the wave equations in three-dimensions allow calculation of the "shape" of each orbital.

Figure 2.2 shows the DOS, transmission function, as well as the molecular orbitals of the OPE when no electric field is applied. The gap between the highest occupied molecular orbital (HOMO) and the lowest unoccupied molecular orbital (LUMO) is 2.58 eV. The HOMO is closer to the Fermi level (E_F) of the crystalline Au, -5.31 eV, than the LUMO.

The contribution of each molecular orbital to the electron transport characteristics depends on two factors. First is the shape of the molecular orbital. Localized molecular orbitals are less conducting than delocalized ones. Second is its distance to the Fermi level in energy. The threshold for conduction directly depends on the energy separation from the conducting molecular orbitals to the E_F of the contacts. If the energy of a delocalized molecule orbital is far away from the Fermi level, then electrons need to overcome a large barrier to transport through the molecular orbital. In most cases, the molecule would be destroyed by high voltage applied onto it before such molecular orbital contributes to the electron transport.

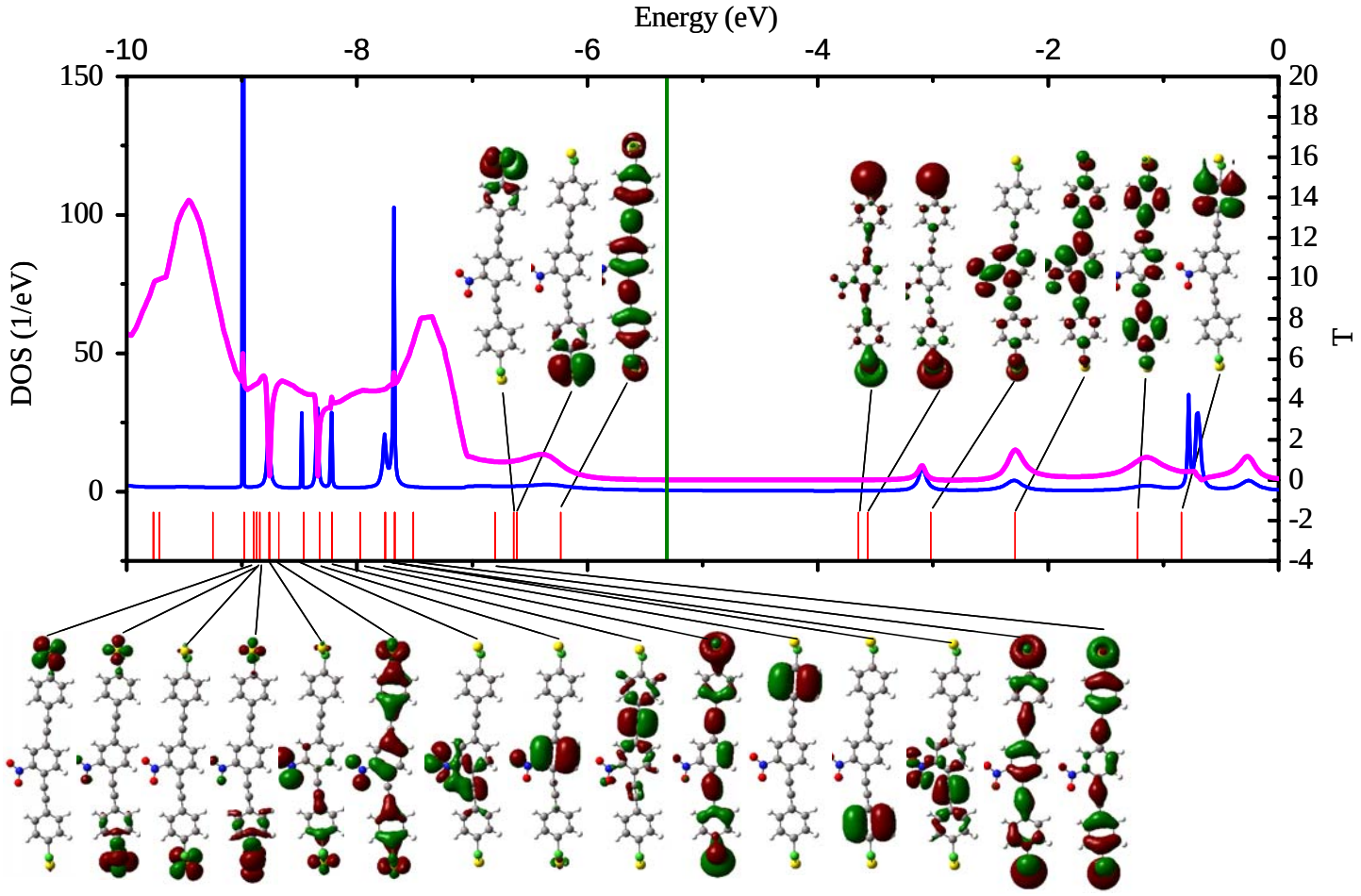

Figure 2.2. Density of states (blue) and transmission function (purple) of the molecule OPE when no electric field is applied. The molecular orbital and electronic states (red) are also plotted. The Fermi energy of gold (green) is shown as a reference.

In the case of the OPE molecule, as shown in Figure 2.2, the HOMO of the OPE is the closest to the E_F of gold. It is the first level to be reached by electrons from the contacts as the applied bias voltage increases. Thus, the shape of the HOMO determines the conduction of OPE at low voltages. From Figure 2.2, the HOMO is delocalized. Thus there is a local maximum in the transmission function.

2.3.3 Effect of the bias voltage on electron transmission function

A bias voltage from 0.00 V to 3.37 V is applied to the OPE molecule. During the field calculation, the geometry of the molecule is kept the same the one without field. Figure 2.3 shows the transmission function of the OPE for bias voltages in the range of 0 ~ 3.4 V. The shape of the transmission function remains similar for all the bias. However, as the bias increase, the curve shifts to lower energy and the peak which is originally located at -7.4 V for zero bias raises. From Equation (2.8), the current at a given voltage V is the integral of the transmission function in an energy range of eV centered at E_F (-5.31 eV) for gold. Thus, the current gradually increases with applying voltage.

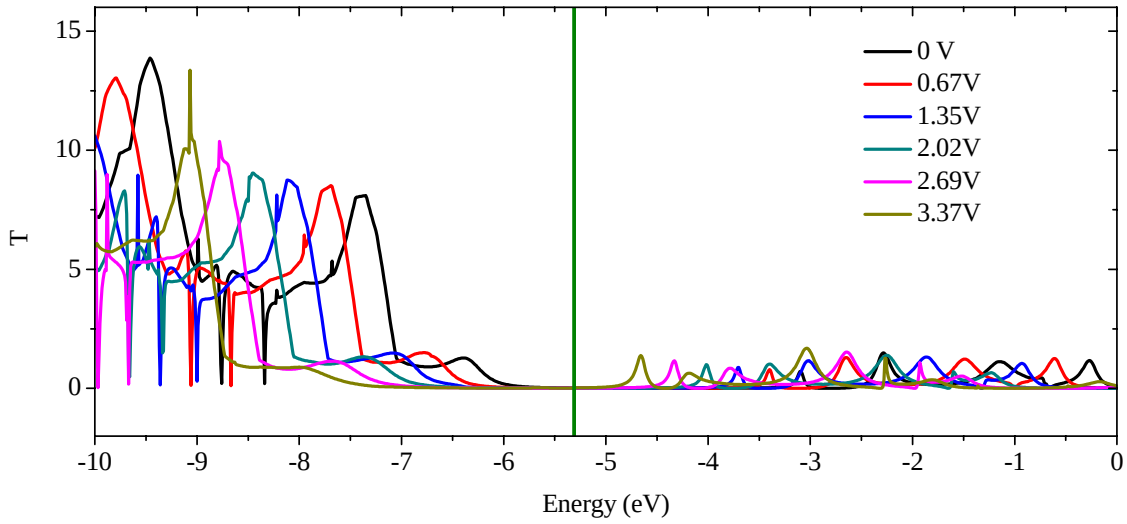

Figure 2.3. Transmission function versus energy of incoming electrons at several bias voltages for the OPE.

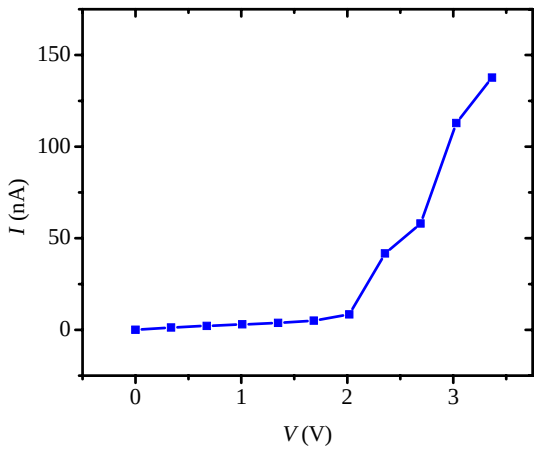

Figure 2.4. Theoretical current-voltage characteristics of the OPE molecule.

Figure 2.5 shows the bias dependence of energy levels of molecular orbitals. Similar to the transmission function, as bias voltage increase, both HOMO and LUMO

shift to lower energies. Interestingly, at 2.02 V, the LUMO is so low that it crosses the Fermi level which may results in a sudden reduce of the barrier for electron transport, thus the current increases tremendously, as shown in Figure 2.4.

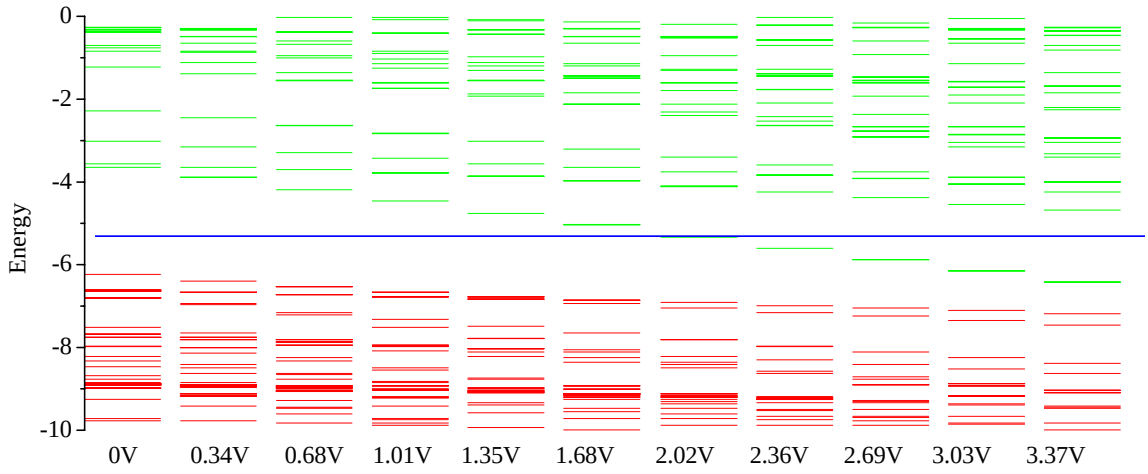

Figure 2.5. Bias dependence of energy levels of molecular orbitals. The green bars are unoccupied molecular orbital and the red bars are occupied molecular orbitals. The blue line indicates the location of Fermi energy level.

2.4 Possible reason for the discrepencies between theoretical and experimental results

Figure 2.6a shows the experimentally measured I-V curves at 10 K for an in-wire junction (solid black) and for a break junction (red) comprising OPE molecules. For comparison, the theoretical calculated result is fitted into the plot as the blue curve Obviously, the current of the break junction is 20 times larger than the theoretical obtained value in high voltage region. This is reasonable as we investigate the structure

of the break junction. It is possible that 20 molecules instead of 1 molecule are bridging the gold contacts and the single molecule conductance is 20 times smaller than the 20 molecules connected in parallel.

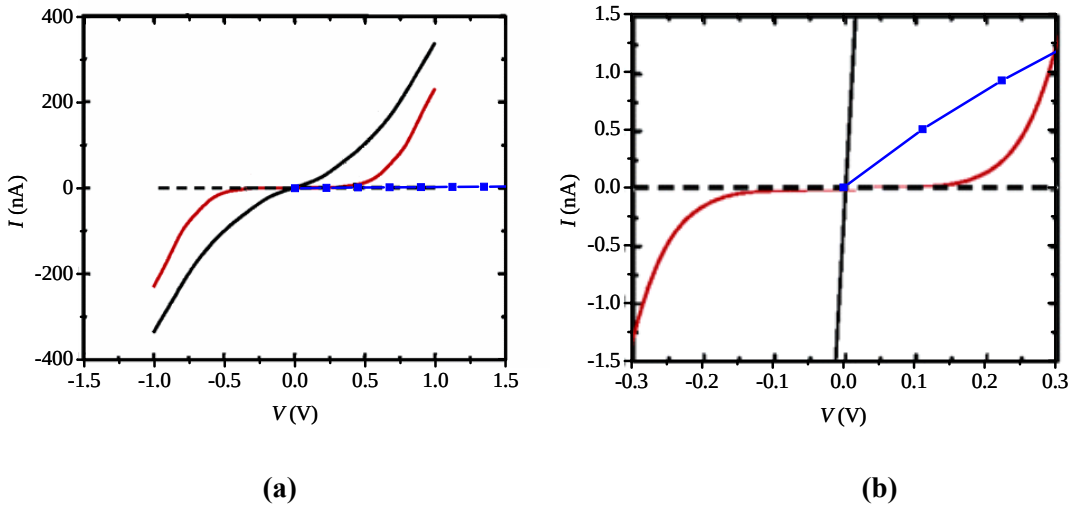

Figure 2.6. Comparison between theoretical and experimental current-voltage characteristics. The experimental values are obtained by Selzer et al.[16] (a) Bias voltage from -1.5 V to 1.5 V. (b) An expanded view of the -0.3 to 0.3 V range.

CHAPTER III

PROGRAMMABLE MOLECULAR ARRAYS*

In this chapter, first the programmable molecular array will be introduced. Next, related research work in other research groups are reviewed. Then, the fabrication process of the programmable molecular array as well as the process of forming self-assembled monolayers will be explained. And then, the electrical measurement set-up is described. Last, the electrical characterization of memory and switching phenomena, start-up transitional behavior, effect of different molecular depositions, and programmability of the device are investigated.

3.1 Introduction to programmable molecular arrays

As conventional silicon based microelectronics encounters more and more challenges when it scales down to smaller sizes, several companies and research groups are trying to incorporate single or small groups of molecules into electronic circuits. These molecules are expected to implement complex computations, for example, logic gates, memories and etc. By doing so, the size of a rather complicated circuit can be greatly reduced, and at the meantime it will bring down the fabrication cost.

---

* Part of this chapter is reprinted with permission from Jorge M. Seminario, Yuefei Ma, Luis A. Agapito, Liuming Yan, Roy A. Araujo, Sridhar Bingi, Nagendra, S. Vadlamani, Krishna Chagarlamudi, Tangali S. Sudarshan, Michael L. Myrick, Paula E. Colavita, Paul D. Franzon, David P. Nackashi, Long Cheng, Yuxing Yao, and James M. Tour, ***Clustering Effects on Discontinuous Gold Film NanoCells,*** J.Nanosci. Nanotechnol., Vol. 4, pp.907-917 (2004)..

However, to address a single molecule is another challenge for conventional fabrication techniques, especially lithography. This is the reason why molecular programmability has been proposed.[50-53] A programmable molecular array can also be called a molecular random access memory cell or nanoCell. It is a two-dimensional structure constructed on an insulator, e.g., SiO_2. Inside a nanoCell, there are chemically organized molecules and metallic nanoclusters, nanowires and/or nanotubes, as shown in Figure 3.1. The nanowires or nanotubes serve as anchors to attach the molecules by self assembled monolayer techniques. They can also conduct electrical current. Microsized metal leads are located on the periphery of the 2-D structure to allow the interconnection between the molecules and external circuit. It has been shown theoretically that some molecules can function as electronic device.[54-57] Therefore, the nanoCell can be viewed as hundreds of devices connecting any of the two contacts in series-parallel. After fabrication, the nanoCell will be programmed by a computer program to function as the purpose of desired device.

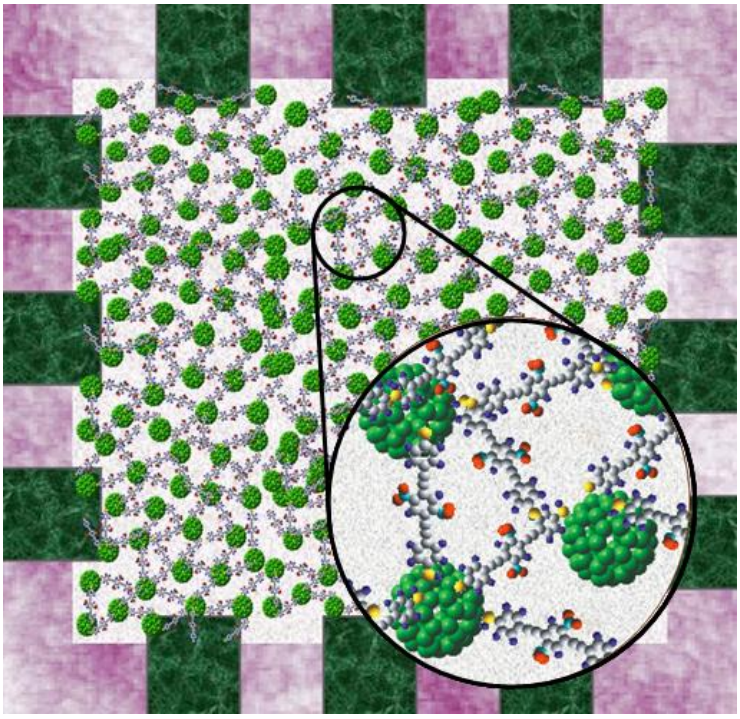

Figure 3.1. Schematic of a nanoCell composed of gold clusters (green) and interlinking molecules (grey) sitting on a substrate of SiO_2 (white). The electrodes (green) are located around the nanoCell. [58]

The advantage of a nanoCell is to relieve the painful fabrication process, especially for photolithography which currently can not fabricate features at molecular size. The smallest feature in a nanoCell that needs to be defined by photolithography is the metal lead. Except for this, the components of a nanoCell are chemically located. Since the structure of a nanoCell is mainly made of molecules, it also has the advantage of reducing power consumption and heat dissipation. In addition, it allows the device to be advanced in the future to conquer the physical and technical limitations of silicon-based electronics.

3.2 Related research work at USC, Yale, PSU and RICE

The programmable molecular array was originally proposed by a group of researchers from University of South Carolina (USC), Yale University, and Penn State University (PSU).[50] The preliminary idea is to chemically place the molecules inside a box and address them by using an external electrical field. The simulation conducted by Seminario et al. shows that the nanoCell can function as logic device and can be programmable after fabrication.[54] The first two-dimensional nanoCell was fabricated by Tour and Franzon.[53,59] Since it is almost impossible for the molecules to lie parallel to the substrate surface and to interconnect each other, a discontinuous gold film is vapor deposited inside the box.[59] Molecules are then self-assembled onto the gold islands through which the molecules are interconnected. To enhance conductance, molecules covered by nanowires are assembled onto the surface after being deposited.[53] The first molecule being deposited onto the nanoCell was mononitro OligoPhenylene Ethynylene (OPE). It exhibits Negative Differential Resistance (NDR) between Au probes both experimentally and theoretically.[55,60,61] The NDR is believed to be essential to obtain switching effects.[52,62] The current-voltage characteristics of OPE deposited nanoCell were studied and reported. Switching effects and memory effects have been demonstrated in the device.

At the same time, Husband et al. addressed the issue relating to programming the nanoCell to perform specific functions.[52,62] In a computer simulation, they were able to program a nanoCell into a half adder. However, successfully programming a nanoCell in real experiments has never been reported.

3.3 Sample fabrication

The first nanoCell substrate (Figure 3.2) was fabricated by researchers at North Carolina State University (NCSU). As shown in Figure 3.2, instead of metallic nanoclusters, a discontinuous gold film is deposited onto the p-type Si substrate uniformly covered with wet thermally grown SiO_2.[59] The thickness of the SiO_2 film is 1000 Å. The patterning of the discontinuous gold film is performed using a lift-off technique. In this technique, a layer of photoresist is deposit onto the substrate and a lithography process is used to define the pattern. Afterward, a discontinuous gold film is vapor deposited in high vacuum (~10^{-10} torr). During the deposition, the substrate temperature is maintained at 100 ^{o}C in order to increase the stability of the film. Standard silicon process techniques are utilized to fabricate the contact leads and contact pads.

According to the scanning electron microscope (SEM) image (Figure 3.3), the diameter of the gold islands ranges from 5 nm to 60nm and the separation between the islands is around 5 nm, which is sufficiently small to fit two molecules. Atomic force microscope (AFM) shows that the thickness of the film ranges from 3 nm to 4 nm in Figure 3.4. However because the AFM tip might be larger than or about the same size as the gap between the gold islands, the tip might not touch the substrate when it scans through the device. So, the thickness of the gold film might be larger than 4 nm.

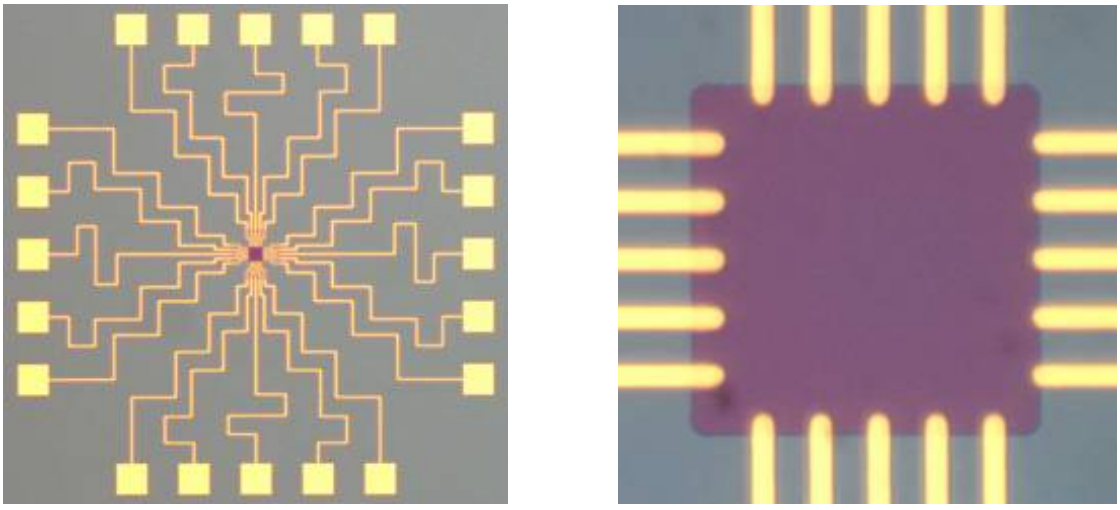

(a) **(b)**

Figure 3.2. Optical microscopic images of an experimentally constructed nanoCell. (a) Optical microscope image of a nanoCell. The yellow squares are contact pads. The purple square in the middle is a discontinuous gold film. The meander lines are contact leads. (b) Enlarged view of a discontinuous gold film.

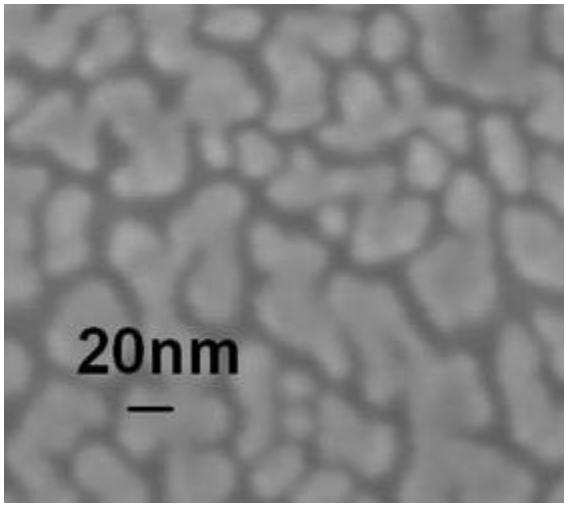

Figure 3.3 Scanning electron microscope image of a discontinuous gold film

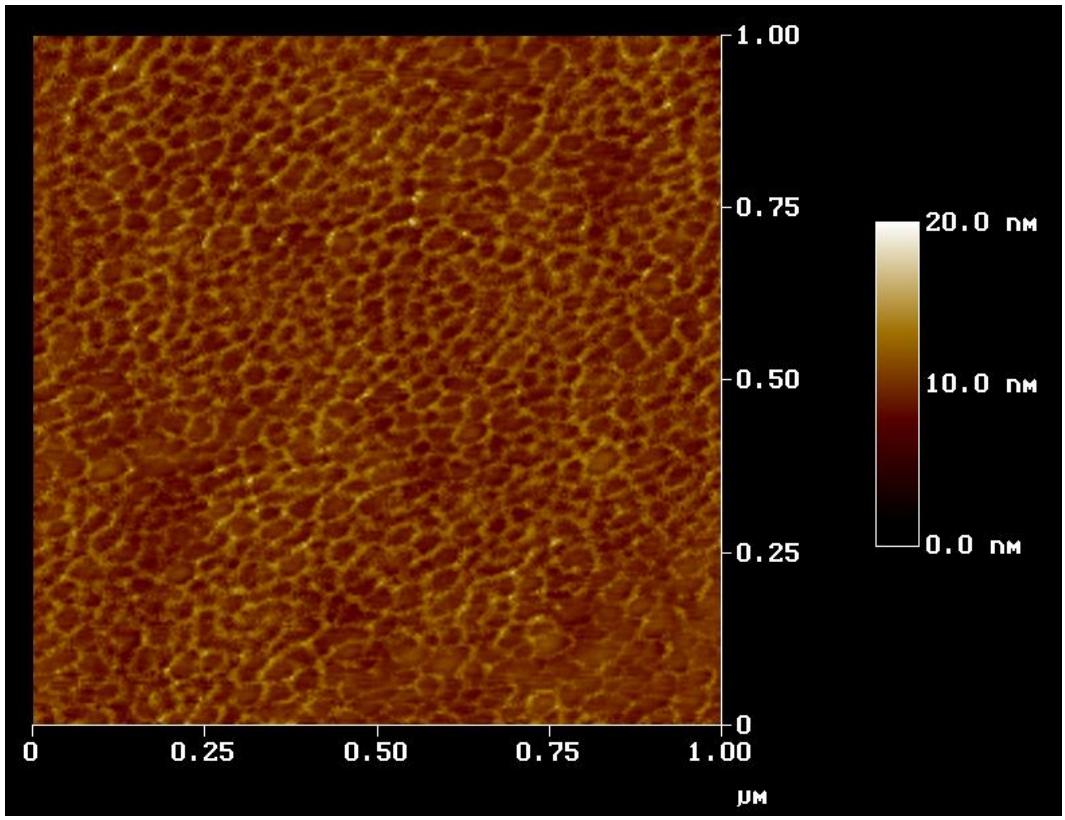

(a)

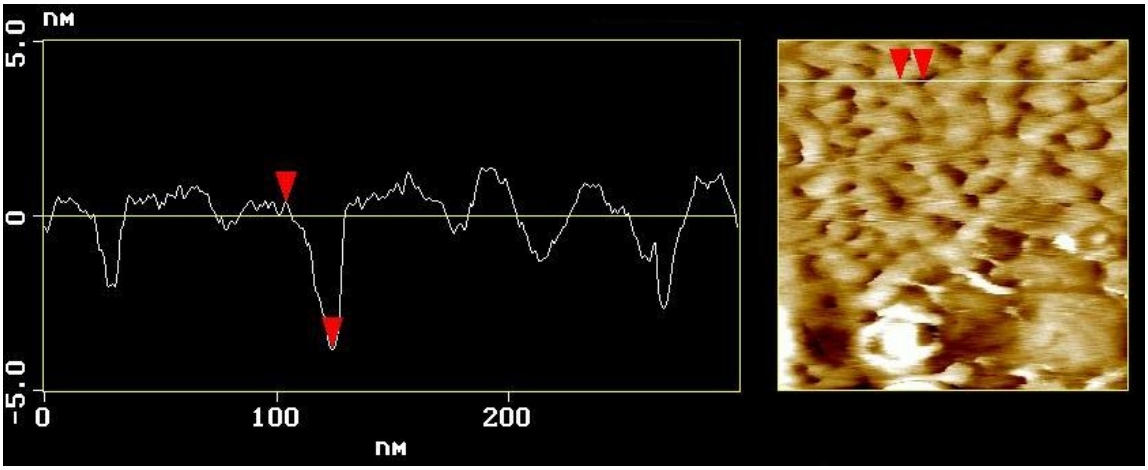

(b)

Figure 3.4. Atomic force microscope image of a discontinuous gold film. (a) Top-view; (c) ross-section analysis of the gold film.

3.4 Formation of self-assembled monolayers on nanoCell

Two kinds of molecules were chosen separately to deposit on different chips. Molecule **1**, as shown in Figure 3.5a, is 4,4'-(diethynylphenyl)-2'-nitro-1-benzenethioacetyl, which belongs to the mononitro oligo (phenylene ethynylene) (OPE) group. The molecule is a three benzene-ring oligomer with two nitro group (NO_2) substituents in the central ring. Sulfur atoms acting as "alligator clips" join one end of the molecular devices with the Au clusters. Electrical properties of the molecule have been studied both experimentally and theoretically. The study shows that the molecule yields negative differential resistance (NDR) which makes it a potential molecular electronic device.[60,61] This is the reason why this molecule has been chosen for this research work. The molecule is synthesized by Tour's group in Rice.[60] The acetyl group is used to protect the molecule against reaction with oxygen during transportation and it is removed in situ during the self-assembly process under acid conditions (CH_2Cl_2/MeOH/H_2SO_4), which is reported to yield better results than the traditional NH_4OH/THF mixture.[63] Once the acetyl group is removed, the S^- ion will attach to the Au atoms, resulting in a self assembled monolayer (SAM).

Molecule **2**, as shown in Figure 3.5b, is octyltrichlorosilane, which self-assembles on SiO_2.[64] The adsorption of the molecule onto the SiO_2 substrate takes place through the hydrolysis of the Si-Cl bonds to form Si-OH groups which interact with OH groups on the SiO_2 surface and form Si-O-Si bonds. Electronic transports through alkanethiol SAMs.

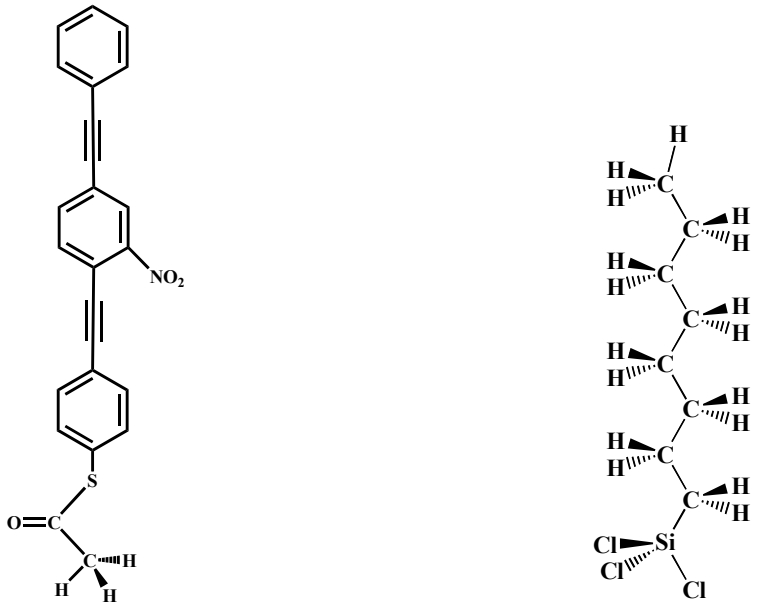

(a) **(b)**

Figure 3.5. Molecules used for self assembling on the chips. (a) Molecule 1 generates the 4,4'-(diethynylphenyl)-2'-nitro-1-benzenethiolate during self-assembly wherein the acetyl group (-COCH3) is cleaved and the sulfur attaches to the gold islands. (b) Molecule 2 is the octyltrichlorosilane. During the self-assembly process, the three chlorine atoms are displaced by surface hydroxyls on the SiO2 substrate.

Two different self-assembly procedures are performed at room temperature. Before the self-assembly, the nanoCell chip is cleaned using methanol and acetone, then rinsed with distilled water and dried by using nitrogen gas. For self-assembling molecule **1**, 1 mM of molecule **1** is added to a solvent composed of methylene dichloride and methanol (2:1) is prepared. The nanoCell chip is soaked for approximately 12 hours in the solution. During the reaction, the acetyl group at the end of the molecule **1** is cleaved and then reacts with the gold surface, forming self-assembled monolayers (SAMs). Finally, it is rinsed by methanol to stop the reaction and dried by nitrogen gas.

For self-assembling 2, the nanoCell chip is soaked for 12 hours in 1% toluene solution. During the reaction, the three chlorine atoms are displaced by surface hydroxyls on the SiO_2 substrate. Thus the molecules are self-assembled on the SiO_2 surface. It is then rinsed by methanol and dried by nitrogen gas.

3.5 Measurement set-up

The nanoCell devices are measured in a probe station (Lakeshore Cryogenic probe station). Since the system being tested involves nanoscale features, such as molecules and gold islands, any free particles in the ambient environment might interfere with the normal operation of the system. In order to exclude this environmental influence, the sample is placed inside a high vacuum (about 10^{-7} torr) chamber (Figure 3.6) during the measurement.

The temperature of the sample stage inside the vacuum chamber can be reduced by a continuous flow of liquid nitrogen, which is pumped out from a nitrogen dewar by a flow of nitrogen gas. A temperature sensor is attached to the sample holder inside the vacuum chamber. The other end of the temperature sensor is connected to a temperature controller. Users could input the set point of the desired temperature and the temperature controller calculated the output power of a heater, which is located at the chamber wall, based on the difference between the desired and the current temperature. Thus the temperature gradually approaches the set point. In this chapter, the nanoCell devices are analyzed at room temperature (297 K).

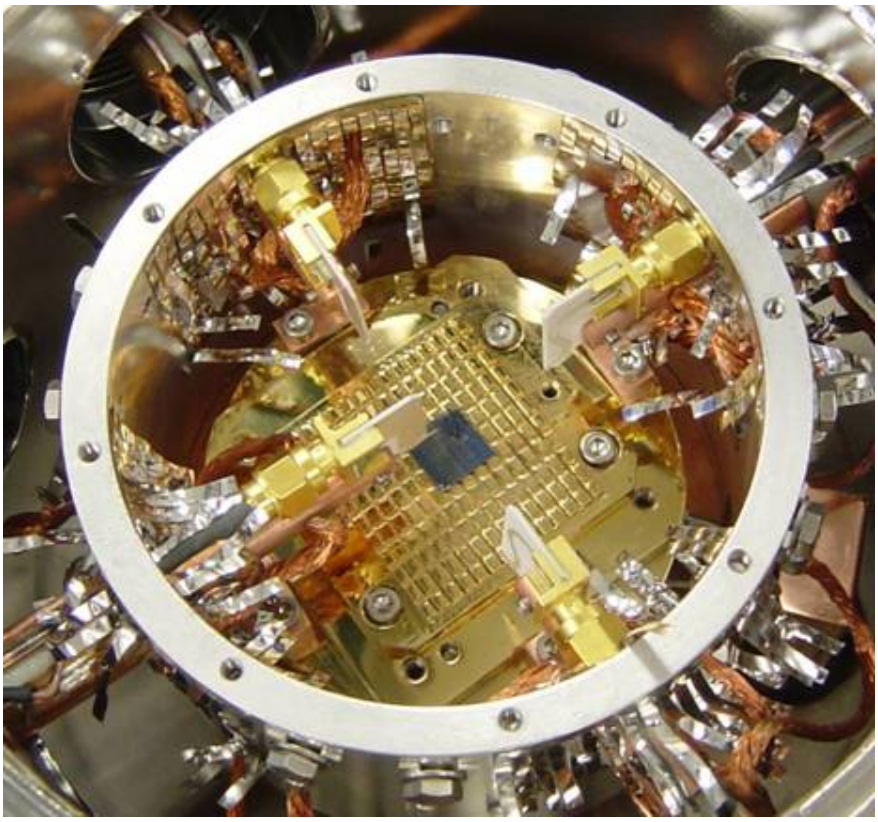

Figure 3.6. Probe station (Lakeshore Cryogenic) used to measure the nanoCell device. The probe station provides a high vacuum environment (~10^{-7} torr) to eliminate any free particles in the neighborhood of the sample.

The electrical measurement is performed by a HP 4145 semiconductor parameter analyzer remotely controlled by a computer. As shown in Figure 3.7, the applied voltage is swept in a staircase manner according to the input parameters: start voltage V_1, stop voltage V_2, voltage step ΔV, delay time Δt. The current is measured at the end of each voltage step.

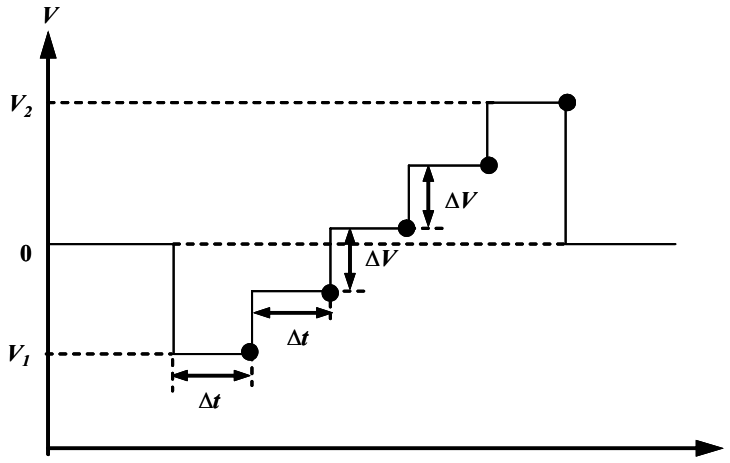

Figure 3.7. Applied voltage for the transient current-voltage measurements. A staircase voltage sweep starts at V_1, the first measurement takes place after a time delay Δt at constant voltage V_1. After the first measurement, the voltage is increased to $V_1+\Delta V$, and the measurement takes place after Δt, and this process continues until the last measurement is finished, then the applied voltage goes back to zero.

3.6 Electrical characteristics of nanoCells

Current voltage measurement is carried out on the simple structure with only two opposing electrodes, as shown in Figure 3.8. There are only OPE molecules self-assembled in the nanoCell.

Most of the devices tested exhibit NDR-like behavior, as shown in Figure 3.9, i.e., the current changes inversely according to applied voltage. Thus, NDR-like behavior has two conductive states at the same current. The current peak value and position, and even the number of peaks may vary for each device. In addition, the devices show similar current-voltage characteristics under both polarities of biased voltage, although the peak value and the position may not be exactly the same.

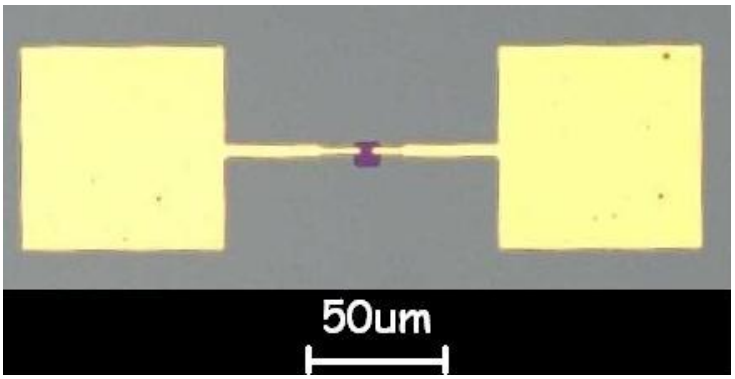

Figure 3.8. Two-electrode nanoCell that is measured. The large yellow squares are the contact for external field application; the purple square in the center is the discontinuous gold film.

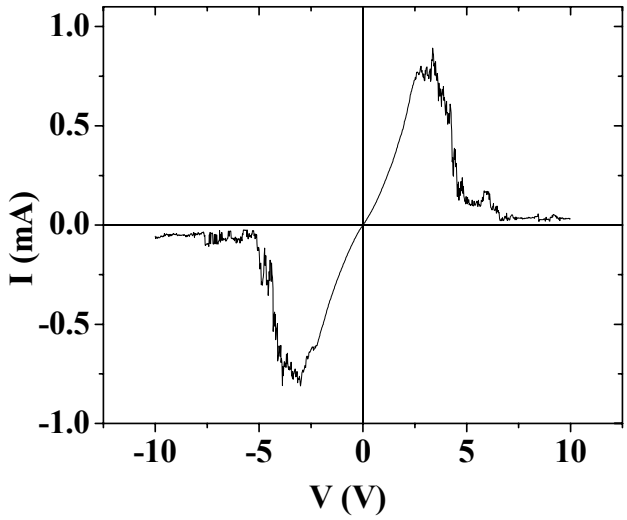

Figure 3.9. Typical NDR-like behavior shown in nanoCell device.

3.6.1 Transition states before NDR

Initially, no NDR behavior is found in the nanoCells, instead, transition states are found before NDR appeared. Based on the tested nanoCells, 50% of them exhibit initial transitional behavior as shown in Figure 3.10. During the first voltage sweeps from 0 V to 5 V, the nanoCell exhibits repeatable linear I-Vs (Figure 3.10a). When the voltage sweeps from 0 V to 10 V, the current drops sharply at a certain voltage V_{th1} = ~6.8 V (Figure 3.10b). When a voltage less than 6 volts is applied, the current is relatively low which is between 9 and 10 nA, as shown in Figure 3.10c. If the voltage is above 6 volts, the current increases about 3 orders of the magnitude, as shown in Figure 3.10c. Therefore voltage of 6 volts is defined as the threshold voltage, which is denoted as V_{th2}. Repeatable NDR-like characteristics appear in the subsequent voltage sweeps (Figure 3.10d). This sequence of events is referred as the first observed initial transitional behavior, which is composed of a high conductance ohmic behavior (Figure 3.10a), a breakdown behavior (Figure 3.10b) and a transitional behavior (Figure 3.10c).

The initial transition states of the other 50% of the nanoCells do not contain the high conductance ohmic behavior and the breakdown behavior. In stead, they contain only the transitional I-V. It is referred to as the second observed initial transitional behavior. For the last 10% of the nanoCells, the transitional I-V does not occur before NDR appears. It is referred to as the third observed initial transitional behavior.

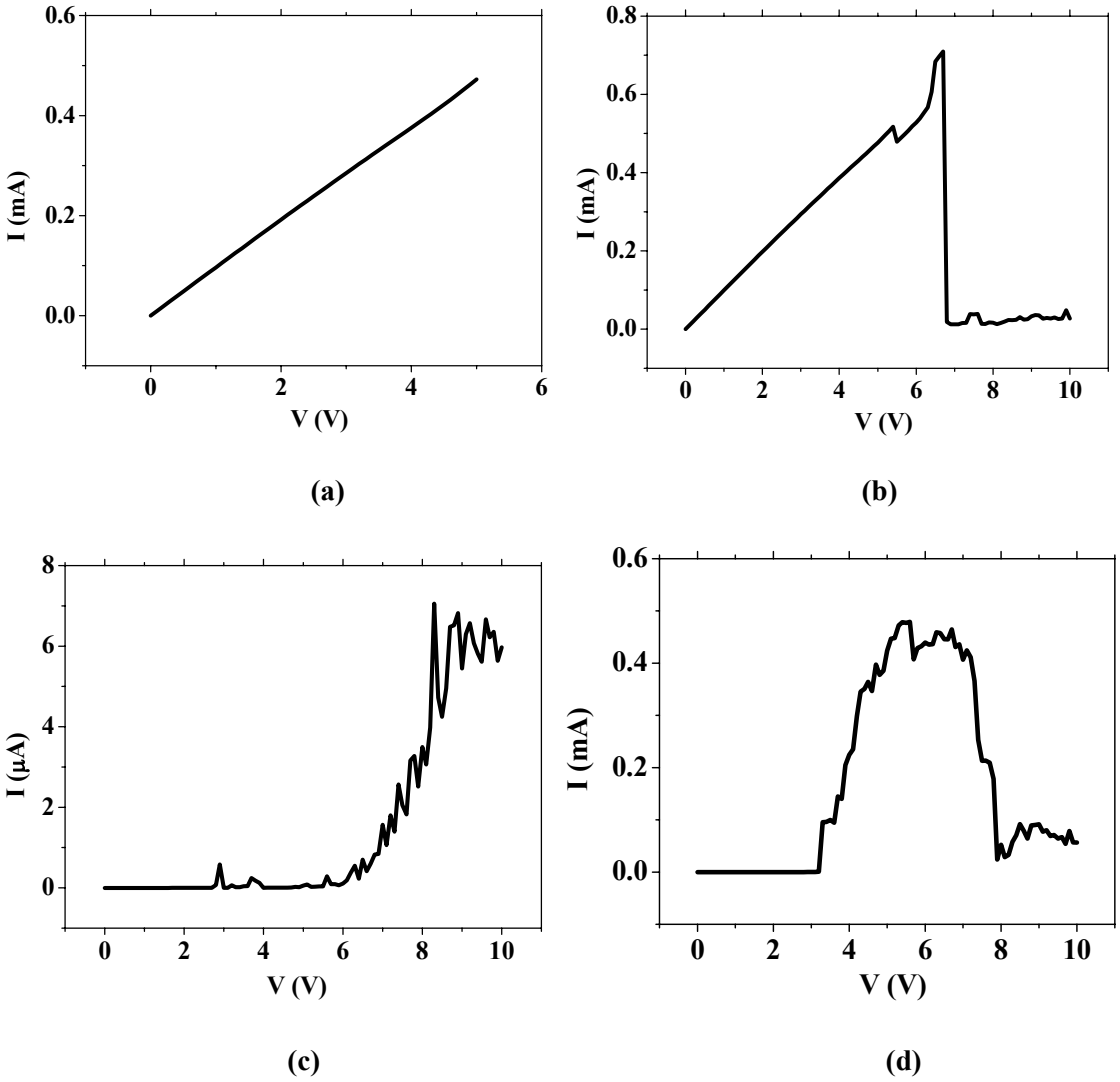

Figure 3.10. First observed current voltage transition behavior of a nanoCell device. (a) high conductance ohmic I-V s from 0 to 5V; (b) breakdown once the bias voltage exceeds ~6.8V; (c) transitional I-V, low current increases sharply at about 6V; (d) NDR-like behavior [65].

An interesting feature of all these three transitional behaviors is that it is not reversible, i.e., the nanoCell cannot be switched back to the original state by the application of a biased voltage. For instance, for the first observed one, once the NDR

appears, the ultra-high conductance ohmic behavior can not be observed. In addition, on unbiased nanoCell devices, negative voltage sweeps also induce similar sequences of I-Vs and finally reach the NDR-like behavior. However, on biased nanoCells, after the NDR has appeared in the forward biased range, it also shows up in the negative biased range without the initial and transitional sequence of I-Vs, and vice-versa.

3.6.2 Effect of electrode geometry on nanoCell IV

Further investigation has been conducted in the transitional state and it has been found that there is a relationship between the shape of the I-V curves and the shape of the electrode geometry. Two types of electrode geometries were fabricated on a nanoCell device, which are acute electrodes (Figure 3.11a) and obtuse electrodes (Figure 3.11b).

(a) **(b)**

Figure 3.11. Schematic drawing of electrodes. (a) Acute electrodes; (b) obtuse electrodes.

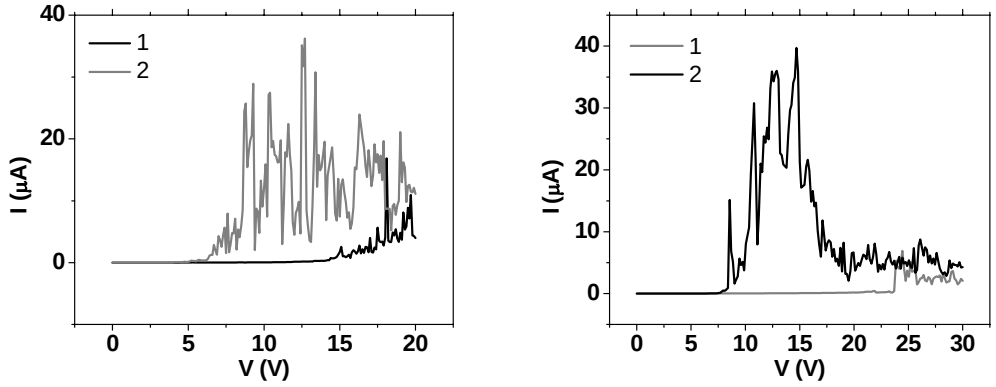

(a) **(b)**

Figure 3.12. Current voltage characteristics of a nanoCell with different electrode geometries. (a) I-V for nanoCell with acute electrodes; (b) I-V for nanoCell with obtuse electrodes. The numbers in the legend represent the sequence of the measurements.

As shown in Figure 3.12, before NDR appears, the nanoCells with acute electrodes experience a smoother transitional state than the ones with obtuse electrodes. This phenomenon might be explained by the crowded current at the tips in the acute electrodes. For the acute electrodes, the conductance paths of electrons are more focused than for the obtuse electrodes.

3.6.3 Memory phenomenon in nanoCells

Memory is another phenomenon that has been observed in a nanoCell. Based on the forward biased I-V characteristics which indicate NDR characteristics, as shown in Figure 3.10d, the operating voltage range of the nanoCell can be obviously divided into two regions separated by a threshold voltage V_T When the applied voltage is confined below V_T , the I-V curve is relatively smooth and follows a predictable track. When

voltage goes beyond V_T, the I-V curve becomes less predictable and includes one or several negative resistance regions. The interesting feature of nanoCell is that the conductance of the first region can be changed by applying a voltage beyond the second region.

As shown in Figure 3.13, if a voltage sweep with stop value higher than V_T is applied (curve 1 in Figure 3.13a), the next voltage sweep with stop value lower than V_T yields a low conductance of around $5.5 \times 10^{-8}\ \Omega^{-1}$ (curve 1 in Figure 3.13b). This low conductance can be switched to high conductance by applying another voltage sweep with stop value higher than V_T (curve 2 in Figure 3.13a). The resulting conductance is around $1.7 \times 10^{-5}\ \Omega^{-1}$ (curve 2 in Figure 3.13b). Thus, the process of applying a voltage that is higher than V_T is "write", while the process of applying a voltage that is lower than V_T is "read". If we assign the high conducive state as "1" or "on" and low as "0" or "off", the nanoCell can be switched between "1" and "0" by applying the writing process.

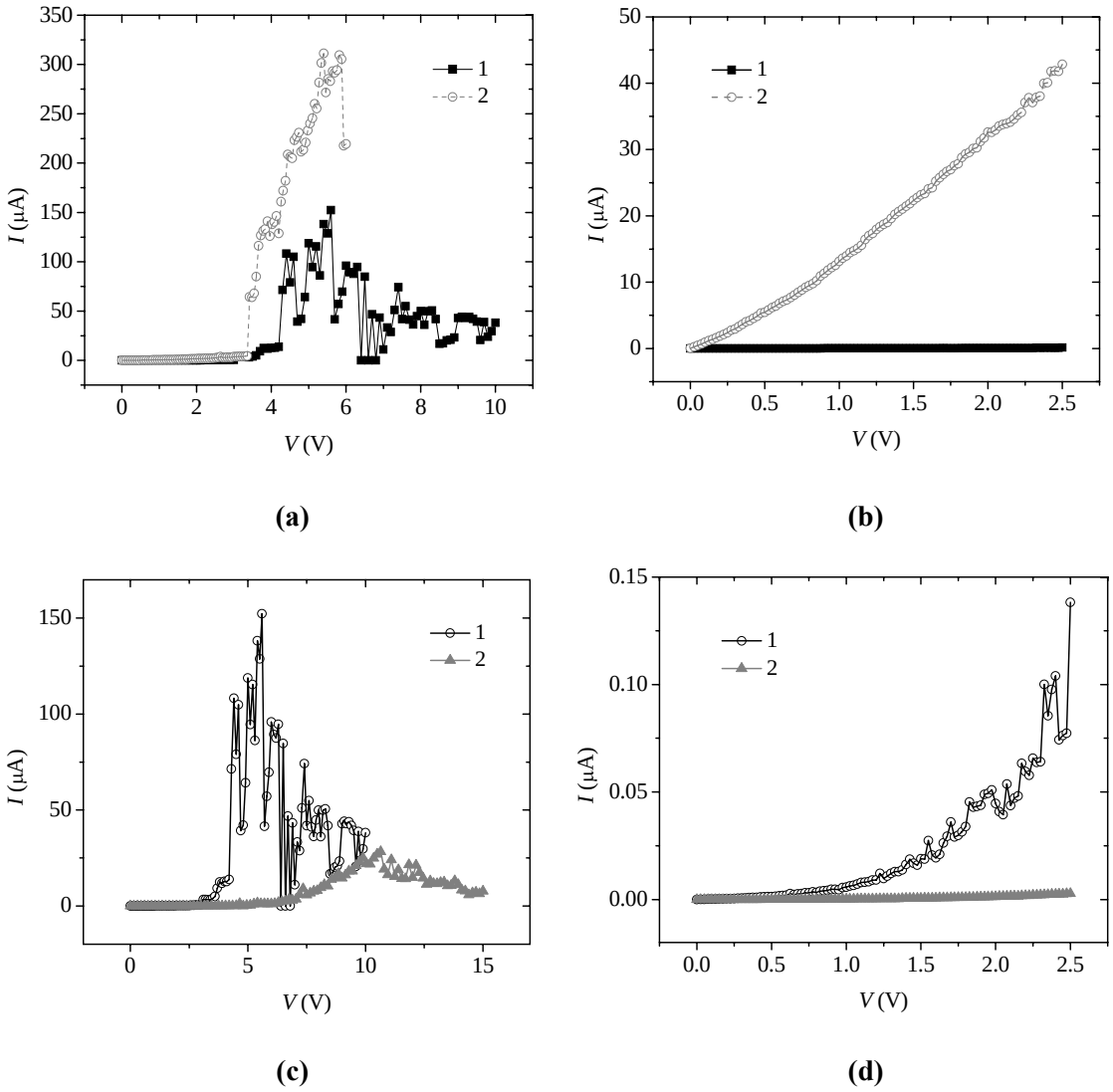

Figure 3.13. Repeatable memory effect in a nanoCell with V_T = 3 V. (a) Writing process in which the final currents are 38 μA and 219 μA for curve 1 and 2, respectively; (b) reading process in which the conductance are 5.5×10^{-8} Ω^{-1} and 1.7×10^{-5} Ω^{-1} for curve 1 and 2, respectively; (c) writing process in which the final currents are 38 μA and 8 μA for curve 1 and 2, respectively; (d) reading process in which the conductance are 5.5×10^{-8} Ω^{-1} and 1.0×10^{-9} Ω^{-1} for curve 1 and 2, respectively.

It is necessary to notice that the assignment of "1" and "0" to difference conductive state is arbitrary since the conductance of the read I-V is dependent on the

final current value of the writing process. For example, the conductances curve 1 and 2 in Figure 3.13d are both low if we compare them to curve 1 in Figure 3.13b. However, it is obvious that they are different since their corresponding conductance are 5.5×10^{-8} Ω^{-1} and 1.0×10^{-9} Ω^{-1} for curve 1 and 2, respectively. Certainly, in order to insure a high on-off ratio, these conductive states will not be used to differentiate "1" and "0".

Both conductive states are repeatable, i.e., any subsequent read voltage sweep generates similar I-V curve as in the previous one. Besides, switching between the two conductive states is repeatable, i.e., any induced conductive state can be switched to the other one by applying a write voltage. In addition, as shown in Figure 3.14, the read voltage is reversible, i.e., the I-V characteristics generated from reverse read voltage sweep also follows the same pattern.

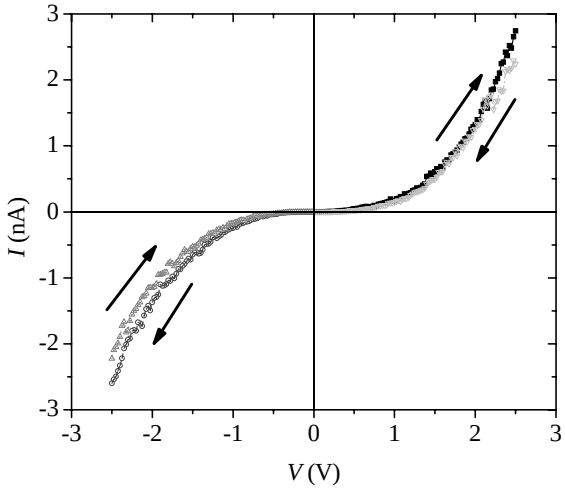

Figure 3.14. Read conductance in forward and reverse biases. The arrows indicate the direction of applied voltage.

Switching could also be carried out by applying a voltage pulse. Similarly, reading can be done by a constant voltage. For example, for the nanoCell that already shown a "0" state, if a voltage pulse of 6 V for 0.05 second, a higher current will be resulted at a read voltage of 2 V (Figure 3.15).

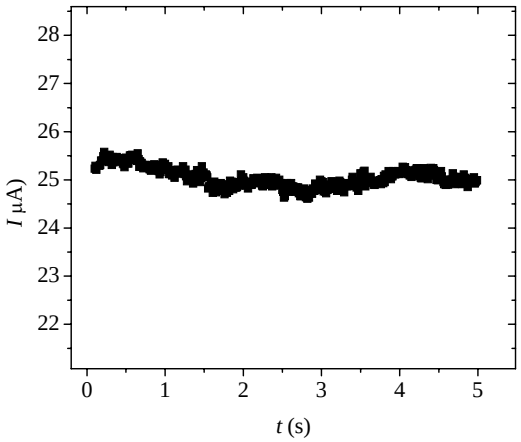

Figure 3.15. A read current at 2 V vs. time after a write voltage of 6 V for 0.05 second.

3.6.4 Influence of molecules on electrical behavior

One interesting experiment is to prepare and test four different ensembles (Figure 3.16) by depositing different combinations of molecule **1** and **2.** The first ensemble has only the discontinuous gold film; the second one has molecule **1** self-assembled on the gold islands of the discontinuous gold film; the third ensemble has molecule **2** self-assembled on the silicon oxide of the substrate; the fourth one has **1** and **2** self-assembled on the gold islands and SiO_2, respectively. It is expected that the first and the third ensemble should have extremely low conductance, since alkane and vacuum are both good insulators; the fourth ensemble should have a conductance somewhat in

between. However, the four ensembles showed similar I-V characteristics with peak current values in the same order of magnitude. Thus we reach the conclusion that the above observed behavior is due to the electron migration through discontinuous gold film.

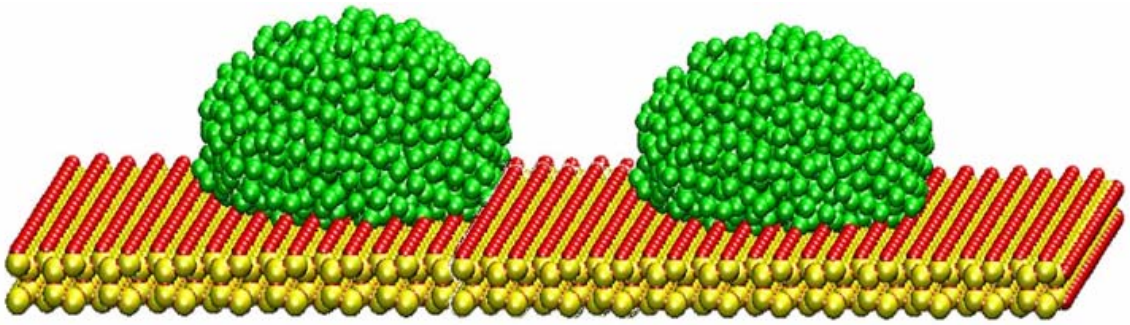

(a)

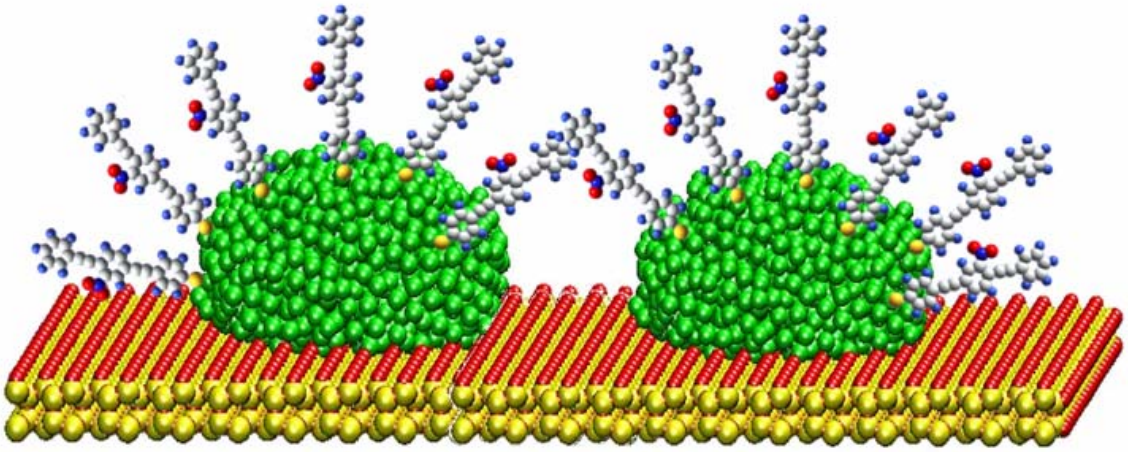

(b)

Figure 3.16. Schematic drawings of four ensembles of the nanoCells. (a) Only the discontinuous gold film on SiO_2; (b) molecule 1 deposited on the discontinuous gold film islands; (c) molecule 2 deposited on the silicon oxide surface; (d) molecules 1 and 2 deposited on gold and SiO_2, respectively.

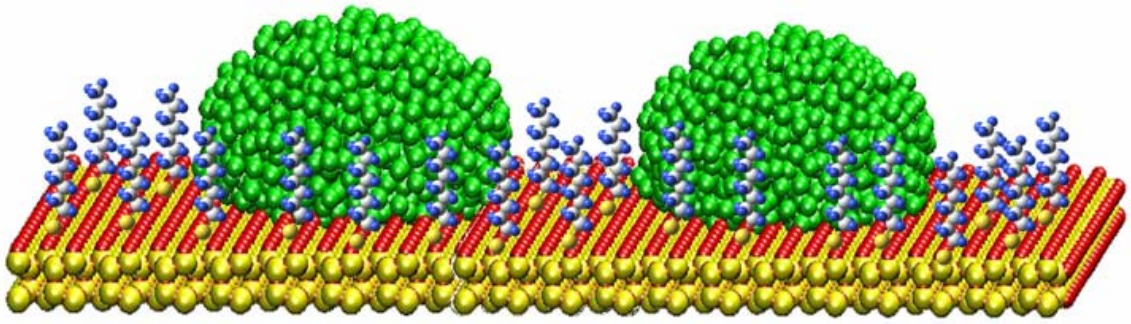

(c)

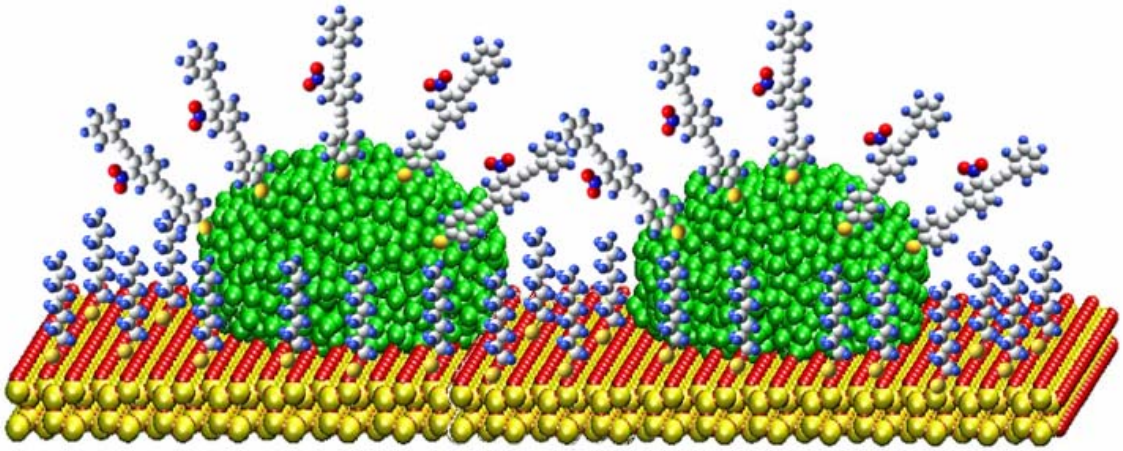

(d)

Figure 3.16 (Continued)

In order to further investigate the influence of molecules on the nanoCells electrical behavior, one of the chips with nanoCells featuring NDR, is cut into two pieces. Molecule OPE is deposited on one half of the chip and alkane molecule on the other half of the chip. The nanoCells with OPE molecule (Figure 3.16b) exhibit similar switching characteristics like the nanoCells with only the discontinuous gold film

(Figure 3a), including a similar threshold voltage and NDR peak value. This further demonstrates that only the formed gold filaments are responsible for the NDR behavior or at least that the contribution of the OPE to the electron conductance is negligible compared to the contribution of the filaments. The nanoCells with alkane molecule (Figure 3.16c) self-assembled on SiO_2, show increases in threshold voltage V_{th2} (~10 V higher). This means that the insulating alkane molecule creates a higher barrier for the electron transfer through gold islands. After reaching V_{th2}, the barrier is overcomed and we obtain a NDR characteristic similar to those found without any molecule or with only OPE. We carry out deposition of alkane on the chips already containing molecule OPE (Figure 3.16d). This fourth ensemble (Figure 3d) exhibits similar behavior like the third ensemble (Figure 3.16c), which is consistent with our previous conclusion that the I-Vs of the nanoCell with and without OPE are very similar.

To further investigate the influence of OPE, we deposit OPE on a chip where no current is found. After deposition, there is still no current. This, again, proves that the OPE have no significant influence on the I-Vs of the nanoCells.

3.7 Programming of nanoCell

The nature of randomness on addressing molecules inside the nanoCell makes this device dependent on computer programming.

In a multi-leads nanoCell, each pair of the leads shows similar switching and memory phenomenon as in the two-lead nanoCell. Once a conductive state has been written to one of the lead pairs, the conductance of the same nanoCell between the other pairs changes accordingly. During the measurement, only the two leads of interests are

connected to the semiconductor parameter analyzer, while others are dangling. Take the nanoCell shown in Figure 3.17 as an example. When the conductive state between K-E is set to “1”, the conductive states between other pairs of leads are summarized in Figure 3.18.

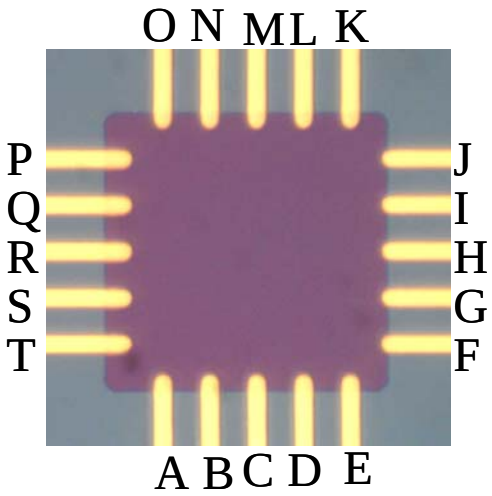

Figure 3.17. Multiple leads nanoCell with alphabetic notation on each leads.

Three kinds of conductive states exhibit on this nanoCell. The “1” and “0” correspond to the high and low conductance, respectively. These are expected to be observed. However, there is a third state with high conductance and Ohmic behavior which is similar to the initial transitional behavior in the two-leads nanoCell. In the programming of nanoCell, this kind of conductance can be ignored. However, it provides interesting information for our discussion in the next Chapter.

S\D	A	B	C	D	E	F	G	H	I	J	K	L	M	N	O	P	Q	R	S	T
A	X	1	1	1	1	0	0	0	0	0	1	1	1	1	1	1	1	1	1	1
B	1	X	1	1	1	0	0	0	0	0	1	1	1	1	1	1	1	1	1	1
C	1	1	X	1	1	0	0	0	0	0	1	1	1	1	1	1	1	1	1	1
D	1	1	1	X	1	0	0	0	0	0	1	1	1	1	1	1	1	1	1	1
E	1	1	1	1	X	0	0	0	0	0	1	1	1	1	1	1	1	1	1	1
F	0	0	0	0	0	X	0	0	0	0	0	0	0	0	0	0	0	0	0	0
G	0	0	0	0	0	0	X	0	0	0	0	0	0	0	0	0	0	0	0	0
H	0	0	0	0	0	0	0	X	0	0	0	0	0	0	0	0	0	0	0	0
I	0	0	0	0	0	0	0	0	X	0	0	0	0	0	0	0	0	0	0	0
J	0	0	0	0	0	0	0	0	0	X	0	0	0	0	0	0	0	0	0	0
K	1	1	1	1	1	0	0	0	0	0	X	a	0	0	0	0	0	0	0	0
L	1	1	1	1	1	0	0	0	0	0	0	X	a	0	0	0	0	0	0	0
M	1	1	1	1	1	0	0	0	0	0	0	0	X	a	1	1	1	1	1	1
N	1	1	1	1	1	0	0	0	0	0	0	0	0	X	a	0	0	0	0	0
O	0	0	0	0	0	0	0	0	0	0	0	0	0	0	X	0	0	0	0	0
P	1	1	1	1	1	0	0	0	0	0	0	0	0	0	0	X	a	0	0	0
Q	1	1	1	1	1	0	0	0	0	0	0	0	0	0	0	0	X	a	0	0
R	0	0	0	0	0	0	0	0	0	0	0	0	0	0	0	0	0	X	a	a
S	0	0	0	0	0	0	0	0	0	0	0	0	0	0	0	0	0	0	X	0
T	1	1	1	1	1	0	0	0	0	0	0	0	0	0	0	0	0	0	0	X

Figure 3.18. Truth table of a nanoCell as K-E is set to “1”. The truth value in any entry is measured between the drain-terminal (D) and the source-terminal (S) when a voltage sweep is applied to the drain.

The programming of nanoCell can be carried out using a multiple probe testing board and computer controlled oscilloscope. The fundamental idea is to first to collect all the switching information between each leads. For example, the switching information between KE when KE is “1” has been obtained. The switching information between KE when KE is “0” also needs to be obtained. Similarly, the information between AB, CD, JO, and etc. needs to be obtained. Once a data-base of switching information is formed, computer calculates the specific pair of leads that a voltage pulse can write into to perform desired function.

CHAPTER IV

ELECTRICAL CONDUCTANCE OF DISCONTINUOUS METALLIC FILM

In this section, first the theoretical models proposed by several researchers to explain the electrical conductance through discontinuous metallic films are outlined. Then the electrical conductance is investigated both experimentally and theoretically in two categories: below the threshold voltage and beyond the threshold voltage.

4.1 Theoretical models in discontinuous metallic film

Since nanoCell with only discontinuous gold film have large current (> 1 μA) and exhibit memory and switching phenomena, the understanding of the electrical conductance of discontinuous metallic film becomes critical for the analysis of programmable molecular array. It will not only benefit the research work in discontinuous-metal-film-based nanoCell, but also provide in-depth knowledge of electron transport through any two-dimensional molecular array. Since the molecules that will be used in the programmable molecular array are semiconducting, ultimately the programmable molecular array can be viewed as a two-dimensional array of electron transport junctions, as the discontinuous metallic film does.

As early as 1960's, electrical conductance through discontinuous thin metal films has been studied by a number of researchers. Non-Ohmic behavior of the electrical conductance have been observed in several types of discontinuous metal film.[66-69]

Neugebauer et al. proposed that when island sizes and separations between them are both small, activated tunneling of electrons is the dominant mechanism of electron transfer.[70] The barrier to tunneling is the energy difference between a Fermi-level of a particle and the lower edge of the conduction band of the substrate. Hill et al. developed a two-island model to account for the transport.[71,72] According to Hill, the current density in a discontinuous metallic film is

$$J(V,T) = \frac{4\pi me}{h^3 B^2} \frac{\pi BkT}{\sin(\pi BkT)} \exp\left(- A\bar{\phi}^{1/2} - \frac{\delta E}{kT} \right) \frac{eV}{kT} \tag{4.1}$$

where $A = 4\pi(2m)^{1/2} \Delta s / h$, $B = A / 2\bar{\phi}^{1/2}$, m is the mass of an electron (9.1095×10^{-31} kg), $-e$ is the electron charge, k is Boltzmann's constant, h is Planck's constant, T is the absolute temperature, $\bar{\phi}$ is the mean potential barrier height, Δs is the effective barrier width, V is the voltage applied between islands and δE is the activation energy. The activation energy is the work required in transporting an electron from one of the islands against the Coulomb force between the emitted electron and the charged island. At low electric field, it is expressed as[71]

$$\delta E = \delta E_0 \equiv \frac{e^2}{\varepsilon} \left(\frac{1}{r} - \frac{1}{2r + d} \right) \tag{4.2}$$

where ε is the dielectric constant of the medium, r is the radius of an island, and d is the gap distance. Hill proposed that when the electric field is strong enough, the Coulomb potential rises to a maximum, so does the activation energy. Thus a non-Ohmic conductance arises.[71,72]

However, Uozumi et al. argued that the non-Ohmic conductance arises from non-Ohmicity of the tunneling current at high electric field, and the expression for the current density is[73]

$$J(V,T) = \frac{4\pi me}{h^3 B^2}\exp\left(-A\phi^{-1/2}\right)\frac{\pi BkT}{\sin(\pi BkT)} \times\left\{\exp(B\delta E_0)\sinh\left(\frac{eV}{kT}-\frac{1}{2}BeV\right)-\sinh\left(\frac{eV}{kT}+\frac{1}{2}BeV\right) + \exp\left(-\frac{\delta E_0}{kT}\right)\left[1+\exp(B\delta E_0)\right]\sinh\left(\frac{1}{2}BeV\right)\right\} \times\left[\cosh\left(\frac{\delta E_0}{kT}\right)-\cosh\left(\frac{eV}{kT}\right)\right]^{-1} \quad (4.3)$$

They also found that the non-Ohmicity occurs when the electric field between two metal island exceed the critical field E_c, which is defined as [73]

$$E_c = kT/ed \quad (4.4)$$

Uozumi et al. extended the two-island model to one-dimensional series-connected-islands with identical sizes but different gap lengths.[74] Their computational result showed that the voltage between two islands can be about a hundred times higher than the average voltage calculated from the one between the two electrodes and that the logarithm of the conductance depends almost linearly on the square root of the voltage between the two electrodes above the threshold voltage.[74] Their experimental results further confirmed their suggestion.[75]

A tremendous breakthrough was accomplished by Shin et al., who proposed a ring-shaped model to account for the transport properties.[76,77] In this model, the ring-

shaped array of small islands is located between the two electrodes (Figure 4.1). Thus unlike the one-dimensional arrays proposed by others,[71-75,78-81] there are two branches of paths for electron transfer. Electrons may get trapped in one of the island.[82] Thus multiple Coulomb blockade gaps may appear in current-voltage characteristics[76] as current peaks followed by NDR behavior. This is the distinct features of this modal in contrast to the linear 1D array. In addition, trapped electrons block the electrical conduction through the array, so no current flows. Using Monte Carlo simulation, Shin et al. were able to calculate the current for constant voltage between the two electrodes.

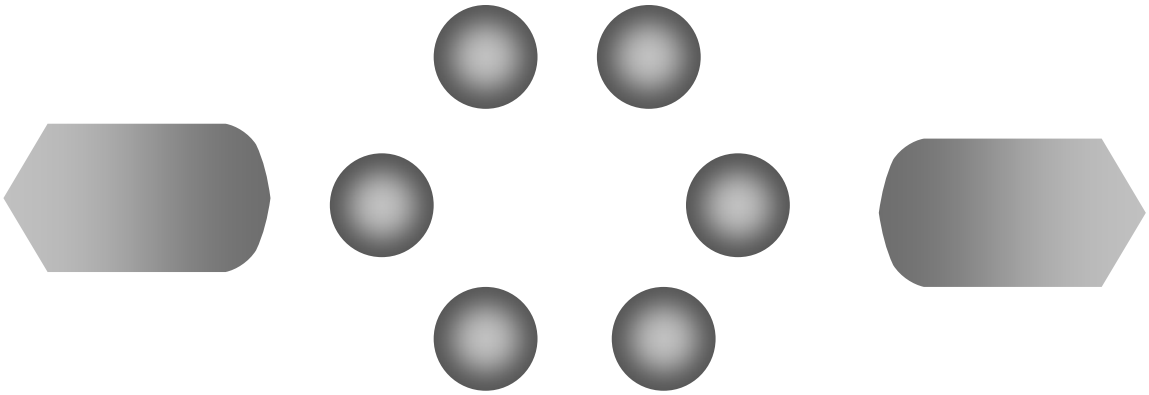

Figure 4.1. The ring-shaped model proposed by Shin et al.[76,77] The six islands are located between the two electrodes.

Interestingly, NDR and memory phenomena has been observed and reported in thin insulating films made of SiO[83] and in organic light emitting diodes[84-95]. Tang et al.

found that for those devices, nano-sized metallic islands exist inside the insulating film. Thus, they explained the NDR and memory phenomena based on the ring-shaped model of four islands.[96] The state that the trapped electrons block the conductance path is the "off" state; otherwise it is "high". The thermal fluctuations results in the transition between "on" and "off", thus the NDR appears.[96] When the temperature increases, the current peak broadens. In addition, The memory effect is due to the "charging" and "discharging" of the electrons in the system.[96]

4.2 Electron transport through discontinuous metallic film below activation energy

As it is mentioned in the last Chapter, the current voltage characteristics of nanoCell can be divided into two regions: below V_T , the current increase with increasing voltage and the I-V curve follows a predicted behavior; beyond V_T , the I-V curve changes violently and include one or several local current maximum.

When the applied voltage is below $\boldsymbol{V_T}$, the I-V characteristic is relatively smooth for both low conductance and high conductance. In order to find out the electron conduction mechanism, we performed a temperature variant current-voltage measurement on the nanoCell sample that carries room temperature I-V curves shown in Figure 4.2. There are no molecules deposited on the discontinuous film. Thus the gaps between the gold islands are considered as vacuum.

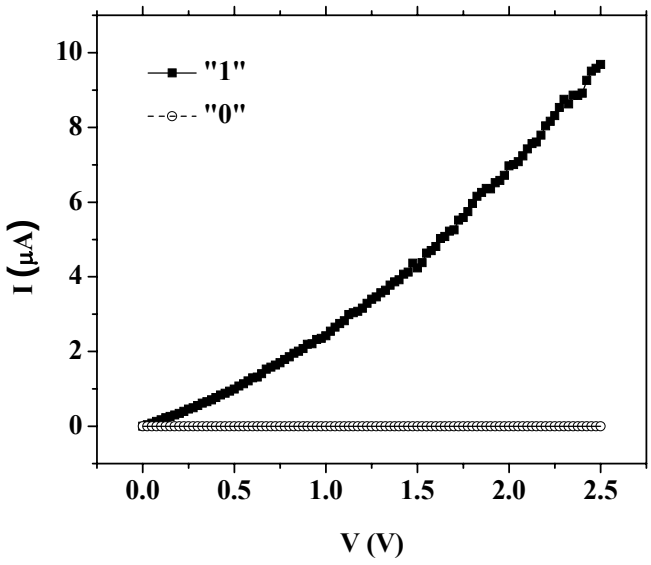

Figure 4.2. Room temperature I-V curves of the sample whose field dependences of conductance are shown in Figure 4.3 and Figure 4.4.

Interestingly, although discontinuous gold film is a two-dimensional array of junctions, the electrical characteristics resembles the one that predicted by Uozumi et al. Figure 4.3 shows the electric field dependence of the high conductance G of a discontinuous gold film at various temperatures. The electric field is calculated directly from applied voltage by dividing 2×10^{-4} cm which is the distance between the two electrodes for this particular sample. The interesting feature of these curves is a remarkable ohmic conductance can be observed beyond 220 K at low electric fields, i.e., around 20 $(V/cm)^{-1/2}$. Thus the critical applied field strength from 220 K to room temperature is 400 V/cm. A second interesting point is for all temperatures, there is another critical applied field above which the logarithm of the conductance ***G*** depends almost linearly on the electric field in a form of

$$\log G = N \cdot E^{1/2} + C \tag{4.5}$$

where ***N*** is the slope and ***C*** is the interception.

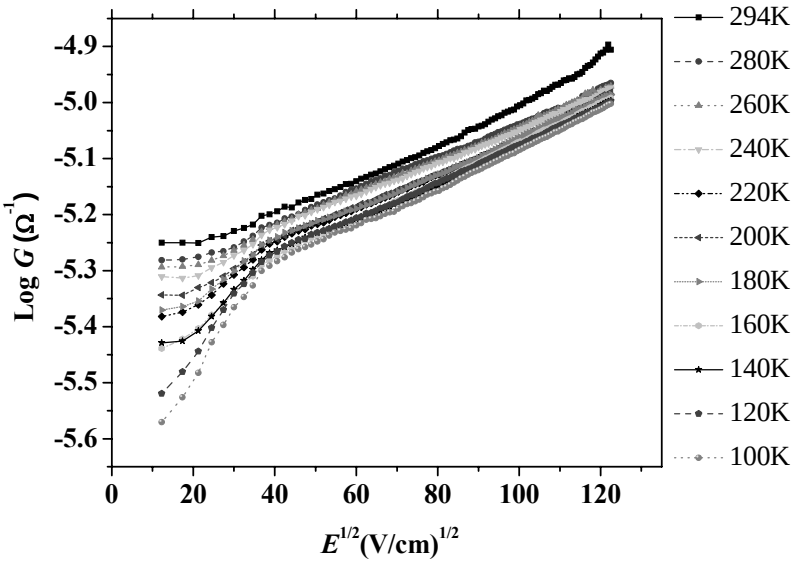

Figure 4.3. Electrical field dependence of the high conductance of a discontinuous film.

In contrast, the electric field dependence of the low conductance G at various temperatures is shown in Figure 4.4. Since the current is close to zero, the measurement will inevitable generate some artifact current value that is lower than zero. It should be noted that although the current is extremely small, there is a slightly larger variation of the current in low field. Since the largest variation happens in 260 K and 220 K, so it seems that this variation does not depend on temperature.

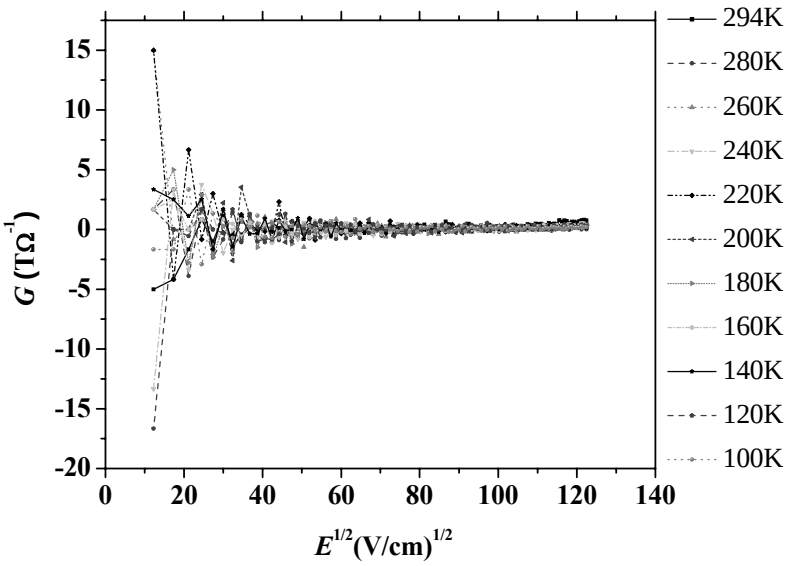

Figure 4.4. Electrical field dependence of the low conductance of a discontinuous film.

From scanning electron micrograph image of discontinuous gold film shown in Figure 3.4c, approximately the mean value of gap length is $d = 5$ nm, the mean radius of gold island length is $r = 25$ nm. Since the distance between the two electrodes is $l = 2$ μm, there are

$$n = \frac{l}{d+m} = \frac{2um}{5nm + 50nm} = 36 \tag{4.6}$$

gaps between two electrodes. The field enhancement factor α is

$$\alpha = \frac{l}{n \cdot d} = \frac{2um}{36 \cdot 5nm} = 11 \tag{4.7}$$

Thus according to equation (4.4), the critical voltage between two gold islands V is

$$V = \alpha \cdot E_c \cdot d = 11 \times 1600 \cdot V/cm \times 5nm = 0.008V \tag{4.8}$$

It is theoretically predicted that non-ohmic conductance should appear when the applied voltage between two islands exceeds kT/e, where $\boldsymbol{k}$ is the Boltzmann's constant 8.617×10^{-5} eV/K, T is the temperature and $\boldsymbol{e}$ is electron charge. So in 298K the critical voltage is 0.026V, which is in the same order of magnitude as calculated by our experiment, i.e., 0.008V.

The disagreement rises from the errors in the estimation of islands sizes and gap length. Also the theoretical model is based on a 1-D array with only one conductance path, however for the actually sample with thousands of gold islands, multiple conductance paths exist and they will inevitably complicate the situation.

It has been shown theoretically that in a discontinuous gold film, electrons flow from one of the electrodes to the other preferably via the most conductive paths.

4.3 NDR region beyond threshold voltage

While several mechanisms have been proposed to explain the NDR behavior, modern molecular simulation technique enables us to visualize the atomic movement in an electrical field. Molecular dynamic simulations have been performed on a 1D nanowire with hundreds of gold atoms. The simulation starts from an ideal state where all the atoms are closely packed and the whole nanowire is in a regular shape (Figure 4.5a). Since this shape has relatively high conductance, we could say the peak current is associated with it. When an electric field is acting upon the nanowire, the local temperature of the nanowire increases, the atoms begin to vibrate violently, yielding the irregular shape shown in Figure 4.5b, which also accounts for the decreasing current. The atoms continue to vibrate, and the shape of the nanowire is constantly changing,

which results in the rising and falling of the current. At some point the atoms vibrate so violently that the nanowire breaks, yielding nano-clusters, then current rapidly drops to zero (Figure 4.5c). After the nanowire breaks, the local temperature decreases. Then under the high voltage electron migration induced the moving of the gold atoms, thus bridging the nanoclusters (Figure 4.5c). Hence the current increases again. This could also explain the rising of the current when the biased voltage is between V_T and V_{max}.

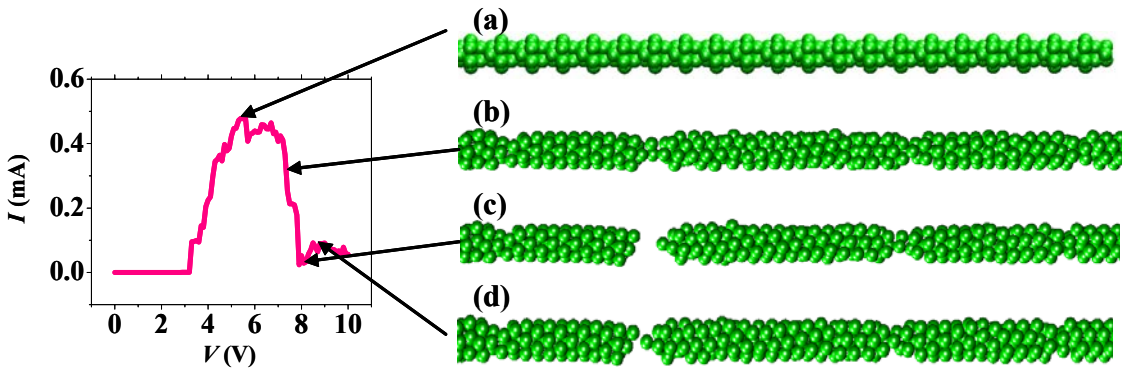

Figure 4.5. Comparison of molecular simulation results and experimentally obtained I-V.

Thus, by the assistance of molecular dynamic simulation, the I-V characteristic beyond V_T can be explained and is mainly due to the combination effect of thermal motion and electro migration.

4.4 Effect of the gate

According to Tang's explanation of memory effect, that the memory effect is due to the to the "charging" and "discharging" of the electrons in the system. Then any electron movement would affect the conductance of the system. However, we find that

it is only the case for larger voltage. An experiment is performed that a discontinuous gold film has four electrodes on the periphery (Figure 4.6).

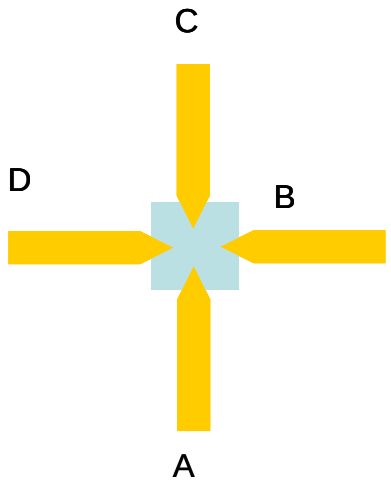

Figure 4.6. A piece of discontinuous gold film with four gold electrodes on the periphery.

As shown in Figure 4.7, if AC is originally set to low conductance state, and a subsequent read voltage sweep is applied to AB, then AC is still in low conductance state.

However, if a large voltage, a voltage beyond V_T is applied to AB, the conductive state between AC changes significantly. This phenomenon reaffirms the existence of a threshold voltage for the electron transport. Below the threshold voltage, the electrons are not activated and trapped in the vicinity of an island. However, if the electrons are activated and jump to other island, the conductance state change violently.

Although according to Uozumi, the activation energy is constant all over the discontinuous gold film. Thus the threshold voltage is about the same value.

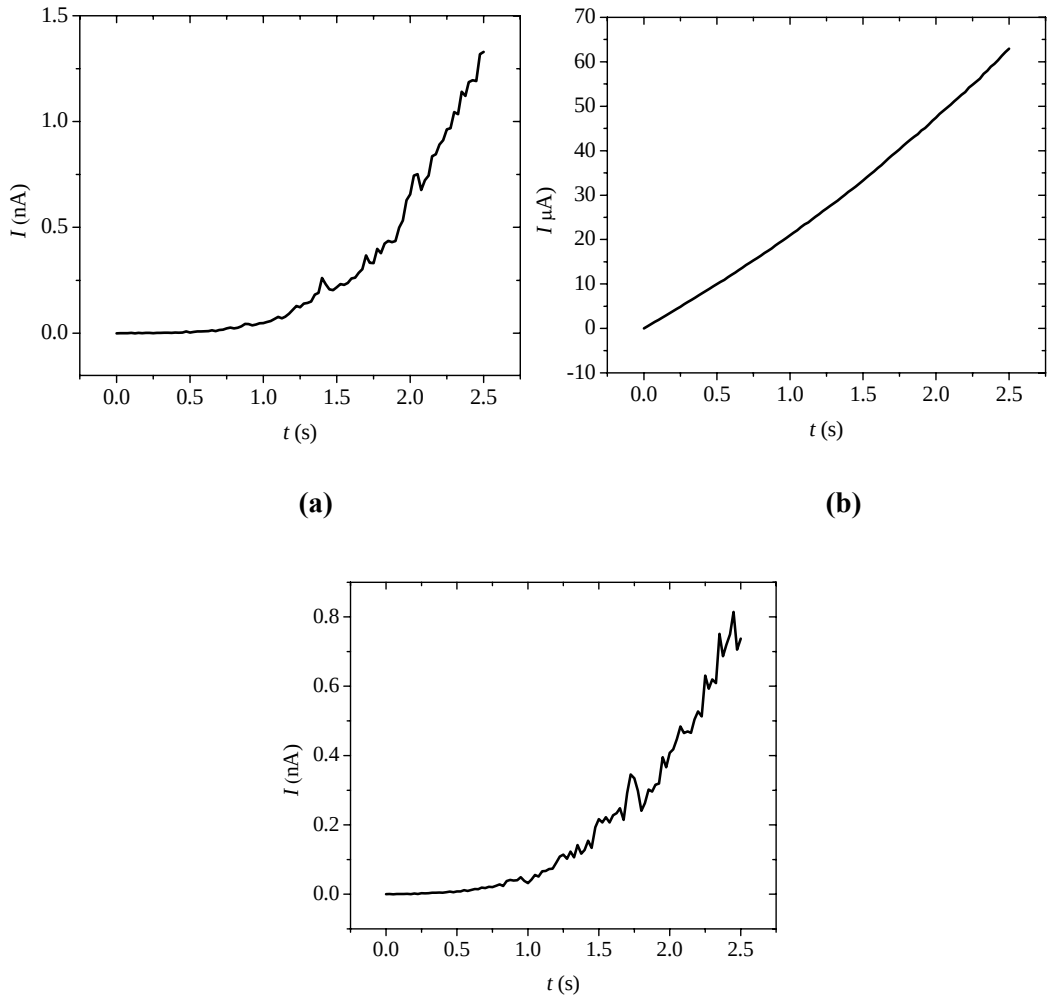

Figure 4.7. Effect of the gate on the electrical characteristics of the nanoCell. If AC is originally set to the low conductance state (a), and a subsequent read voltage sweep is applied to AB (b), then AC is still in low conductance state (c).

4.5 Effects of morphology of discontinuous gold film

The gold islands in the nanoCells are removed when a chip with discontinuous gold film is immersed in piranha solution (a mixture of H_2SO_4 and H_2O_2, in a ratio of 3:1) for 30 min. The temperature in this exothermic reaction rises to 130ºC. However, we find that only the gold filaments and clusters can be removed without significantly damaging the discontinuous Au film if the chip is immersed for a much shorter time. An experiment is carried out in which one chip with only the discontinuous gold film is immersed in piranha solution for 45 s. Thus, the gaps between the gold islands become wider after the piranha bath. On this chip, prior to the piranha bath treatment, some of the nanoCells have yielded NDR behavior. After the piranha bath, we find no NDR behavior in these nanoCells. Instead, the two types of observed behavior (first and second) are found again; therefore, the nanoCell can be reset to its original conduction state through the bathing process. Moreover, the nanoCell does not have memory of its previous behavior; in other words, a nanoCell, which initially exhibits the first observed behavior, may exhibit the second observed behavior after the piranha bathing, and vice versa (i.e., second behavior, piranha bath, and first behavior). Then, the same nanoCell chip is immersed in piranha for another 2 min and then 90% of the nanoCells do not show any current in excess of the noise (~0.1 pA) even when they are biased up to 100 V and observations under an optical microscope indicate that the discontinuous gold film (gold islands) is not removed.

CHAPTER V

STATIC AND TRANSIENT CURRENT VOLTAGE CHARACTERISTICS AT THE NANOSCALE

In this section, the standard transient response of conventional systems is first briefly reviewed. Then, the similarities and differences between the nano-sized systems and the conventional system are introduced. A situation is proposed in which the number of electrons may be in the order of magnitude as the number of nuclei. The effect of this situation is investigated based on the static current-voltage measurement of discontinuous gold film.

5.1 Standard transient response of conventional systems

For many physical systems or devices, there is a transient status between two stationary stages. The nature of the transient and stationary responses is determined by the individual characteristics of the system or device. What is most interesting is that most realistic systems have uniquely determined responses by the same equations, implying that both static and transient responses can be studied using similar techniques through several fields of science and engineering. In particular, systems with equivalent characteristics constitute the topic of several if not all of present engineering.

For example, the transient response for electrical and chemical systems shown in Figure 5.1 and Figure 5.2 are practically identical except that they correspond to very different time scales. Figure 5.1 shows an electrical circuit consisting of a resistor (***R***),

an inductor (***L***), and a capacitor (***C***) connected in series and with values of each component given by ***R*** = 10 Ω, ***L*** = 10 H, and ***C*** = 100 mF. At time ***t*** = 0, the voltage source v_s in the RLC switches on and applies a voltage of 1 V. The voltage across the capacitor *C* is [97]

$$v_c = e^{-\alpha \cdot t}\left[-\cos(\beta \cdot t) + K \sin(\beta \cdot t)\right] \tag{5.1}$$

where $\alpha = \frac{R}{2L}$, $\beta = \frac{\sqrt{4LC - (RC)^2}}{2LC}$ and $K = \frac{\alpha}{\beta}$.

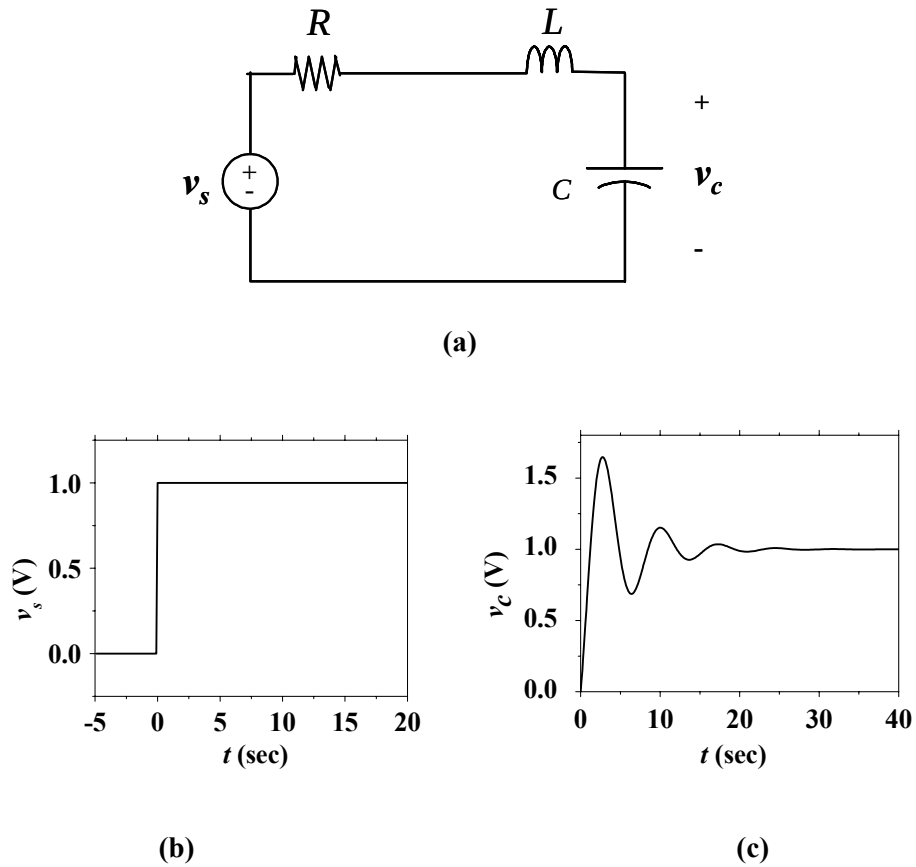

Figure 5.1. The transient response of a series RLC circuit. (a) Circuit layout; (b) step input; (c) transient response.

Figure 5.2 shows a chemical liquid storage system which exhibits an underdamped second-order flow-rate response. In this example, the liquid volume V = 100 m^3, liquid density ρ = 30 kg/m^3, original input and output mass flow rate $w_{ino} = w_{outo}$ = 50 kg/min, damping coefficient ζ = 0.2 and time constant $\tau = \frac{V \cdot \rho}{w_{ino}} = 1$ hour. At t=0, the input flow rate changes from 50 m^3/min to 70 m^3/min. The output flow rate after t=0 is

$$w_{out}(t) = w_{in0} + \left(w_{out}' - w_{out0}\right) \cdot \left\{1 - e^{-\zeta \cdot t/\tau}\left[\cos\left(\frac{\sqrt{1-\zeta^2}}{\tau}t\right) + \frac{\zeta}{\sqrt{1-\zeta^2}}\sin\left(\frac{\sqrt{1-\zeta^2}}{\tau}t\right)\right]\right\} \quad (5.2)$$

where w_{out}' is the output at steady state, which is 70 m^3/min in this case.

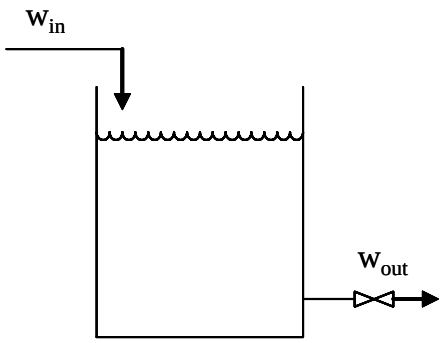

(a)

Figure 5.2. The transient response of a chemical liquid storage system with an underdamped second-order flow-rate response. (a) System configuration; (b) step input; (c) transient response.

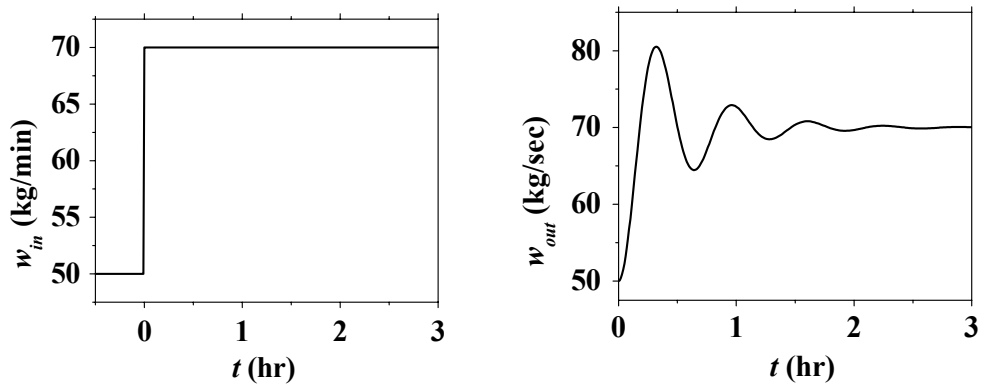

(b) **(c)**

Figure 5.2 (Continued)

For the electrical RLC circuit, the rising and falling of the voltage is determined by the movement and rearrangement of electrons in the RLC circuit, thus time scales associated are usually from fractions of seconds to fractions of nanoseconds; however, the chemical plant has a transient behavior depending on the movement and arrangement of big, macroscopic masses involving large portions of fluids and large mechanical systems with transient times from minutes to several hours.

This interesting analogy between chemical and electrical systems of totally different size, no matter human-fabricated or nature-made, has usually been taken for granted and we never ask the question why? Why this strong similarity between a macroscopic and microscopic system is not observed at the nanoscopic scale? The answer is based on the atomistic nature of the system. At microscopic level we can observe the robustness of the nuclei compared to the fluid, the electrons. For instance, a

typical current of 10^{-4}A in an n-channel silicon based Metal Oxide Semiconductor Field Effect Transistor (MOSFET) with channel length L = 1 μm, width W = 10 μm and depth d = 100 nm, represents a total of 6.25×10^{5} electrons flow through the channel in one nanosecond, which is the typical frequency (~GHz) of today's microelectronic device. We know the density of silicon is 5×10^{22} atoms per cm^{3}.[5] Thus in such a volume holding the little transistor, one single electron causes a small perturbation to an average of 10^{5} atoms. As a result, the nuclei in a crystal are not strongly affected by the dynamics of the electrons. Chemically speaking, when the nuclei are kept together by equally strong chemical bonds in the three dimensions, the strong dependence of transient and stationary responses is valid. This also gives rise to specific and sharply defined transient and stationary responses. A similar situation takes place at macroscopic level, for instance, in the chemical plant where the fluid is not a small perturbation to the materials forming the plant. Since the weight of the fluids in chemical plant is in the same order of magnitude as the materials making the plant, the nature of the flows may cause much more fluctuations in plants than electronics, which also explains why chemical plants require much more maintenance than the transistors in integrated circuits.

As the electronic device scales down dimensions whereby the number of electrons and the number of atoms becomes comparable, then a similar problem encountered in a chemical plant also is faced by the electrical circuits. The plant components should be robust enough to hold the fluids; however, in microelectronics,

the materials under process are not the electrons but information encoded on their flow. In electronics, the amount of information that can be processed per unit of matter has grown exponentially; however, in classical engineering, the amount of material that can be processed by a unit of plant material has undergone only a linear growth and it is practically constant with time. Thus the exponential growth of the former is going to strongly affect the electronic devices at nano-dimensions if we want to continue with such an exponential growth.

Thus, as devices and systems approach the nanoscale driven by the present trends in nanotechnology,[98] the strong relationship and sharp separation between transient and stationary responses is broken and blurred as the electron-nuclei interaction takes a major contribution. Thus from a system point of view, transient times in nanosystems are longer and may differ from one similar system to another as construction and distribution of atoms at the atomistic level need to be considered individually and not averaged over a large number of nuclei.

5.2 Set up of transient response measurement

To test the above assumptions we have performed several electrical experiments of non-chemically robust metallic structures. The structure we test is a piece of discontinuous gold film deposited on a silicon dioxide substrate. Scanning electron microscope (SEM) image shows that the gap between the gold islands is around 5 nm. There are two probe tips made of palladium and titanium at each side of the film to allow the application of electric fields. The separation between tips is 3 μm.

For the static current-voltage measurements, we combine the time-domain measurement function of the HP4145A and our custom designed Labview control program (detailed description in Figure 5.3). As shown in Figure 5.3, in the time-domain measurement, a fixed voltage is applied while the current is measured in every Δt'. Once the current is considered stable or stationary, the voltage goes down to zero and then the next voltage is applied.

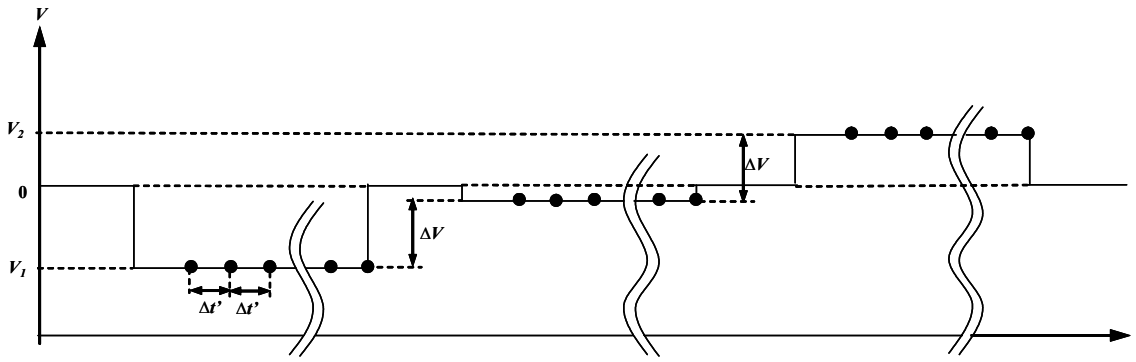

Figure 5.3. For the static current-voltage measurements, the applied voltage sweep starts at V_1 and is held constant at V_1. Current is measured in every Δt' and monitored. When the system enters into a stationary state, i.e., the current oscillates in a predictable manner, the measurement is stopped manually, the applied voltage is set to zero, and the next step follows.

5.3 Atomic scale response of discontinuous gold films

Before the static voltage sweep is applied, we performed a transient current voltage measurement. The voltage sweeps from 0 to 5 V with a step size of 0.05 V. Figure 5.4 shows a transient current voltage characteristic obtained from the device constructed by discontinuous gold film. The delay time is 0.1 sec. In the low voltage region, the current voltage curve is slightly smoother than the high voltage region.

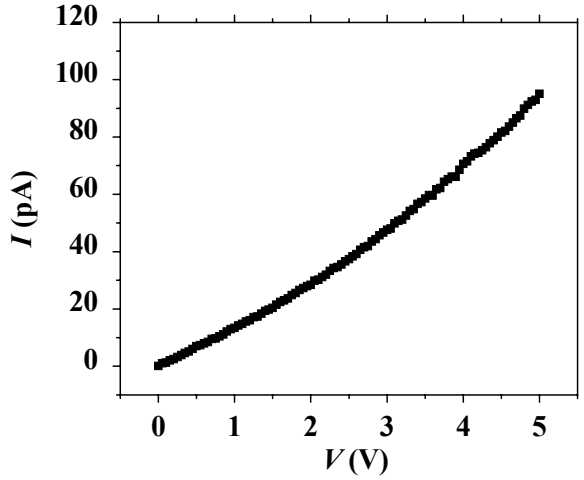

Figure 5.4. Transient current-voltage characteristic of a discontinuous gold film device

The static voltage sweeps from 0 to 5 V with a step size of 0.1 V. The current is recorded in intervals of 10 seconds. Figure 5.8 shows the measured current vs. time when applied voltage is varied from 0 V to 5V and then back to 0 V.. It is clear from the plot that for a fixed voltage, the current oscillates around a relatively stable value. This current oscillation is the "transient" behavior of the device, analog to macroscopic electrical devices, for example, a resistor, which yields a fixed current when a fixed voltage is applied. Consider now the discontinuous gold film as the structure under test, which is a 2-dimensional array of gold clusters with nanosized separations. Since there is no other substance inside the system, the conduction of current should depends on the conformations of the gold atoms. As the voltage is applied, the gold atoms diffuse by electron migration and form quantum nanosized filaments [58,65,99] (which are different in nature to widely studied classical microfilaments). As the current flows through the

nanofilaments, the local temperature inside the filaments also increases, which results in breaking of the nanofilaments. As a result, the current increases by forming of the nanofilaments and decreases by breaking of the nanofilaments forming a variety of nanocluster structures.

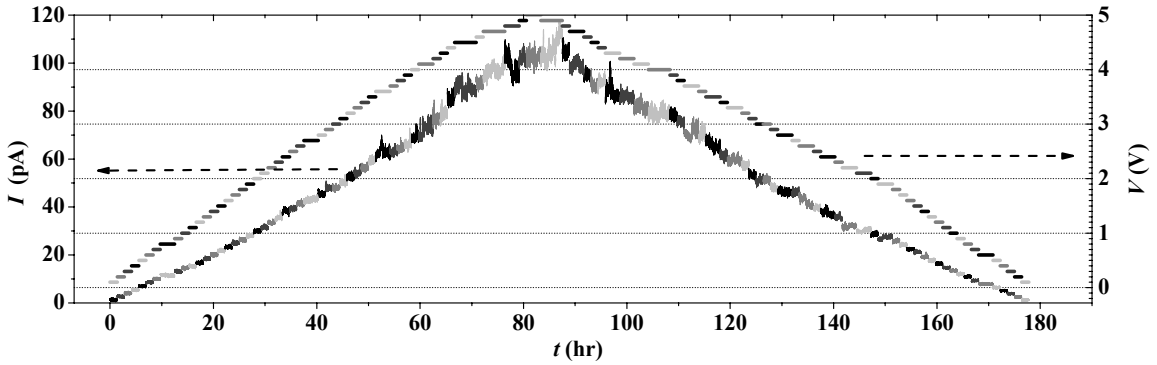

Figure 5.5 Time-domain current (axis on left side) vs. applied voltage (axis on the right) from 0 V to 5V and then back to 0 V.

Figure 5.6 displays the high and low values of the measured current connected by a vertical line with a tick mark displaying the mean value. We find that the higher the applied voltage, the more the current oscillates. This phenomenon is also clearly shown by observing the standard deviation of the current vs. voltage plot, as in Figure 5.7 Since the local temperature increases with the applied voltage, and the self-diffusion coefficient of the gold clusters increases accordingly,[100] the gold atoms vibrate more vigorously. This explains the strong oscillation of current at high voltages.

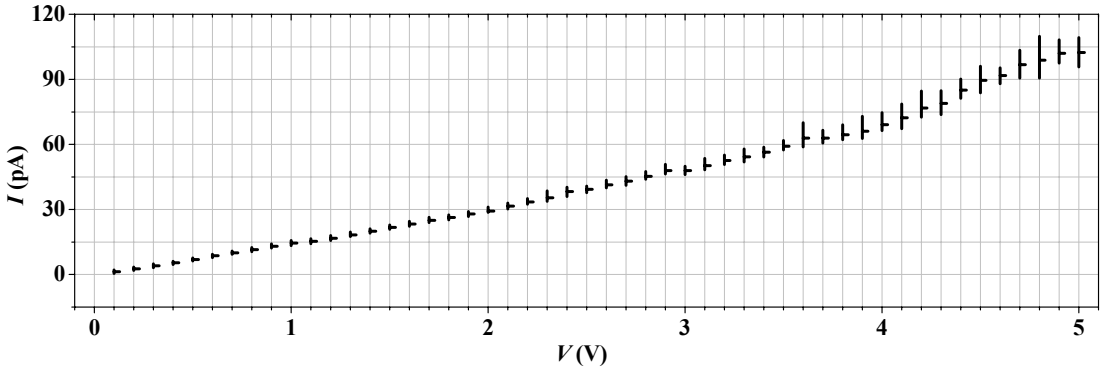

Figure 5.6. High and low values for the measured current in each voltage step. These values are connected by a vertical line with a tick mark displaying the mean value.

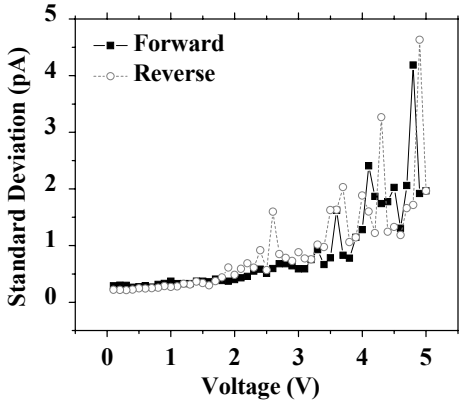

Figure 5.7. Standard deviation of the current flowing through the nanoCell at each applied voltage.

In addition, the level of uncertainty of the current also increases as the voltage increases. For instance, when applied voltage is 4.8 V, the current ranges from 80 pA to 100 pA. At the next step, i.e., V = 4.9 V, the current ranges from 97 pA to 108 pA. This

uncertainty have a strong impact on the transient current-voltage measurements yielding results in the choppy region of current-voltage curve in the high voltage area, as shown in Figure 5.4.

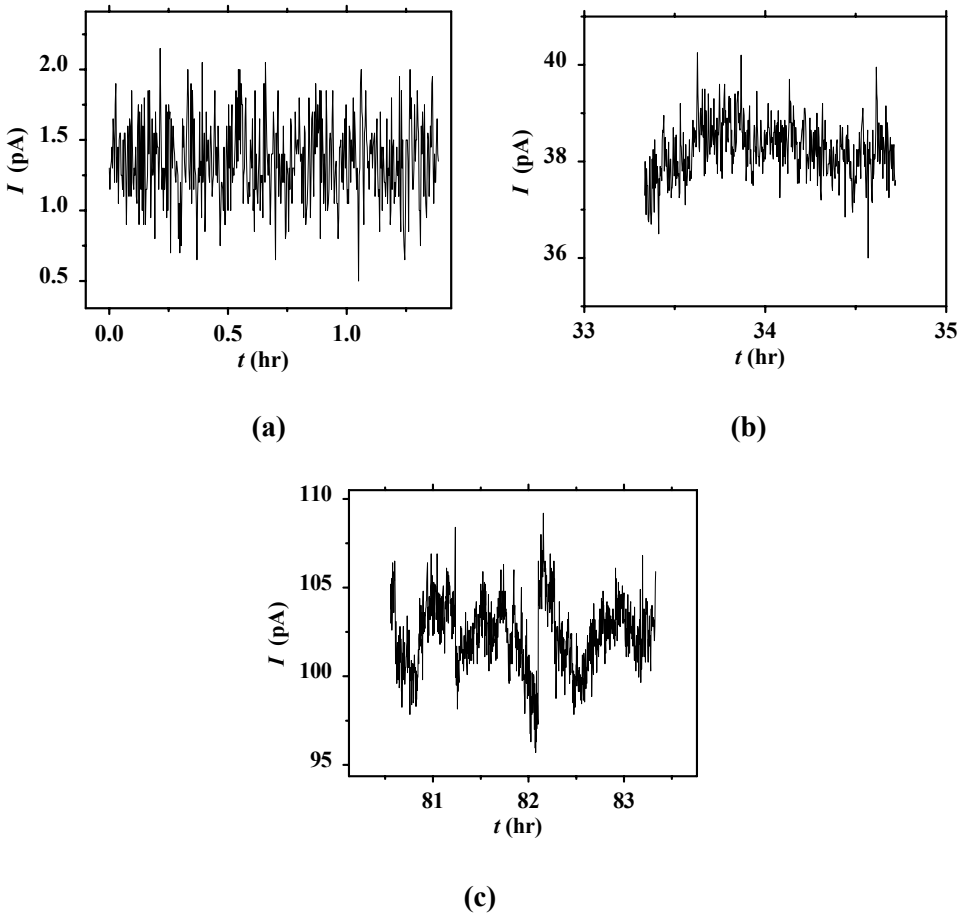

Figure 5.8. Detailed current vs. time plots. (a) current vs. time plot when applied voltage V = 0.1 V; (b) current vs. time plot when V = 2.4 V; (c) current vs. time plot when V = 5.0 V.

On the other hand, the current uncertainty also washes out or creates artificial NDR characteristic. If during a measurement, the current is 100 and 98 pA at 4.8 and

4.9 V, respectively, a negative differential resistance behavior is observed. However, if the current is 95 pA at 4.8 V and 100 pA at 4.9 V, then the NDR is not observed. In fact, NDR has been reported in several experimental papers[60,61,100] where only non "static" current-voltage measurements were performed.

In addition, it takes longer time for the device to reach a stationary state at higher voltage. As seen from Figure 5.8(a), when the applied voltage is 0.1 V, the system immediately enters into a quasi-static stage, i.e., although the current oscillates, the mean value of the current remains almost constant. However, at higher voltage, V = 5.0 V in Figure 5.8(c) for instance, the current oscillates for more than 4 hours and still does not reach to a static or quasi-static state.

5.4 Time dependent NDR and hysterisis

A large amount of work on single molecules has been reported indicating switching and NDR; it would be informative to re-analyze those results to find out whether they are really electrical in nature as it takes place in standard microelectronics or they are due to nuclear dynamics effects due to the strong interaction with the electron currents as the experiments reported in this work.

We actually provide a new perspective to study the electrical characteristic of nano systems at the atomistic level. As the dimensions of today's electronic devices scale down to the nano level, the relative amount of electrons flowing through the electronic system increases when compared to the microelectronic systems. This relatively increasing amount may result in the displacements of atoms, which in turn causes a more complex transient behavior due to the creation of conformational states of

gold clusters. The design of devices needs to consider this new conformational behavior and might utilize these inherent characteristics for some specific functions of nano circuits.

CHAPTER VI

VIBRONICS AND MOLECULAR POTENTIAL*

In this chapter, first the limitation of charge-current transport as a method for signal transmission is reviewed. Then the concept of vibronics is introduced and related research works are reviewed. Next the fundamental theory of molecular dynamic simulation is explained. And then the DSP techniques for encoding and decoding information are introduced. The results of the simulation are reported. Additionally, the molecular electrostatic potential method is explained and simulation results are provided. Finally, the feasibility of combining the two methods into programmable molecular array is investigated.

6.1 Limitations of charge-current transport as a method for signal transmission

One of the biggest problems faced in microelectronics development is the amount of power consumed by the various components in the circuit. This leads to extremely high amount of heat dissipated by the chips containing the integrated circuits. Although smaller transistors consume less power, as transistor density and speed rise, the overall chip consumes more power and generates more heat.

* Part of this chapter is reprinted with permission from Liuming Yan, Yuefei Ma, and Jorge M. Seminario, ***Encoding Information Using Molecular Vibronics,*** J. Nanosci. Nanotechnol. 6, 675–684 (2006).

Presently, a charge-current approach is widely used to process and transfer information in any integrated circuit. In this approach, the data is stored by induced charge separation in a memory device and data signals are transmitted and processed using electron current variations. Based on these methods, detection of signals and driving of circuits require minimum signal to noise ratio having strong effects in energy dissipation, which is the major limiting factor for charge-current approaches. Nevertheless, for practical but not optimal reasons, this approach is still being used in molecular electronics.[101]

The programmable molecular circuit, which is studied in the previous two chapters, is proposed to complement conventional electronic devices in order to reach molecular size devices. However, it may not be the right solution if it still uses the charge-current approach, i.e., the data is transmitted through the device using electron current variations, which may still lead, and certainly will, to the problem of energy dissipation.

6.2 Previous research work related to vibronics

Due to the limitations of charge transport, molecular vibronics combined with molecular electrostatic potential (MEP) is proposed as a substitute method to transport information.[102]

“Vibronics” stands for “Vibrational Electronics”. When a signal is injected into a molecule, the vibrational mode of the atoms around the injection point changes. Since the atoms in a molecule are bonded to each other, the changes in the vibrational states of the molecule triggers the movement of atoms, which transfers to their neighbor atoms by

means of bond bending, bond stretching, van der waal interactions, coulomb interaction between charges, etc.[103] Thus using vibronics, the signals are transferred through the molecule. [101,104,105]

Our molecular dynamics (MD) simulation demonstrates that a signal can be encoded and modulate the vibrational state at one site of the molecule, and the propagation of the vibrational movement allows the vibrational signal be detected at the other site of the molecule. Thus the molecule can be used as a single signal processing unit. Digital signal processing techniques are used to encode and decode the signals from molecular vibrational states. The typical molecular vibrations are in the range of terahertz (THz) thus starting a new era for terahertz signal transmission techniques in molecular electronics. All this work is triggered by preliminary molecular dynamics simulations performed in a "nanoCell" where the modulation of a signal was performed[106,107]. It should be noted that to implement vibronics in real electrical circuits, transducers are necessary to convert the electrical signals to vibrational signals and vibrational to electrical.

6.3 Molecular dynamics simulation

Atoms in molecules vibrate around their equilibrium position. Usually, the vibrational modes are assigned to certain bond length stretching or bond angle bending, etc.; however, bond length stretching or bond angle bending can cause the vibrational movement of other atoms that are directly or indirectly bonded to this vibrating bond. Therefore a vibrational mode is actually the vibrational movement of a few atoms in a molecule. Although the propagation of vibrational movements are beyond the ability of

direct observation by modern experimental techniques; modern computer simulation techniques allow us to trace the trajectory of all the atoms; therefore, to view the vibrational movements of individual atoms in a molecule.

Molecules are modeled as a collection of mass centers which may be a single atom or a group of atoms (united atom) that are part of the molecule. The mass centers, which will generally be called the atoms in this context, bear electric charges. The atoms interact with each other via bonding forces, non-bonding forces, and electrostatic forces. The total potential energy of a molecular system is $u(\mathbf{R}_1,\cdots,\mathbf{R}_M)$, where $\mathbf{R}_1,\cdots,\mathbf{R}_M$ are coordinates of all *M* atoms in the system, can be written as the sum of all the interactions:

$$u(\mathbf{R}_1,\cdots,\mathbf{R}_M)=\sum_{\rho}^{bonds}\frac{1}{2}k_\rho^{bond}(r_\rho-r_{\rho 0})^2+\sum_{\eta}^{angles}\frac{1}{2}k_\eta^{angle}(\theta_\eta-\theta_{\eta 0})^2$$
$$+\sum_{\delta}^{dihedrals}k_\delta^{dihe}[1+\cos(n_\delta\phi_\delta+\phi_{\delta 0})]+\sum_{\alpha}\sum_{\beta>\alpha}4\varepsilon_{\alpha\beta}\left(\left(\frac{\sigma_{\alpha\beta}}{r_{\alpha\beta}}\right)^{12}-\left(\frac{\sigma_{\alpha\beta}}{r_{\alpha\beta}}\right)^{6}\right)+\sum_{\alpha}\sum_{\beta>\alpha}\frac{q_\alpha q_\beta}{4\pi\varepsilon_0\varepsilon_r r_{\alpha\beta}} \tag{6.1}$$

The terms in the right hand of the equation (5.1) represents, respectively, bond stretching potential running over all the bonded atom pairs, bond angle bending, torsional rotation, van der Waals interaction (Lennard-Jones) between non-bonded atoms, and electrostatic interaction between charges. The forces acting on each atom α are computed from the potential energy:

$$\mathbf{f}_\alpha=-\nabla_\alpha u(\mathbf{R}_1,\cdots,\mathbf{R}_M)\qquad(\alpha=1,\cdots M) \tag{6.2}$$

And therefore, the atomic motions of the system could be predicted using the Newton's equations:

$$\frac{d^2\mathbf{R}_\alpha}{dt^2} = \frac{\mathbf{f}_\alpha}{m_\alpha} \qquad (\alpha = 1, \cdots, M) \tag{6.3}$$

where $\mathbf{R}_\alpha$ represents the coordinate of atom α with mass m_α, and *t* is time.

An MD simulation is the numerical integration of the Newton's equations (3) typically following these steps:[103] the coordinates and velocities of all the atoms are set to initial values randomly such that the average kinetic energy of the system is equal to the simulation temperature, and the total momentum is zero. Then, a geometry optimization is run to relax the system to a stable configuration. Then, the actual MD simulation, the integration of the Newton's equations of motion is run. Since the coordinates are known, all the forces acting on each atom are calculated using equation (5.2), and the accelerations, $\mathbf{a}_\alpha(t_i)$ ($t_i = t_0$ for the first step) are computed as:

$$\mathbf{a}_\alpha(t_i) = \frac{\mathbf{f}_\alpha(t_i)}{m_\alpha} \qquad (\alpha = 1, \cdots, M) \tag{6.4}$$

The velocities are updated at half time steps [103,108,109]:

$$\mathbf{v}_\alpha\left(t_i + \frac{1}{2}\Delta t\right) = \mathbf{v}_\alpha\left(t_i - \frac{1}{2}\Delta t\right) + \mathbf{a}_\alpha(t_i)\Delta t \qquad (\alpha = 1, \cdots, M) \tag{6.5}$$

and the coordinates are updated at each time step.

$$\mathbf{R}_\alpha(t_{i+1}) = \mathbf{R}_\alpha(t_i) + \mathbf{v}_\alpha\left(t_i + \frac{1}{2}\Delta t\right)\Delta t \qquad (\alpha = 1, \cdots, M) \tag{6.6}$$

Using the updated coordinates, new forces are calculated; therefore, new velocities and coordinates are calculated. This process is repeated millions of time steps.

During the simulation, two atoms F_1 and F_2 from each end of the molecules are fixed. The vibrational signal is injected into the molecule following every step of updating coordinates. In this extra step, an atom X bonded to one of the fixed atoms, F_1 for example, oscillates along the direction X-F_1 at the distance defined by the modulated signal. The step time is set to 1 fs, and 200,000 equilibration steps are run before the production runs to relax the system. Then, 1,000,000 production steps are run corresponding to 1 ns, and the coordinates of all the atoms at each step are recorded in a trajectory file.

6.4 DSP techniques for encoding and decoding signals

From the trajectory file, time series of bond lengths, which contain the vibrational information, are calculated at each time step, and digital signal processing (DSP) techniques are applied to analyze the signal transmission along the molecule.

6.4.1.1 Modulation techniques

Before the signal is transmitted in a molecule, it has to be modulated with a carrier signal. This carrier signal is usually a sinusoidal signal. The main reason for modulation is that it makes the signal properties physically compatible with the propagation medium, i.e., the molecule.

Amplitude modulation (AM) and frequency modulation (FM) are two methods frequently used in signal modulation. In AM, amplitude of a carrier wave is varied in direct proportion to that of a modulating signal; while in FM, frequency of the carrier is varied.

In our simulation, the frequency of the carrier wave is selected as the intrinsic vibrational mode of the backbone of the molecule. For example, for polypeptide, the frequency f_c is 23.81 THz. Thus the carrier wave becomes

$$x_c(t_i) = \sin(2\pi f_c t_i) \tag{6.7}$$

For the sake of identifying, the modulating signal, i.e., the actual information signal) is designed to consist of a series of squares and triangles. Thus the AM signal is:

$$r(t_i) = r_0 + 0.0065 \times (1 + 0.538 x_n(t_i)) \sin(2\pi f_c t_i) \tag{6.8}$$

where r_0 is the equilibrium bond length between atom F_1 and X, $x_n(t_i) = 2x_A(t_i) - 1$ is the normalized modulating signal at time t_i which coincides with the time step of MD simulation.

The frequency modulating (FM) wave, $x_F(t_i)$, is slightly different from the AM signal that it consists a series of trapezoids and triangles. The FM signal is:

$$r(t_i) = r_0 + 0.01 \times \sin(2\pi(f_c t_i + f_m \tau_i)) \tag{6.9}$$

where f_m is the modulation index and τ_i is given by

$$\tau_i = \int_0^{t_i} x_F(t) dt \tag{6.10}$$

6.4.1.2 Decoding information

Digital signal processing (DSP) techniques are used to analyze bond length vibrations signals in the molecular wires.[110,111] At a sampling period of 1.0 fs, which is identical to the time step for the MD simulations, a discrete time series

$D_{\alpha\beta}[i, i = 0, 1, \cdots, N-1]$ is calculated from $\mathbf{R}_\alpha$ and $\mathbf{R}_\beta$, the *i*-th step coordinates of atom α and β, respectively, recorded in trajectory file. Thus, $D_{\alpha\beta}(i)$ can be expressed as:

$$D_{\alpha\beta}(i) = \left|\mathbf{R}_\alpha(t_i) - \mathbf{R}_\beta(t_i)\right| \quad (i = 0, 1, \cdots, N-1) \tag{6.11}$$

where N is the total number of the steps used in the MD simulation.

The time series $D_{\alpha\beta}[i, i = 0, 1, \cdots, N-1]$ contains both the direct (DC) and alternating (AC) components. The AC series $\tilde{D}_{\alpha\beta}[i, i = 0, 1, \cdots, N-1]$, is calculated from the initial bond length series $D_{\alpha\beta}[i, i = 0, 1, \cdots, N-1]$ by subtracting its series average $D_{\alpha\beta,0}$, which is the DC component.

The frequency spectrum of the time domain signal $F_{\alpha\beta}[k,\ k = 0, 1, \cdots,\ N-1]$ is obtained by a fast Fourier transform (FFT) of the AC time series $\tilde{D}_{\alpha\beta}[i, i = 0, 1, \cdots, N-1]$:[110,111]

$$F_{\alpha\beta}[k,\ k = 0, 1, \cdots,\ N-1] = \sum_{i=0}^{N-1} \tilde{D}_{\alpha\beta}(i) e^{-j2\pi ik/N} \tag{6.12}$$

$$F_{\alpha\beta}(k) = A_{\alpha\beta}(k) e^{j\varphi_{\alpha\beta}(k)} \tag{6.13}$$

where N is the total number of samples in the series, $A_{\alpha\beta}(k)$ and $\varphi_{\alpha\beta}(k)$ are the amplitude and phase of the frequency domain signal, respectively.

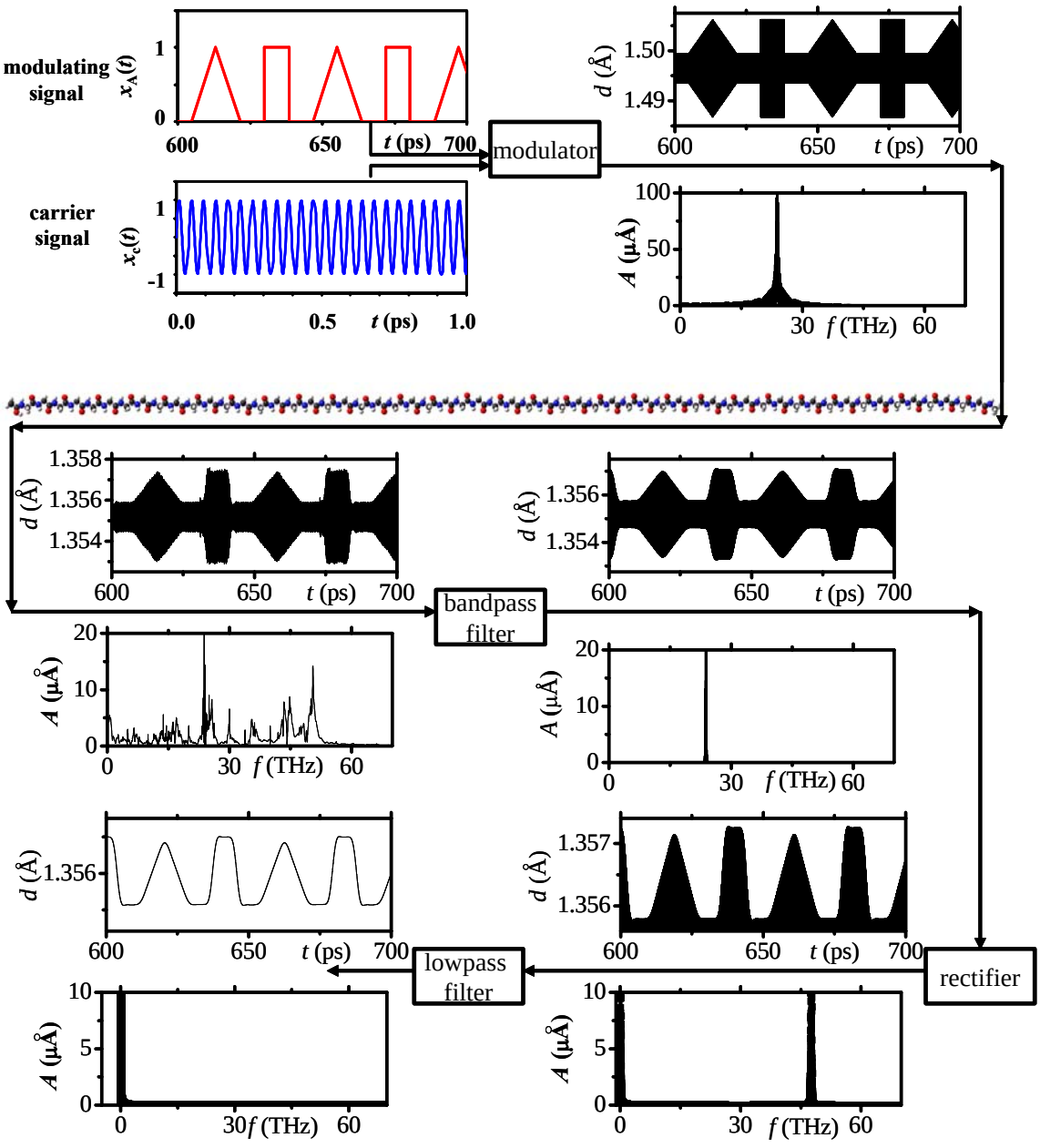

Figure 6.1. DSP techniques used for the processing of signals transmitted through molecule GLY58 via amplitude modulation.

To recover signal from an AM wave, the time domain AC series are filtered using a Bessel bandpass filter centered at a carrier frequency and with a bandwidth of around 1 THz. The Bessel filter is selected because its output closely resembles the original waveform adding small and gentle edge rounding.[110] This bandpass filter filters out all the low frequency and high frequency vibration signals and only allows vibrational signal centered at the carrier frequency f_c with a narrow band to pass. Then, the bandpass filtered signal is rectified using a rectifier and the signal is recovered by passing the rectified signal through a Bessel lowpass filter with a small cutoff frequency; these last two steps can also be done using a peak detector. Figure 6.1 shows an example of AM signal processing in molecule GLY58.

The demodulation of the FM signal is carried out by means of slope detector. [112] First, the time domain AC series, which are obtained as described in the AM signal recovery, are filtered using a Bessel bandpass filter centered at carrier frequency. Then the bandpass filtered signal is clipped to constraint the amplitude variation to and thus eliminating the thermal noise due to the finite temperature. The clipped signal is demodulated by a slope demodulator, a special Bessel bandpass filter, which has a center frequency slightly larger than the carrier frequency, and the entire frequency variation of the FM signal falls on the linear part of the left slope of the frequency response curve of the filter.[110] Figure 6.2 shows the frequency response of the slope detector used for demodulate signal transmitted through molecule GLY58. Since the carrier frequency is 23.81 THz and the frequency variation of the bandpass filtered signal is ±0.2 THz, the center and bandwidth of the slope demodulator are set to 24.9 THz and 2.6 THz,

respectively. Finally, the signal is recovered by passing the slope-detected wave through a full wave rectifier and a lowpass filter. Figure 6.3 shows an example of FM signal processing in molecule GLY58.

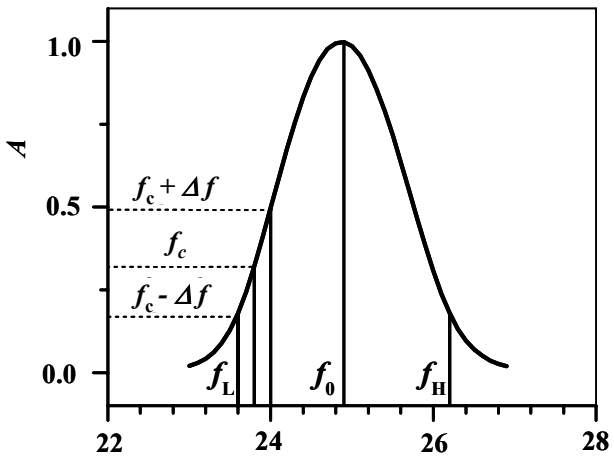

Figure 6.2. Frequency response of the slope demodulator, a special Bessel bandpass filter, used for FM signal demodulation. The center frequency f_0 is 24.9 THz and the bandwidth is 2.6 THz. The lower and upper cut-off frequencies of the slope demodulator f_L and f_H, are 23.6 and 26.2 THz, respectively. The carrier signal has a center frequency f_c of 23.81 THz. and frequency variation Δf of 0.2 THz.

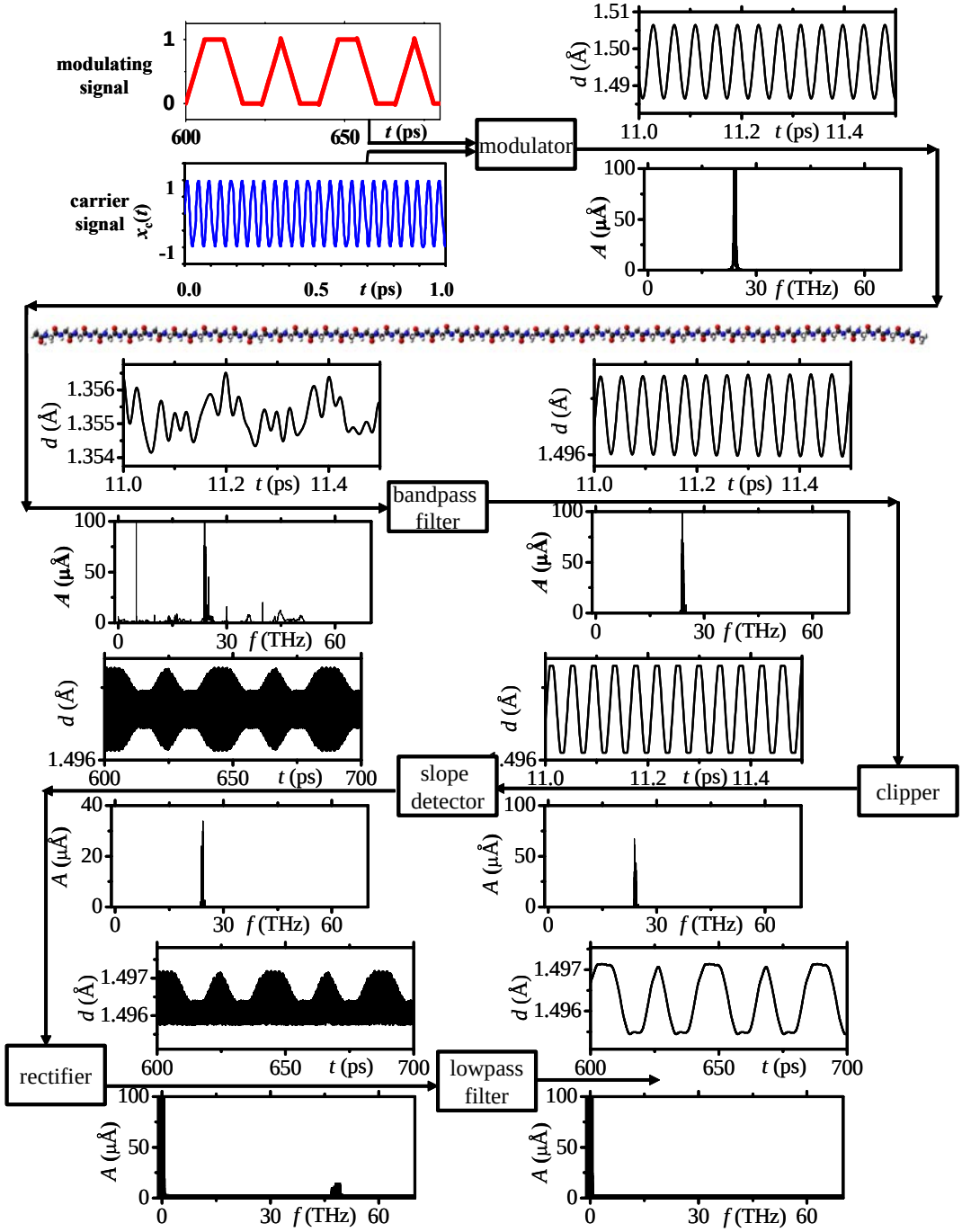

Figure 6.3. DSP techniques used for the processing of signals transmitted through molecule GLY58 via amplitude modulation.

6.5 Simulation results of molecular vibrational signal transmission

MD simulation of molecular vibrational signal transmission is carried out for molecule GLY58 at room temperature (298.1 K) for 1 nano-second. The sampling time, i.e., the time step is 1 femto-second and total number of steps is 1,000,000. The molecular structure of GLY58 is shown in Figure 6.4. It consists of 58 glycine residues and a methylamine cap at the C-terminus and acetyl at N terminus. The total length of the molecule is around 218 Å. The intrinsic vibrational mode of the backbone of this molecule is 23.81 THz.

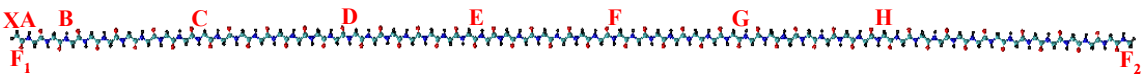

(a)

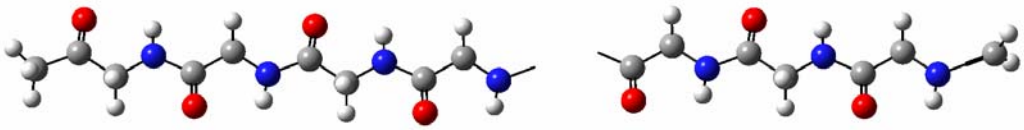

(b)

Figure 6.4. Molecular structure of GLY58. (a) Entire molecule. (b) Detailed structure of GLY58. The grey atoms are carbon (C); the blue nitrogen (N); the red oxygen (O); the white hydrogen (H).

During MD simulation, two carbon atoms, F_1 and F_2, from each cap are held fixed. Input signals are couples to the carbon atom X that is bonded to F1 at left. The signals are detected at difference sites A, B, C, D, E, F and G in the backbone of GLY58.

Shown in Figure 6.4, sites A, B, C, D, E, F and G are located at 1.4, 8.3, 34, 67, 90, 116, 142, 168 Å from the input site, respectively.

6.5.1 Amplitude modulated signal transmission

Amplitude modulated signal is injected into the molecule GLY58 by coupling the input signal expressed in Equation (5.8) into the movement of carbon atom X as indicated in Figure 6.4. The time domain signal at site A, 1.4 Å from the input site X, is shown in Figure 6.5a. In the frequency domain signal (Figure 6.5b) calculated by FFT, the carrier frequency is clearly shown as a peak in 23.81 THz. Figure 6.5c and d show the time and frequency domain signals detected at site E, which is 90 Å from the input site. Apparently, the frequency domain signal carries not only the carriers signal, shown as a peak at 23.81 THz in Figure 6.5d, but also other molecular vibrational signal due to thermal noise, solvent effect, etc. The modulating signal is recovered as described in section 6.4.1.2 The Bessel bandpass filter is centered at 23.81 THz with a bandwidth of 0.7 THz. The Bessel lowpass filter has the cut-off frequency of 0.5 THz. The recovered signal is shown in Figure 6.5e. The similarity between the original modulating signal and the recovered signal clearly tells us that the recovered signal is the original modulating signal that propagates from site X.

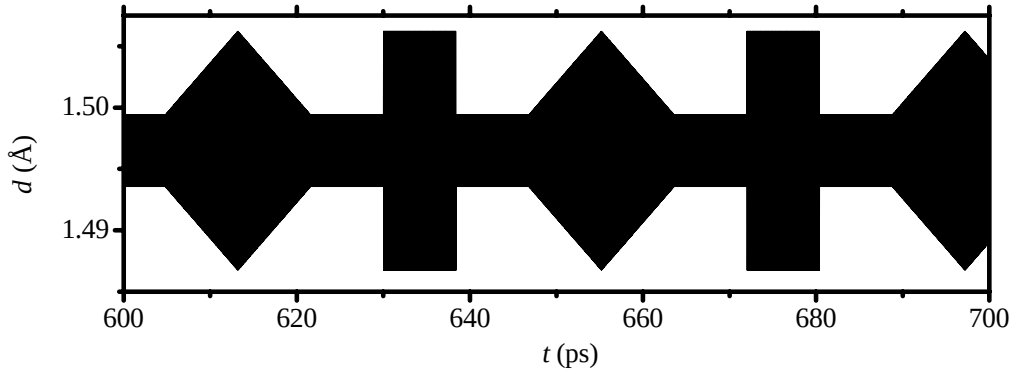

(a)

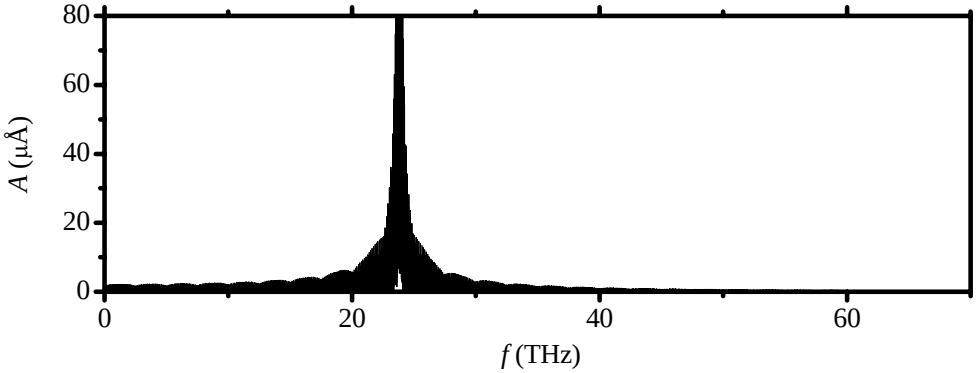

(b)

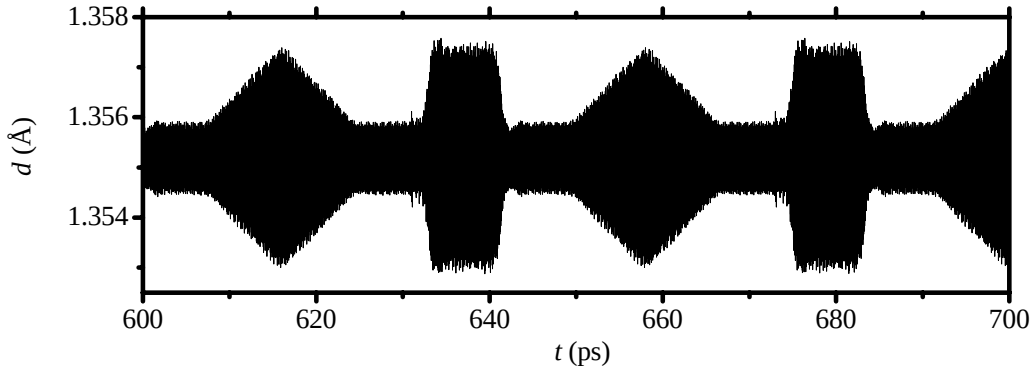

(c)

Figure 6.5. Signal transmission along GLY58 using amplitude modulation by a carrier at 23.81 THz. (a) Time domain vibrational signal detected at a remote site A; (b) frequency domain vibrational signal at site A; (c) time domain vibrational signal detected at a remote site E; (d) frequency domain vibrational signal at site E; (e) Signal recovered using DSP techniques.

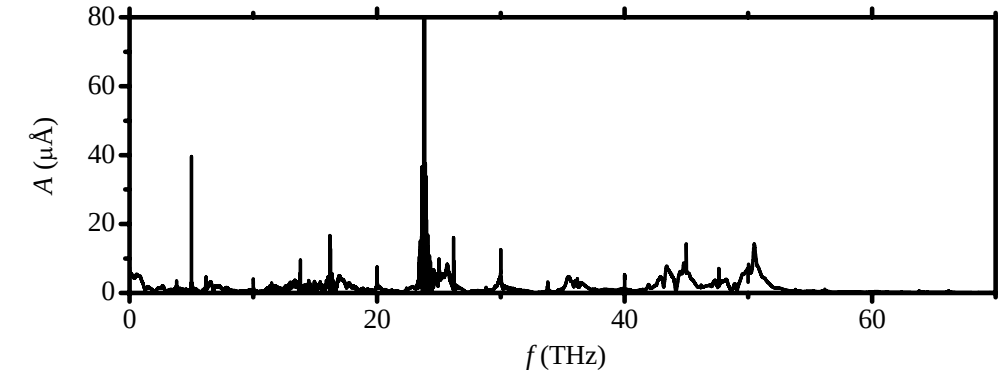

(d)

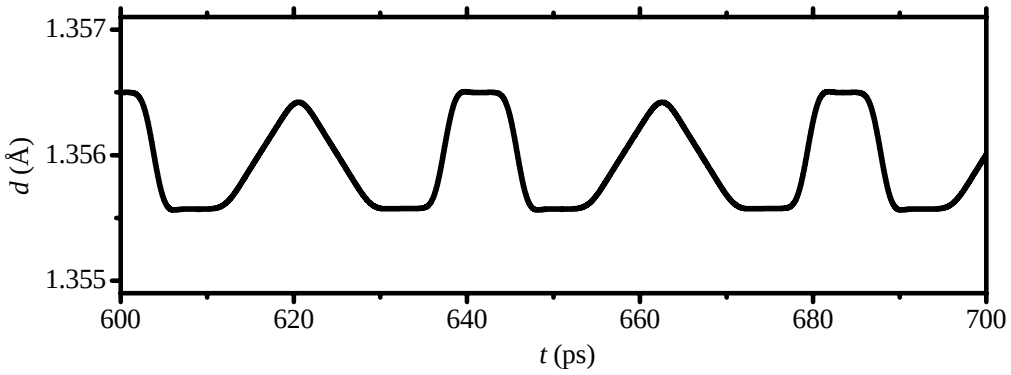

(e)

Figure 6.5 (Continued)

6.5.2 Time delay of molecular vibrational signal transmission using AM

Figure 6.6 shows the recovered AM AC signals at different sites in molecule GLY58 as indicated in Figure 6.4a. The average velocity of the vibronic signal can be determined following the time delays as signal propagates along the molecule. From Figure 6.6, the peak of the first triangle shape signal is located at 617.705 ps at site A and 622.775 ps at site H. The distance between site A and H is 166.6 Å. This yields an

speed of 3286 m/s. When this type of information is collected at all sites, an average speed of 3279 m/s will be obtained (Figure 6.7). Although, this speed is at least one order magnitude smaller than the speed of electrons in a bulk semiconductor, the advantage of our vibronic approach is that the energy needed to transfer one bit of information is a fraction of eV as compared to the few ten-thousands of eV needed under the present electron current approaches.

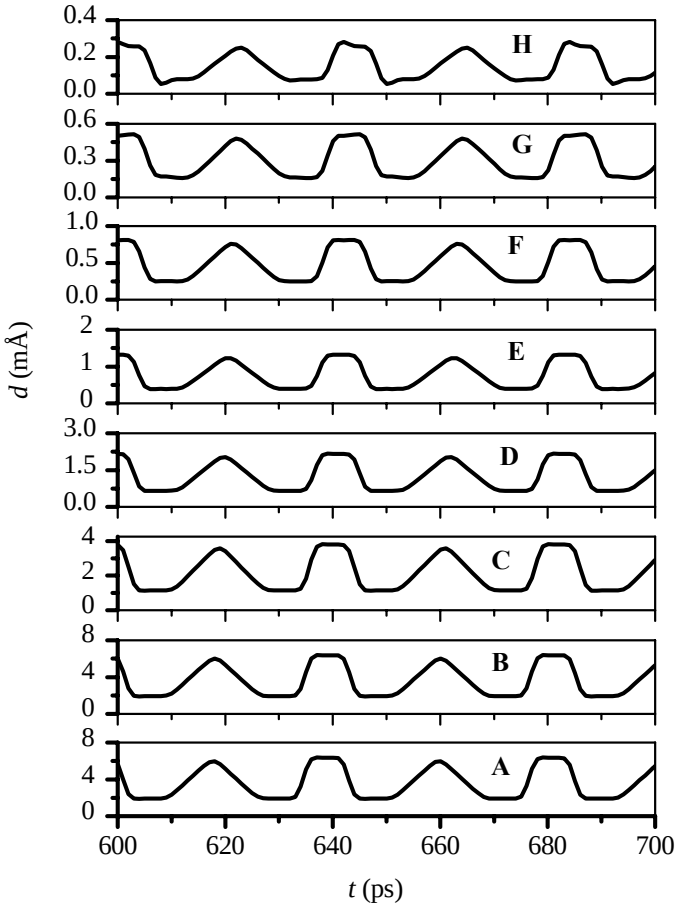

Figure 6.6. Detected AM AC signals in molecule GLY58 at different sites as indicated in Figure 6.4a.

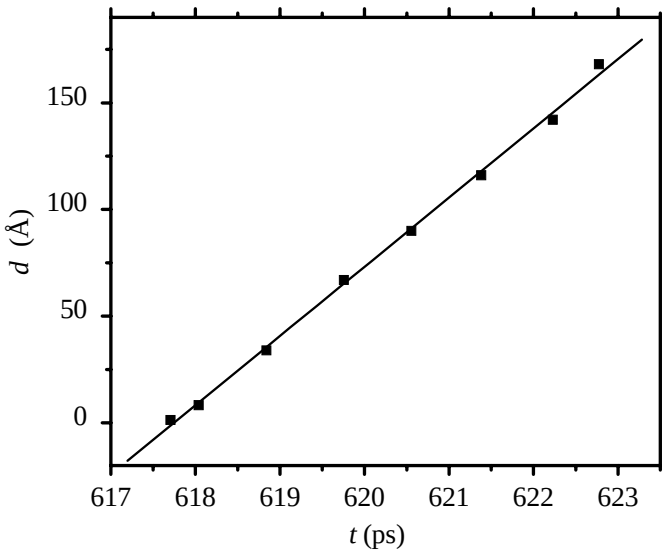

Figure 6.7. Distance versus time-delays of the first triangle apex from AM signals in Figure 6.6.

6.5.3 Noise and attenuation of molecular vibrational signal transmission using AM

Signal-to-noise ratio is a determining factor in any data processing systems. As signal travels, its amplitude decreases to the point that is washed out by the noise (usually thermal noise). Amplitude modulation is prone to this as noise simply adds to the signal. The vibronic approach is suited to interconnect molecular and nano devices that cannot be interconnected by standard lithographic techniques, thus in the range of nanometers. Figure 6.6 shows that the signal keeps its original shape after it travels to site G at 14.2 nm, which is a reasonable distance for a nano-sized circuit. The amplitude of the signal attenuates exponentially with a factor of 0.0195 $Å^{-1}$ (Figure 6.8). Thus for a distance of 1.0 nm, the signal amplitude is still 82.3 % of its original amplitude.

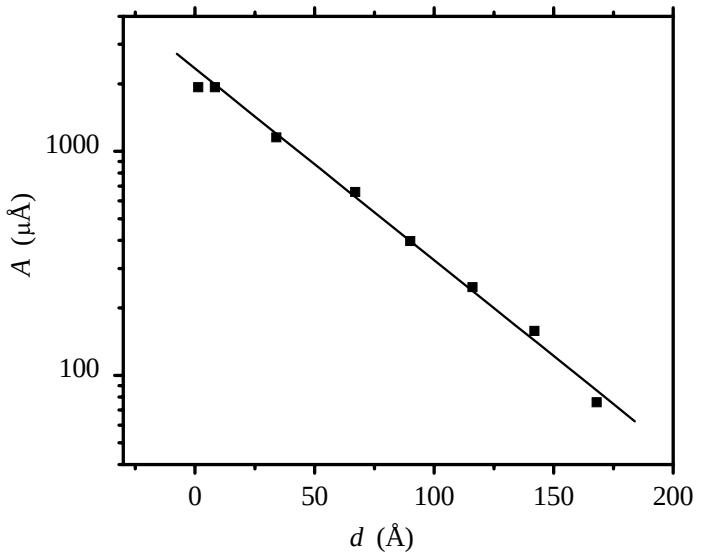

Figure 6.8. Attenuation of the AM signal along molecule GLY58.

6.5.4 Effects of different carrier frequency on AM signal transmission

When signals are coupled to atom X (forced movement of X), the atom that is directly bonded to X will also be driven to vibrate at the applied frequency; and this atom will again drive another bonded atom. As this process progresses, the vibrational signal propagates. As is discussed before, the carrier frequency of the signal should be one of the intrinsic vibrational frequencies of the backbone in the molecule. We compare the response to two signals with different carrier frequencies: one at 23.81 THz corresponding to one of the intrinsic vibrational mode; and the other at 71.43 THz corresponding to a frequency range with no intrinsic vibrational modes. Figure 6.9 compares the evolution of these two signals. Notice that the later signal at 71.43 THz is

much faster than the former that corresponds to an intrinsic mode of the polypeptide; actually, it almost dissolved immediately after it propagates through site A.

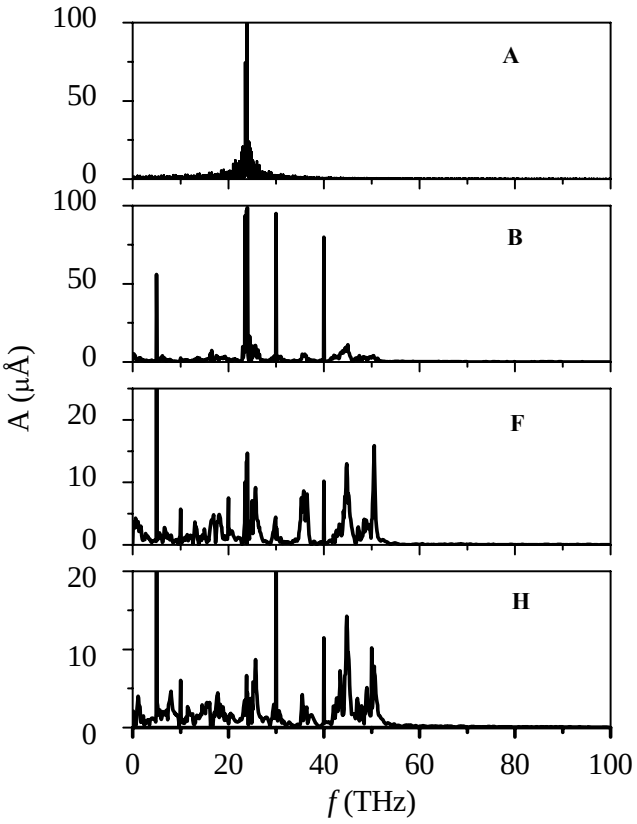

(a)

Figure 6.9. Frequency response of GLY58 of different AM carrier frequencies. (a) Frequency spectrums at site A, B, F and H under excitation frequency of 23.81 THz; (b) frequency spectrums at site A, B, F and H under excitation frequency of 71.43 THz.

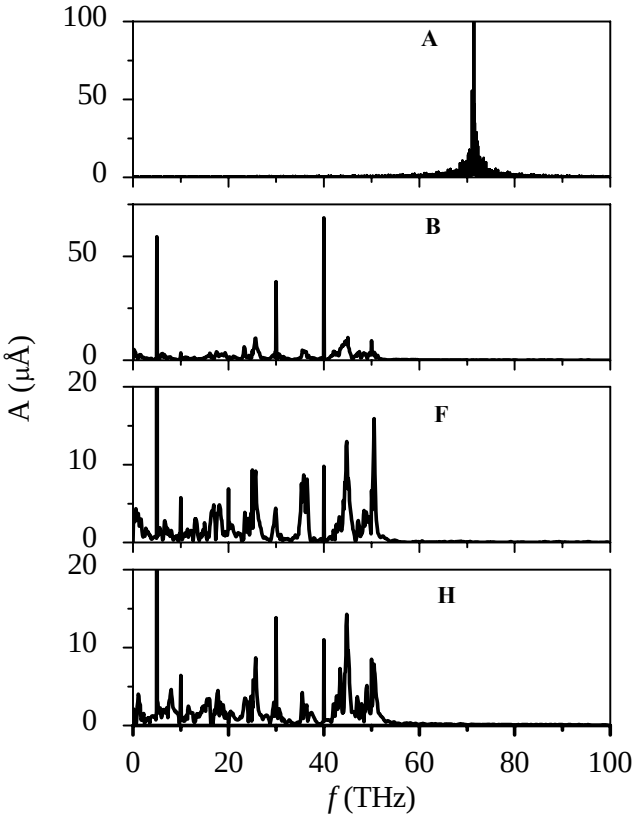

(b)

Figure 6.9 (Continued)

6.5.5 Molecular vibrational signal transmission using frequency modulation

Frequency modulated signal is injected into the molecule GLY58 by coupling the input signal expressed in Equation (5.9) into the movement of carbon atom X as indicated in Figure 6.4. The time domain signal at site A, 1.4 Å from the input site X, is shown in Figure 6.10a. Since the signal is only varied by frequency, it is difficult to distinguish the change in the time domain. In the frequency domain signal (Figure

6.10b), the carrier frequency is clearly shown as a peak in 23.81 THz. Figure 6.10c and d show the time and frequency domain signals detected at site G, which is 142 Å from the input site. The modulating signal is recovered as described in section 6.4.1.2 The first Bessel bandpass filter is centered at 23.81 THz with a bandwidth of 1.0 THz. The bandpassed AC signal is clipped to constrain the amplitude variation to ± 200 μÅ. The slope demodulator is centered at 24.9 THz with a bandwidth of 2.6 THz and the Bessel lowpass filter has a cut-off frequency of 0.5 THz. The recovered signal is shown in Figure 6.10e.

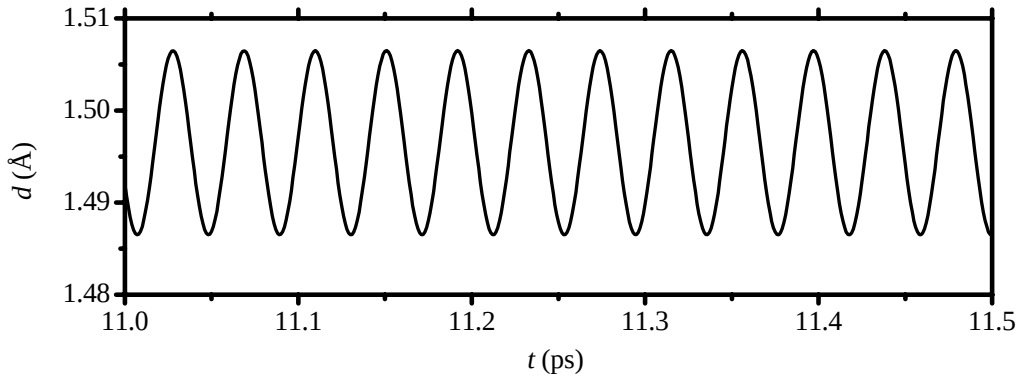

(a)

Figure 6.10. Signal transmission along GLY58 using frequency modulation by a carrier at 23.81 THz. (a) Time domain vibrational signal detected at a remote site A; (b) frequency domain vibrational signal at site A; (c) time domain vibrational signal detected at a remote site G; (d) frequency domain vibrational signal at site G; (e) Signal recovered using DSP techniques.

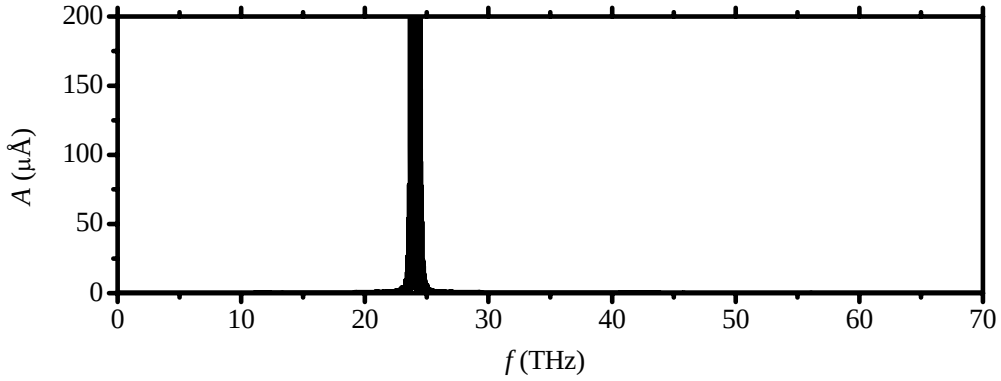

(b)

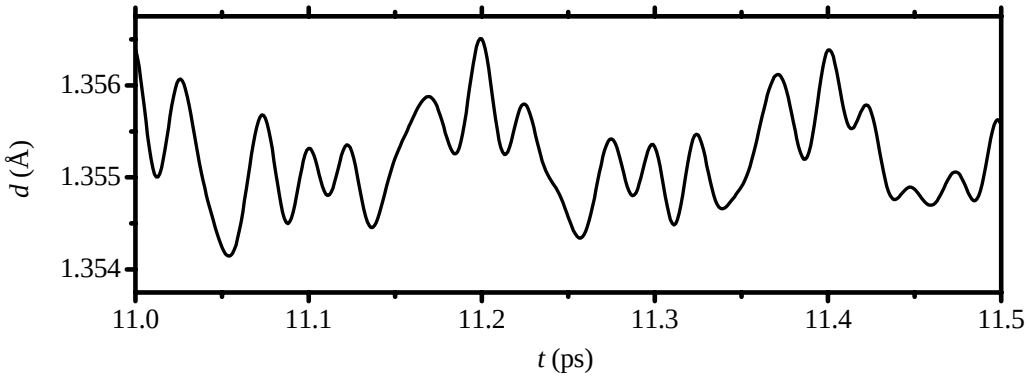

(c)

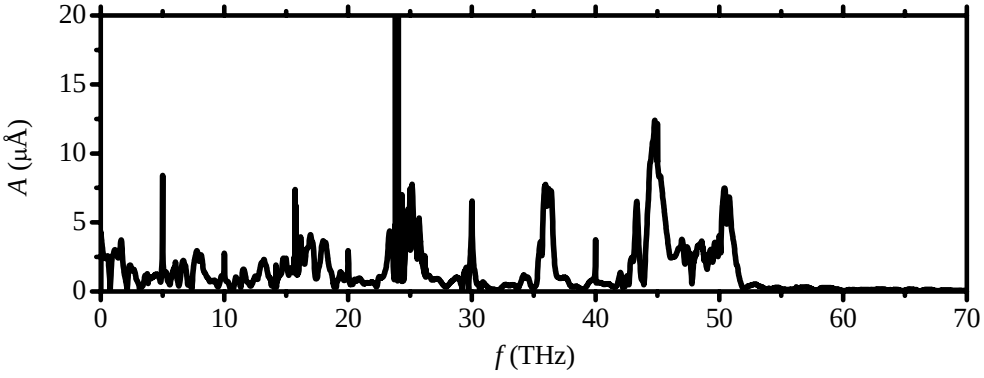

(d)

Figure 6.10 (Continued)

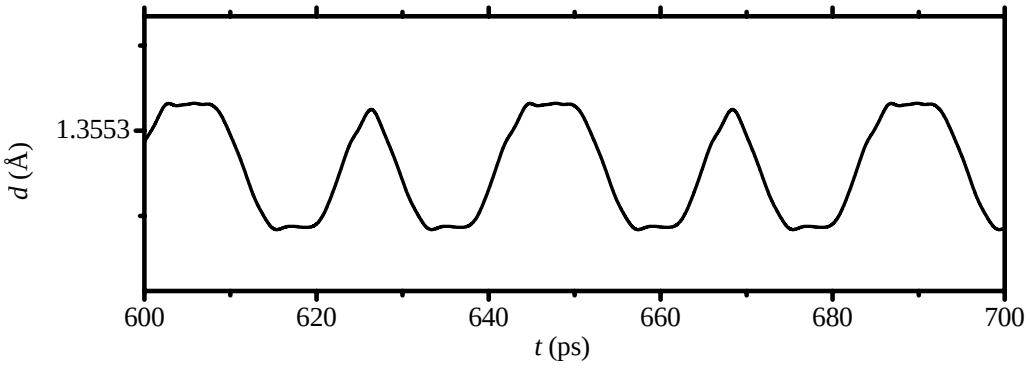

(e)

Figure 6.10 (Continued)

6.5.6 Time delay and attenuation of molecular vibrational FM signal transmission

Figure 6.11 shows the recovered FM AC signals from site A, B, C, D, E, F, G, and H in molecule GLY58. The time delays are clearly shown as the signal transmitted from site A to site H. From the location of the first triangular apexes, a signal transmission speed of 3108 m/s is obtained (Figure 6.12). Since FM signals are encoded in the time variation of carrier frequency, amplitude attenuation does not affect signal recovering if the signals are strong enough to be detected. It could be found that the noise level of FM is much lower than that of AM by comparing between the recovered AM signals in Figure 6.6 and FM signals in Figure 6.11.

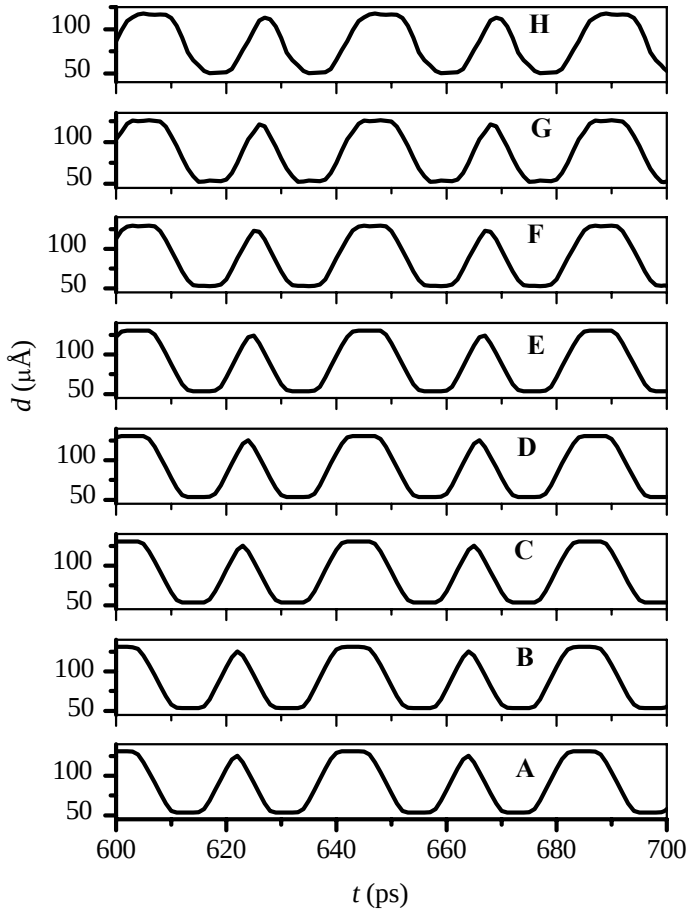

Figure 6.11. Detected FM AC signals in molecule GLY58 at different sites as indicated in Figure 6.4a.

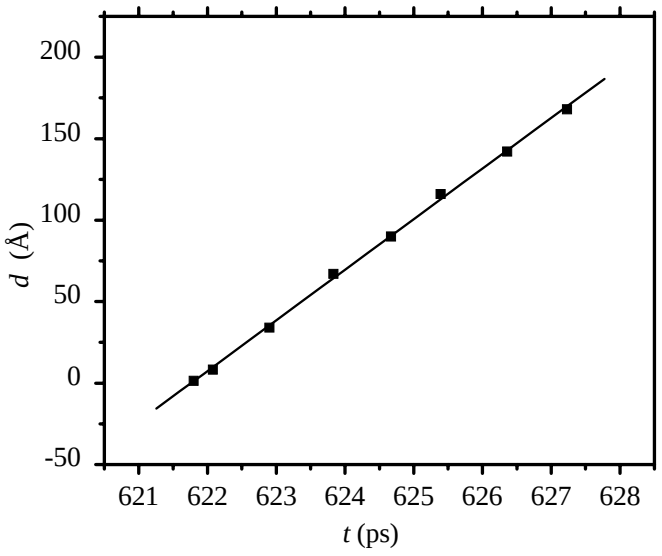

Figure 6.12. Distance versus time-delays of the first triangle apex from FM signals in Figure 6.11.

6.6 Using of molecular potential to process information

For any molecular system, there is an electricstatic potential ϕ. The electrostatic potential ϕ at a point P is defined as the reversible work per unit charge needed to move an infinitesimal test charge Q_t from infinity to P.[113] The molecule can be viewed as a collection of point-charge nuclei and electronic charge smeared out into a continuous distribution. The probability of finding a molecular electron in a volume $dV = dxdydz$ is[113]

$$\rho(x, y, z) = n \sum_{allm_x} \int \cdots \int \left|\psi(x, y, z, x_2, ..., z_n, m_{s1}, ..., m_{sn}\right|^2 dx_2 \cdots dz_n \quad (6.14)$$

where ψ is the electronic wave function of the system comprising n electrons, and $\left|\psi(x_1,...,z_n,m_{s1},...,m_{sn}\right|^2 dx_1dy_1dz_1\cdots dx_ndy_ndz_z$ is the probability of simultaneously finding electron 1 with spin m_{s1} in volume $dx_1dy_1dz_1$ at (x_1,y_1,z_1), electron 2 with spin m_{s2} in volume $dx_2dy_2dz_2$ at (x_2,y_2,z_2), and so on.[113] The wave function ψ can be obtained by solving Schrödinger equation numerically using Gaussian 03 program.

Knowing the probability, we know the amount of electronic charge in dV is $-e\rho dV$. The molecular electrostatic potential ϕ is the addition of the molecular electric charge and of the nuclei α. Thus the molecular electrostatic potential at point (x_1,y_1,z_1) can be expressed as[113]

$$\phi(x_1,y_1,z_1)=\sum_{\alpha}\frac{Z_\alpha}{r_{1\alpha}}-\iiint\frac{\rho(x_2,y_2,z_2)}{r_{12}}dx_2dy_2dz_2 \qquad (6.15)$$

where Z_α is the nuclei charge, r_{12} is the distance between points 1 and 2 and the integration is over all space. Likewise, the molecular electrostatic potential is calculated using the Gaussian 03 program.

As an example, the molecular electrostatic potentials of water are plotted as in Figure 6.13. Positive and negative potentials can be easily distinguished by the color, as positive is blue and cyan and negative is red and yellow. Although the regions around the nuclei show positive potential, the sites outside the molecule show potential either positive (blue) or negative (red) depending on electron distributions around the molecule. For the singlet ground state (Figure 6.13a), the negative potential is located at the lower sites of the molecule; while for the triplet excited state, which is less angular, the negative effect of the electrons can be see on both sites of the molecule.

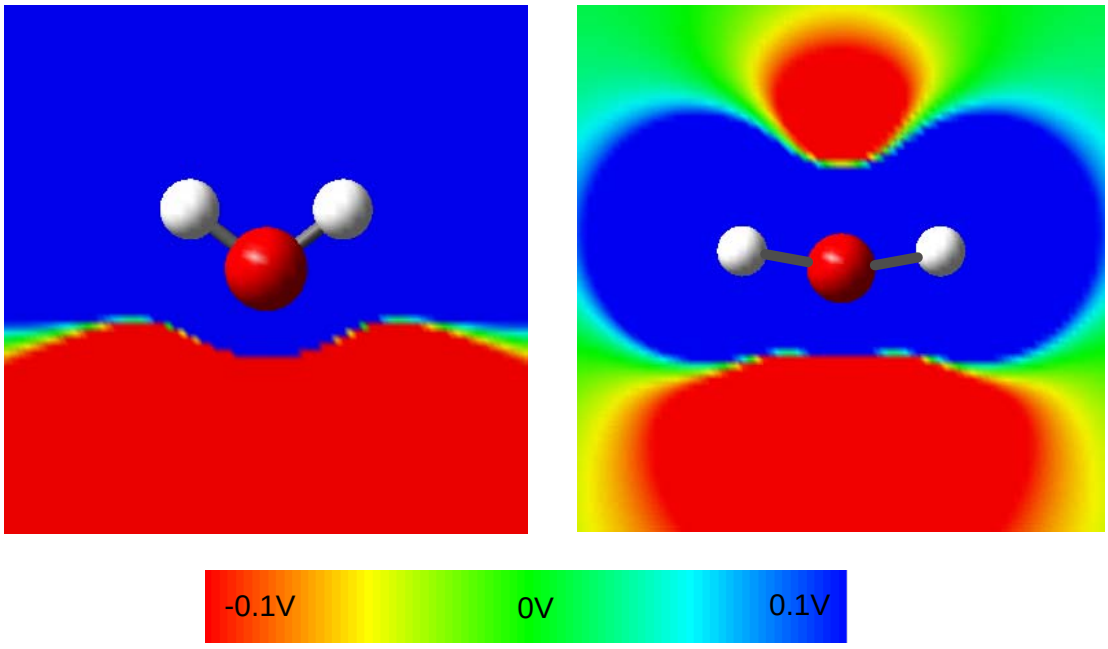

Figure 6.13. Molecular electrostatic potential*.

* Reprinted with permission from Jorge M. Seminario, Yuefei Ma, and Vandana Tarigopula, ***The NanoCell: A Chemically Assembled Molecular Electronic Circuit,*** IEEE Sensors J., In press.

The molecular electrostatic potential can be modified by external fields or excitations. For instance, the molecule triflourobenzene is excited by two water molecules conveniently located to produce four possible inputs Figure 6.14. Assuming a positive voltage is "1" and negative is "0". Then if we record the potential at the right site of the hydrogen atom, the truth table can be generated (Figure 6.15). Thus the molecular system performs as an AND gate.

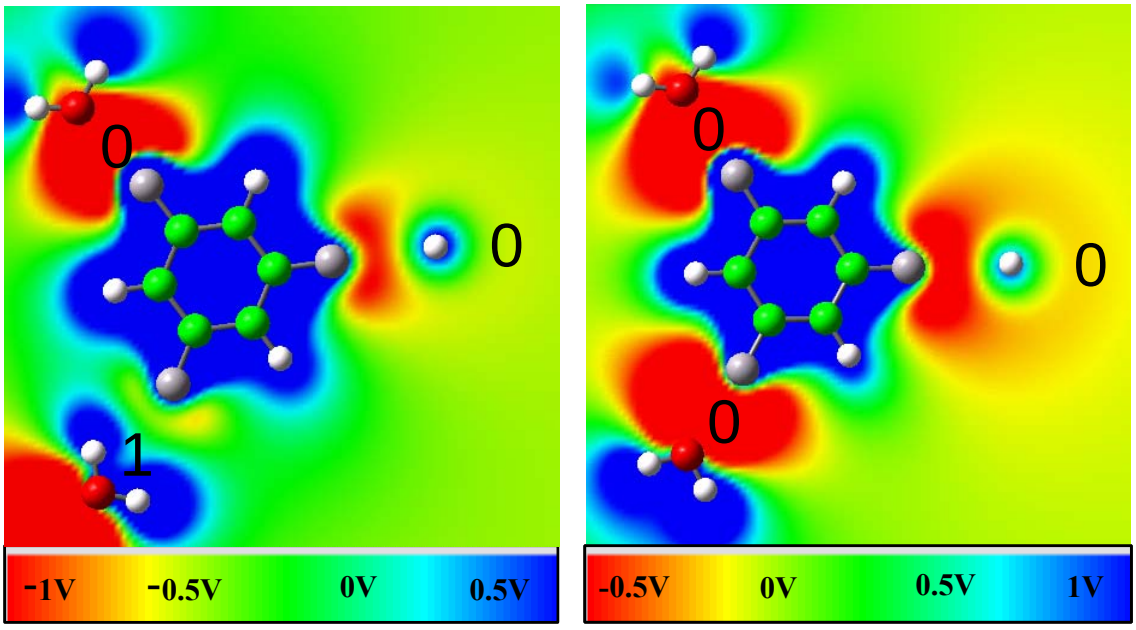

(a) **(b)**

Figure 6.14. The implementation of a logical AND using a tri-flourobenzene molecule*.

* Reprinted with permission from Jorge M. Seminario, Yuefei Ma, and Vandana Tarigopula, ***The NanoCell: A Chemically Assembled Molecular Electronic Circuit,*** IEEE Sensors J., In press. Copyright © [2006] IEEE.

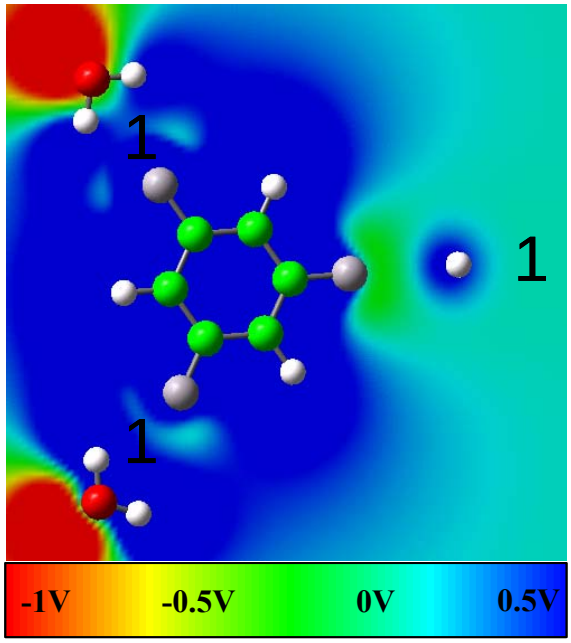

(c)

Figure 6.14 Continued

Input 1	Input 2	Output
1	1	1
1	0	0
0	1	0
0	0	0

Figure 6.15. Truth table of the molecular system shown in Figure 6.14

Additionally MEP can also be used to detect the existence of certain molecules. For example, when a molecule approaches to a MEP gate, the gate processes the information of the molecules and sends an electrical signal.

6.7 Implementation and application

It has been demonstrated that molecular vibrational modes can be used to transmit information while the signal can be processed using molecular electrostatic potential. Thus a complete device can be made if the two methods can be combined together. This could be done in practice by a femtosecond time-resolved laser, or the like.

It is demonstrated that both AM and FM can be used to transmit information in molecular wires using molecular vibrations with a power dissipation of ~50 nW when working at 1 Tbps. We also demonstrate that molecular wires using vibrational modes to transmit signals have very low power dissipation with respect to standard microelectronics devices.

These kinds of vibrational movements are at the range of terahertz. The vibrational modes can not only be excited by an electromagnetic wave, but also be detected using infrared (IR) spectroscopy or Raman spectroscopy if their movements cause changes in electrostatic dipole (IR active) or in polarizability (Raman active).

When the signal is transferred using molecular vibrational modes, the atoms vibrate to a certain position, which may introduce a change in the MEP distribution of the whole molecular system and this change is subsequently transferred through vibronics. Thus, a nanoCell device can be constructed with only molecules, as shown in Figure 6.16. By proper programming, the hundreds of molecules inside the nanoCell can be viewed as signal processing devices.

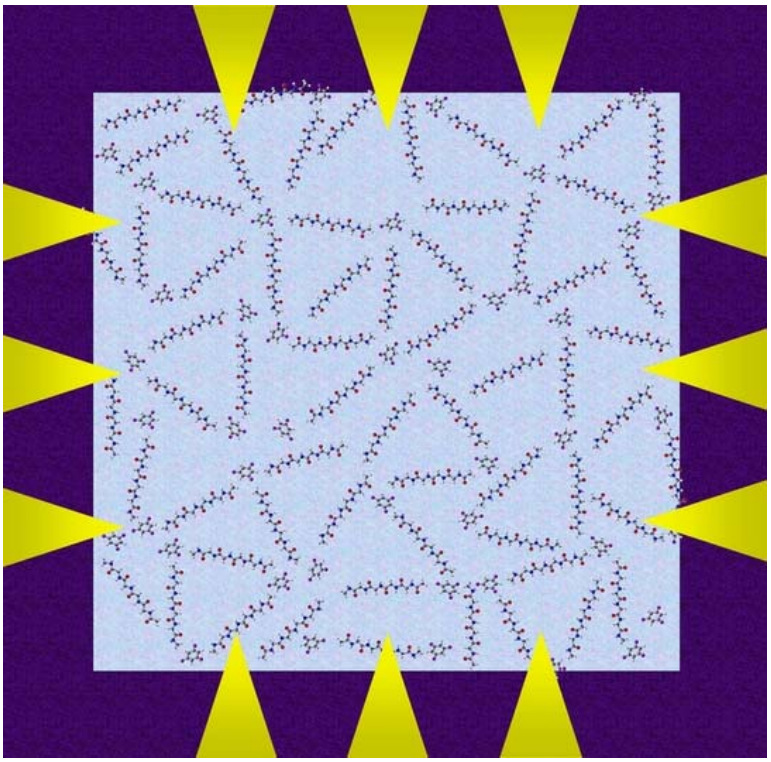

Figure 6.16. Proposed nanoCell with only molecules as the signal transmission and processing units.

If information is transmitted using vibronics, the power dissipation could be evaluated from the energy that excites and keeps the molecular wire to vibrate although you do not need energy for a molecule to vibrate in its stationary states; molecules vibrate even at 0 K. Our simulation shows that the molecular wire dissipates 0.321 eV for transmission one bit data using FM or 0.293 eV using AM. If the molecular wire transmits at 1 Tbps, the molecular wire will dissipate 51 nW using FM or 47 nW using AM, respectively.

Interestingly, the energy needed to excite the molecule with the two inputs is less than 0.5 eV. This implies that it may be possible to operate 200 million of these gates at 10 GHz frequency with just less than 1 Watt! More precisely,

$(2x10^8$ gates) $(10^{10}$ operation/s) (0.5 eV/gate-operation) $(1.6x10^9$ J/eV) = 0.16 J/s = 0.16 W.

This is certainly a rough estimate, most likely within the same order of magnitude of the exact value. This estimation considers the energy to change states of the gate and the energy to excite their inputs. As gates are directly interconnected, losses in interconnections are perhaps a small fraction of the energy to change states. Nevertheless, even an error of one or two orders of magnitude underestimating the power consumption still represents an excellent result. Using a similar logic to calculate the power needed in the modern Pentium XE, assuming a gate capacitance of 40 aF, amazingly yields 125 W (most likely a lucky match) to which we need to add the energy dissipation in the interconnects, the energy needed to change the input states, and the utilization factor among others; all these should account for the total 130 W dissipation in the microprocessor.

CHAPTER VII

CONCLUSION AND FUTURE RESEARCH

The research work presented in this dissertation focuses on the analysis of programmable molecular arrays, including theoretical study of single molecular conductance, electrical characterization of a nanoCell device, study of electron transport in discontinuous thin metal film as well as implementing molecular vibrational modes and molecular electrostatic potential as a methods to process and transfer information using programmable molecular arrays. This research represents a major contribution to an in-depth investigation of the implementation of programmable molecular arrays.

First, the limitations by conventional silicon based microelectronics in device fabrication and solid-state physics are outlined. New techniques such as single molecular electronic device, programmable molecular array and etc. are described that may help to overcome those limitations.

The first objective of investigation of programmable molecular array is to obtain the electrical conductance through single molecules. A number of experimental techniques for molecule conductance measurement are reviewed. Because of the large discrepancies between the experimental results, ab inito calculation based on density functional theory is used to calculate the single molecule conductance. The result shows a good match with the experimental results in the low voltage region.

The electrical characteristics of programmable molecular array are thoroughly studied. The distinct features of programmable molecular array include the memory and switching phenomena and start-up transitional behavior. Effects of deposition of different molecules are investigated. It is found that the OPE molecules interlinking the gold islands do not contribute significantly to the electrical conductance. However, the alkane molecules create additional barrier for the electron transport through the islands. A programming procedure for the multi-leads molecular array is proposed. In this method, a matrix of truth valued between each pair of the leads are obtained and followed by a set of voltage pulses to program the molecular array.

Since the OPE molecules are found not to contribute significantly to the electrical conductance of the programmable molecular array, it is obvious that the discontinuous gold film is the fundamental conductor. After reviews of several theoretical models that explain the electrical conductance through a discontinuous metallic film, a model based on the clustering effect of gold atoms are proposed to account for the electrical behavior of discontinuous gold film in high electrical field. At low field, however, electrons have not overcome the barrier imposed by electron activation energy. So the discontinuous gold film exhibits a predictable current-voltage behavior in low field.

Finally, it is proposed that in the programmable molecular array, the molecular vibronics and MEP could replace the charge-current approach to transport and process information. The result of the simulation is provided as a primary proof for the concept.

In addition, it is shown that the energy consumption using this approach is much smaller than the conventional charge-current based device.

Much remains to be done in this project of programmable molecular array. For instance, an effective electrical testing system has to be built to measure the conductances between each pair of the electrodes in the multi-leads programmable molecular array. Also, an electrical transducer need to be developed in order to realize vibronics in the programmable molecular array May this research work provide all of us several new ideas towards the realization of ultimate molecular computer in the future.

REFERENCES

(1) Moore, G. E. *Electronics* **1965**, *38*, 20.

(2) Moore, G. E. *Proc. SPIE* **1995**, 2437.

(3) Campbell, S. A. *The Science and Engineering of Microelectronic Fabrication*; Oxford University Press: New York, NY, 2001.

(4) Semiconductor Industry Association, International technology roadmap for semiconductors, http://www.itrs.net/Common/2005ITRS/ExecSum2005.pdf; 2005.

(5) Sze, S. M. *Physics of Semiconductor Devices*, 2nd ed.; Wiley: New York, 1981.

(6) Cilingiroglu, U. *Systematic Analysis of Bipolar and MOS Transistors*; Artech House: Norwood, MA 1993.

(7) Wheeler, J. A.; Zurek, W. *Quantum Theory and Measurement (Princeton Series in Physics*; Princeton Univ Pr, 1984.

(8) Aviram, A.; Ratner, M. A. *Chem. Phys. Lett.* **1974**, *29*, 277.

(9) Sharma, P. *Science* **2005**, *307*, 531.

(10) Wolf, S. A.; Awschalom, D. D.; R. A. Buhrman; Daughton, J. M.; Molnar, S. v.; Roukes, M. L.; Chtchelkanova, A. Y.; Treger, D. M. *Science* **2001**, *294*, 1488.

(11) Porath, D.; Bezryadin, A.; Vries, S. d.; Dekker, C. *Nature* **2000**, *403*, 635.

(12) Park, J.; Pasupathy, A. N.; Goldsmith, J. I.; Chang, C.; Yaish, Y.; Petta, J. R.; Rinkoski, M.; Sethna, J. P.; Abruna, H. D.; McEuen, P. L.; Ralph, D. C. *Nature* **2002**, *417*, 722.

(13) Xu, B.; Tao, N. J. *Science* **2003**, *301*, 1221.

(14) Cui, X. D.; Primak, A.; Zarate, X.; Tomfohr, J.; Sankey, O. F.; Moore, A. L.; Moore, T. A.; Gust, D.; Harris, G.; Lindsay, S. M. *Science* **2001**, *294*, 571.

(15) Mbindyo, J. K. N.; Mallouk, T. E.; Mattzela, J. B.; Kratochvilova, I.; Razavi, B.; Jackson, T. N.; Mayer, T. S. *J. Am. Chem. Soc.* **2002**, *124*, 4020.

(16) Selzer, Y.; Cai, L. T.; Cabassi, M. A.; Yao, Y. X.; Tour, J. M.; Mayer, T. S.; Allara, D. L. *Nano Lett.* **2005**, *5*, 61.

(17) Crommie, M. F.; Lutz, C. P.; Eigler, D. M. *Physical Review B* **1993**, *48*, 2851.

(18) Joachim, C.; Gimzewski, J. K. *Europhysics Letters* **1995**, *30*, 409.

(19) Joachim, C.; Gimzewski, J. K.; Schlittler, R. R.; Chavy, C. *Physical Review Letters* **1995**, *74*, 2102.

(20) Yazdani, A.; Eigler, D. M.; Lang, N. D. *Science* **1996**, *272*, 1921.

(21) Yazdani, A.; Jones, B. A.; Lutz, C. P.; Crommie, M. F.; Eigler, D. M. *Science* **1997**, *275*, 1767.

(22) Xu, B. Q.; Xiao, X. Y.; Yang, X.; Zang, L.; Tao, N. J. *J. Am. Chem. Soc.* **2005**, *127*, 2386.

(23) Bumm, L. A.; Arnold, J. J.; Cygan, M. T.; Dunbar, T. D.; Burgin, T. P.; Jones, L., II; Allara, D. L.; Tour, J. M.; Weiss, P. S. *Science* **1996**, *271*, 1705.

(24) Deegan, R. D.; Leheny, R. L.; Menon, N.; Nagel, S. R.; Venerus, D. C. *J. Phys. Chem. B* **1999**, *103*, 4066.

(25) Dorogi, M.; Gomez, J.; Osifchin, R.; Andres, R. P.; Reifenberger, R. *Physical Review B* **1995**, *52*, 9071.

(26) Andres, R. P.; Bein, T.; Dorogi, M.; Feng, S.; Henderson, J. I.; Kubiak, C. P.; Mahoney, W.; Osifchin, R. G.; Reifenberger, R. *Science* **1996**, *272*, 1323.

(27) Reed, M. A.; Zhou, C.; Muller, C. J.; Burgin, T. P.; Tour, J. M. *Science* **1997**, *278*, 252.

(28) Park, H.; Lim, A. K. L.; Alivisatos, A. P.; Park, J.; McEuen, P. L. *Appl. Phys. Lett.* **1999**, *76*, 301.

(29) Gittins, D. I.; Bethell, D.; Schiffrin, D. J.; Nichols, R. J. *Nature* **2000**, *408*, 67.

(30) Holmlin, R. E.; Haag, R.; Chabinyc, M. L.; Ismagilov, R. F.; Cohen, A. E.; Terfort, A.; Rampi, M. A.; Whitesides, G. M. *J. Am. Chem. Soc.* **2001**, *123*, 5075.

(31) Rampi, M. A.; Whitesides, G. M. *Chemical Physics* **2002**, *281*, 373.

(32) Holmlin, R. E.; Ismagilov, R. F.; Haag, R.; Mujica, V.; Ratner, M. A.; Rampi, M. A.; Whitesides, G. M. *Angewandte Chemie - International Edition* **2001**, *40*, 2316.

(33) Le, J. D.; He, Y.; Hoye, T. R.; Mead, C. C.; Kiehl, R. A. *Applied Physics Letters* **2003**, *83*, 5518.

(34) Slowinski, K.; Fong, H. K. Y.; Majda, M. *J. Am. Chem. Soc.* **1999**, *121*, 7257.

(35) Ralls, K. S.; Buhrman, R. A.; Tiberio, R. C. *Applied Physics Letters* **1989**, *55*, 2459.

(36) Zhou, C.; Deshpande, M. R.; Reed, M. A.; Jones, L.; Tour, J. M. *Applied Physics Letters* **1997**, *71*, 611.

(37) Wenyong, W.; Takhee, L.; Reed, M. A. *Physical Review B (Condensed Matter and Materials Physics)* **2003**, *68*, 035416.

(38) Chen, J.; Su, J.; Wang, W.; Reed, M. A. *Physica E: Low-dimensional Systems and Nanostructures* **2003**, *16*, 17.

(39) Wang, W.; Lee, T.; Reed, M. A. *J. Phys. Chem. B* **2004**, *108*.

(40) Lee, T.; Wang, W.; Klemic, J. F.; Zhang, J. J.; Su, J.; Reed, M. A. *J. Phys. Chem. B* **2004**, *108*, 8742.

(41) Yu, J.-S.; Kim, J. Y.; Lee, S.; Mbindyo, J. K. N.; Martin, B. R.; Mallouk, T. E. *Chem. Commun.* **2000**, *24*, 2445.

(42) Mbindyo, J. K. N.; Reiss, B. D.; Martin, B. R.; Keating, C. D.; Natan, M. J.; Mallouk, T. E. *Advanced Materials* **2001**, *13*, 249.

(43) Smith, P. A.; Nordquist, C. D.; Jackson, T. N.; Mayer, T. S.; Martin, B. R.; Mbindyo, J.; Mallouk, T. E. *Applied Physics Letters* **2000**, *77*, 1399.

(44) Fink, H. W.; Schonenberger, C. *Nature* **1999**, *398*, 407.

(45) Datta, S.; Tian, W. D.; Hong, S. H.; Reifenberger, R.; Henderson, J. I.; Kubiak, C. P. *Physical Review Letters* **1997**, *79*, 2530.

(46) Seminario, J. M.; Zacarias, A. G.; Tour, J. M. *J. Phys. Chem. A* **1999**, *103*, 7883.

(47) Derosa, P. A.; Seminario, J. M. *J. Phys. Chem. B* **2001**, *105*, 471.

(48) Seminario, J. M.; Zacarias, A. G.; Derosa, P. A. *The Journal of Chemical Physics* **2002**, *116*, 1671.

(49) Yan, L.; Seminario, J. M. *J. Phys. Chem. A* **2005**, *109*, 6628.

(50) Tour, J. M.; Reed, M. A.; Seminario, J. M.; Allara, D. A.; Weiss, P. A. Molecular Computer. In *US Patent 6,430,511*, 2002.

(51) Tour, J. M. *Molecular Electronics. Commercial Insights, Chemistry, Devices, Architecture and Programming*; World Scientific: New Jersey, 2003.

(52) Tour, J. M.; VanZandt, W. L.; Husband, C. P.; Husband, S. M.; Wilson, L. S.; Franzon, P. D.; Nackashi, D. P. *IEEE Trans. Nanotech.* **2002**, *1*, 100.

(53) Tour, J. M.; Cheng, L.; Nackashi, D. P.; Yao, Y.; Flatt, A. K.; St. Angelo, S. K.; Mallouk, T. E.; Franzon, P. D. *J. Am. Chem. Soc.* **2003**, *125*, 13279.

(54) Seminario, J. M.; Cordova, L. E.; Derosa, P. A. *Proc. IEEE* **2003**, *91*, 1958.

(55) Seminario, J. M.; Zacarias, A. G.; Derosa, P. A. *J. Phys. Chem. A* **2001**, *105*, 791.

(56) Seminario, J. M.; Zacarias, A. G.; Tour, J. M. *J. Am. Chem. Soc.* **1999**, *121*, 411.

(57) Derosa, P. A.; Guda, S.; Seminario, J. M. *J. Am. Chem. Soc.* **2003**, *125*, 14240.

(58) Seminario, J. M.; Ma, Y.; Tarigopula, V. *IEEE Sensors* In Press.

(59) Nackashi, D. P.; Di Spigna, N. H.; Winick, D. A.; Amsinck, C. J.; Cheng, L.; Tour, J. M.; Franzon, P. D. *Technical Proceedings of the 2004 NSTI Nanotechnology Conference and Trade Show, Nanotech* **2004**, *3*, 45.

(60) Chen, J.; Wang, W.; Reed, M. A.; Rawlett, A. M.; Price, D. W.; Tour, J. M. *Appl. Phys. Lett.* **2000**, *77*, 1224.

(61) Chen, J.; Reed, M. A.; Rawlett, A. M.; Tour, J. M. *Science* **1999**, *286*, 1550.

(62) Husband, C. P.; Husband, S. M.; Daniels, J. S.; Tour, J. M. *IEEE Trans. Electron Dev.* **2003**, *50*, 1865.

(63) Cai, L.; Yao, Y.; Yang, J.; Price, D. W. J.; Tour, J. M. *Chem. Mater.* **2002**, *14*, 2905.

(64) Kluth, G. J.; Sung, M. M.; Maboudian, R. *Langmuir* **1997**, *13*, 3775.

(65) Seminario, J. M.; Ma, Y.; Agapito, L. A.; Yan, L.; Araujo, R. A.; Bingi, S.; Vadlamani, N. S.; Chagarlamudi, K.; Sudarshan, T. S.; Myrick, M. L.; Colavita, P. E.; Franzon, P. D.; Nackashi, D. P.; Cheng, L.; Yao, Y.; Tour, J. M. *J. Nanosci. Nanotech.* **2004**, *4*, 907.

(66) Bashara, N. M.; Weitzenkamp, L. A. *Journal of Applied Physics* **1964**, *35*, 1983.

(67) Dobson, P. J.; Hopkins, B. J. *Journal of Applied Physics* **1968**, *39*, 3074.

(68) Kiernan, R.; Stops, D. W. *Nature* **1969**, *224*, 907.

(69) Morris, J. E. *Thin Solid Films* **1972**, *11*, 81.

(70) Neugebauer, C. A.; Webb, M. B. *Journal of Applied Physics* **1962**, *33*, 74.

(71) Hill, R. M. *Proc. R. Soc. London, Ser. A* **1969**, *309*, 377.

(72) Hill, R. M. *Proc. R. Soc. London, Ser. A* **1969**, *309*, 397.

(73) Uozumi, K.; Nishiura, M.; Kinbara, A. *J. Appl. Phys.* **1977**, *48*, 818.

(74) Uozumi, K. *Thin Solid Films* **1979**, *57*, 141.

(75) Uozumi, K. *Thin Solid Films* **1981**, *89*, 45.

(76) Shin, M.; Lee, S.; Park, K. W.; Lee, E.-H. *Phys. Rev. Lett.* **1998**, *80*, 5774–5777.

(77) Shin, M.; Lee, S.; Park, K. W.; Lee, E. *Phys. Rev. B* **1999**, *59*, 3160.

(78) Amman, M.; Ben-Jacob, E.; Mullen, K. *Physics Letters A* **1989**, *142*, 431.

(79) Hu, G. Y.; O'Connell, R. F. *Phys. Rev. B* **1994**, *49*, 16773–16776.

(80) Whan, C. B.; White, J.; Orlando, T. P. *Applied Physics Letters* **1996**, *68*, 2996.

(81) Likharev, K. K.; Matsuoka, K. A. *Applied Physics Letters* **1995**, *67*, 3037.

(82) Shin, M.; Lee, S.; Park, K. W.; Lee, E.-H. *Journal of Applied Physics* **1998**, *84*, 2974.

(83) Simmons, J. G.; Verderber, R. R. *Proc. R. Soc. London, Ser. A* **1967**, *301*, 77.

(84) Cimrová, V.; Neher, D. *Synth. Met.* **1996**, *76*, 125.

(85) Kusano, H.; Shiraishi, N.; Hosaka, S.; Kuruma, I.; Kitagawa, M.; Ichino, K.; Kobayashi, H. *Synth. Met.* **1997**, *91*, 341.

(86) Manca, J.; Bijnens, W.; Kiebooms, R.; D'Haen, J.; D'Olieslaeger, M.; Wu, T.; Ceuninck, W. d.; Schepper, L. d.; Vanderzande, D.; Gelan, J.; Stals, L. *Opt. Mater.* **1998**, *9*, 134.

(87) Berleb, S.; Brütting, W.; Schwoerer, M. *Synth. Met.* **1999**, *102*, 1034.

(88) Xu, X.; Yin, S.; Kong, F.; Zhang, F.; Yao, K.; Huang, W. *J. Polym. Sci., Part B: Polym. Phys.* **2001**, *39*, 589.

(89) Lebedev, E.; Forero, S.; Brütting, W.; Schwoerer, M. *Synth. Met.* **2000**, *111-112*, 345.

(90) Ma, L.; Liu, J.; Pyo, S.; Yang, Y. *Appl. Phys. Lett.* **2002**, *80*, 362.

(91) Ma, L.; Xu, Q.; Yang, Y. *Appl. Phys. Lett.* **2004**, *84*, 4908.

(92) Ma, L.; Liu, J.; Yang, Y. *Appl. Phys. Lett.* **2002**, *80*, 2997.

(93) Ma, L.; Pyo, S.; Ouyang, J.; Xu, Q.; Yang, Y. *Appl. Phys. Lett.* **2003**, *82*, 1419.

(94) Bozano, L. D.; Kean, B. W.; Deline, V. R.; Salem, J. R.; Scott, J. C. *Appl. Phys. Lett.* **2004**, *84*, 607.

(95) Brütting, W.; Riel, H.; Beierlein, T.; Riess, W. *J. Appl. Phys.* **2001**, *89*, 1704.

(96) Tang, W.; Shi, H.; Xu, G.; Ong, B. S.; Popovic, Z. D.; Deng, J.; Zhao, J.; Rao, G. *Advanced Materials* **2005**, *17*, 2307.

(97) Thomas, R. E.; Rosa, A. J. *The Analysis and Design of Linear Circuits*; John Wiley & Sons: New York, NY, 2003.

(98) Singer, M. Intel Expanding Moore's Law with Nano, http://www.internetnews.com/infra/article.php/1462171, 2002.

(99) Seminario, J. M.; Araujo, R. A.; Yan, L. *J. Phys. Chem. B* **2004**, *108*, 6915.

(100) Seminario, J. M.; Ma, Y.; Agapito, L. A.; Yan, L.; Araujo, R. A.; Bingi, S.; Vadlamani, N. S.; Chagarlamudi, K.; Sudarshan, T. S.; Myrick, M. L.; Colavita, P. E.; Franzon, P. D.; Nackashi, D. P.; Cheng, L.; Yao, Y.; Tour, J. M. *J. Nanoscience Nanotech.* **2004**, *4*, 907.

(101) Seminario, J. M.; Yan, L.; Ma, Y. *Proc. IEEE* **2005**, *93*, 1753.

(102) Gurrum, S. P.; Suman, S. K.; Joshi, Y. K.; Fedorov, A. G. *IEEE Transactions on Device and Materials Reliability* **2004**, *4*, 709.

(103) Allen, M. P.; Tildesley, D. J. *Computer Simulation of Liquids*; Clarendon Press: Oxford, 1990.

(104) Seminario, J. M.; Derosa, P. A.; Bozard, B. H.; Chagarlamudi, K. *J. Nanoscience Nanotech* **2005**, *5*, 1.

(105) Yan, L.; Ma, Y.; Seminario, J. M. *Int. J. High Speed Electronics Syst.* In Press.

(106) Seminario, J. M.; Derosa, P. A.; Cordova, L. E.; Bozard, B. H. *IEEE Trans. Nanotech.* **2004**, *3*, 215.

(107) Seminario, J. M. “Molecular Devices Operating at Terahertz Frequencies: Theoretical Simulations and Perspectives”; Proc. SPIE, 2004.

(108) Haile, J. M. *Molecular Dynamics Simulation*; J. Wiley & Sons, Inc: New York, 1992.

(109) Hockney, R. W. *Methods Comput. Phys.* **1970**, *9*, 136.

(110) Ifeachor, E. C.; Jervis, B. W. *Digital Signal Processing: A Practical Approach*, Second Edition ed.; Pearson Education Limited: Essex, England, 2002.

(111) McClellan, J. H.; Schafer, R. W.; Yoder, M. A. *DSP First: A Multimedia Approach*; Tom Robbins: Terre Haute, IN, 1998.

(112) Integrated Publishing, FM Demodulation; http://www.tpub.com/neets/book12/51c.htm; 2005.

(113) Levine, I. N. *Quantum chemistry*; Prentice-Hall, 2000.

(114) Labview, Analysis Concepts. In *National Instruments*, 2004.

APPENDIX A

LABVIEW PROGRAM FOR VIBRONICS DIGITAL SIGNAL PROCESSING

A.1 Program selection

In molecular vibronics simulation, there are several options to implement digital signal processing to recover the injected signal. Microsoft Excel is a handy software. However, it only loads up to 65,536 data points, which is far less than our requirement of over 1,000,000. Origin is another choice. But its signal processing ability is very limited. Matlab is a powerful software, but it is based on UNIX system which makes it inconvenient to visualize the result and modify the program immediately after. This would inevitably prolong the feedback-loop time and reduces the programming efficiency. Finally we choose Labview. This software has a large collection of signal processing tools. Also, its user friendly graphical development environment makes it easy to accomplish our task.

A.2 Recovering amplitude modulated signal

Figure A.1 shows the front panel of the Labview program for amplitude modulated signal recovering. As in any computer program, it consists of input section and output sections. The user needs specify:

(1) Name and location of the file that contains the trajectory data, i.e., the time series of bond length;

(2) Name and location of the output file;

(3) Sampling interval, i.e., the time steps that has been used to record the trajectory data;

(4) Number of data has been recorded;

(5) Index and length of the data the user needs to analyze;

(6) Cut-off frequencies for the bandpass filter and lowpass filter.

Because the fast Fourier transform of the trajectory data is needed for the selection of cut-off frequencies, the last two inputs are specified during the program is running, instead of before the program starts.

The output signals are visualized in the front panel as well.

The program is constructed using a sequence structure in which each diagram, or frame, executes sequentially. This structure is chosen because of its ease of data manipulation.

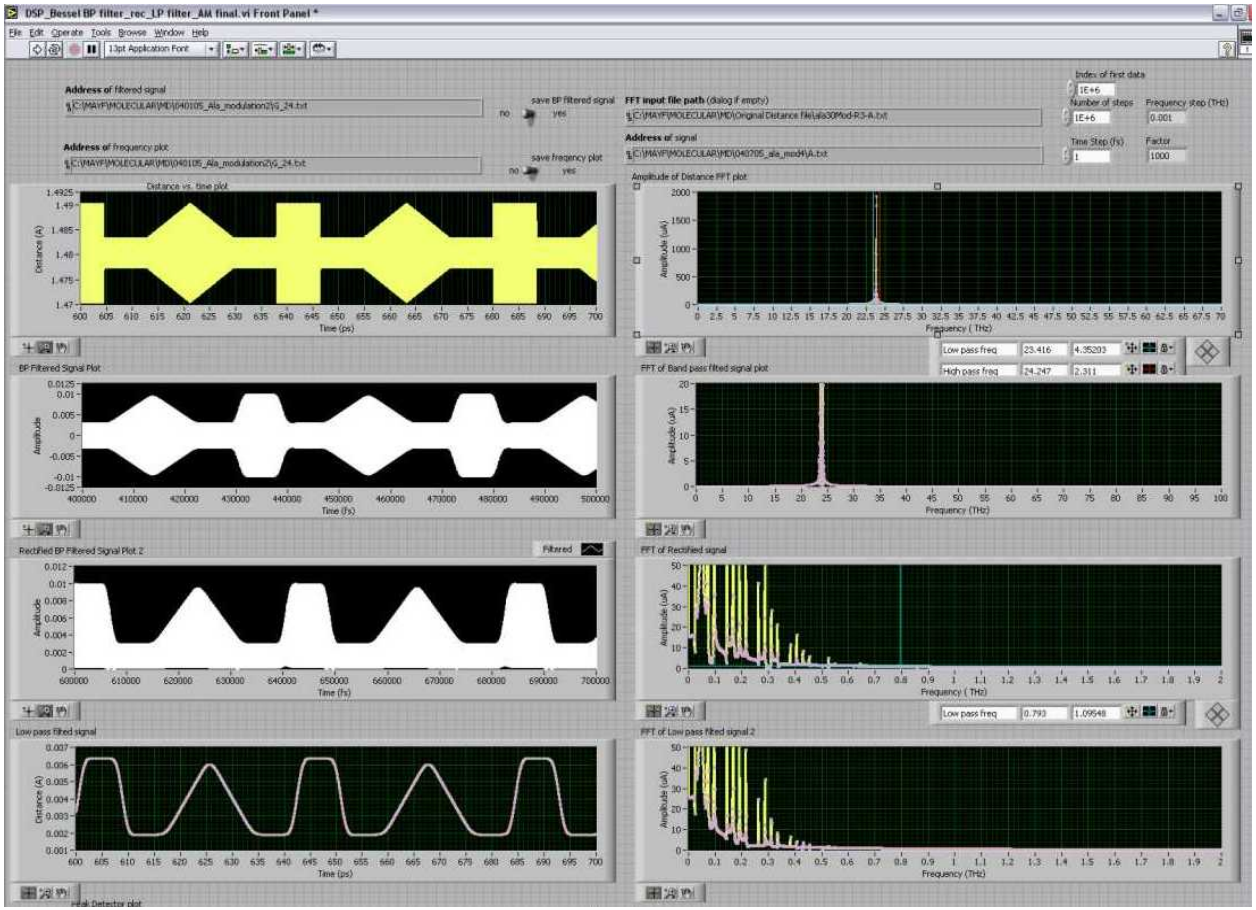

Figure A.1 Front panel of Labview program to recover amplitude modulated signal. The input fields are located on the top of the panel; the output time-domain signals (lower left) and their corresponding frequency domain signals (lower right) are shown.

Figure A.2 shows the first diagram which primarily prepares the data for analyze. In this diagram, the program reads the data from the appointed file and transforms it into a one-dimensional array. It is preferable to skip the initial part of the signal since it may contain excessive noise due to large vibration. The DC series of the data, i.e., the mean value is extracted from the data so that only the AC signal is remained. Frequency spacing Δf is also calculated in this diagram:

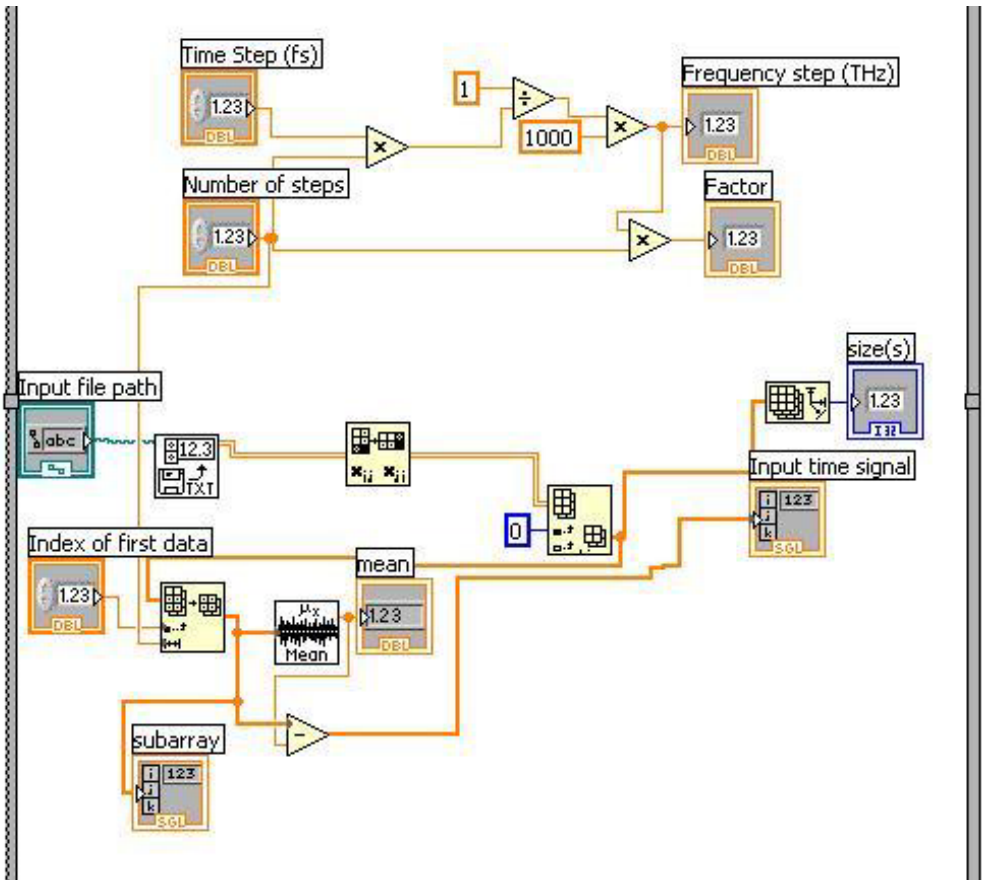

Figure A.2 Diagram 1 for data preparation.

$$\Delta f = \frac{1}{N \cdot \Delta t} \tag{A.1}$$

where Δf is the frequency resolution, N is the number of data and Δt is the sampling interval.

Diagram 2 (Figure A.3) plots the data in a form of waveform graph. The resulting plot is shown as the first one in the left column of Figure A.1.

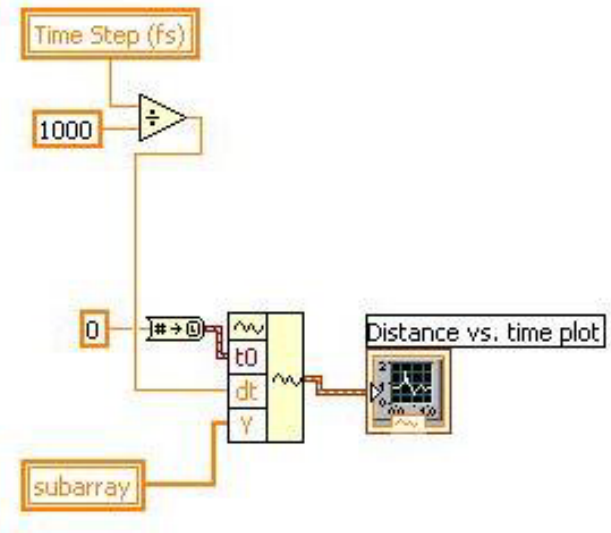

Figure A.3 Diagram 2 to plot time domain signal.

Diagram 3 (Figure A.4) computes the fast Fourier transform (FFT) of the input AC data. Using AC data, instead of the original data, as an input, ensures that the first element of the generated frequency-domain array is zero [114]. The output from the FFT sub-program is an array of complex number. The amplitude is calculated and plotted in a waveform graph.

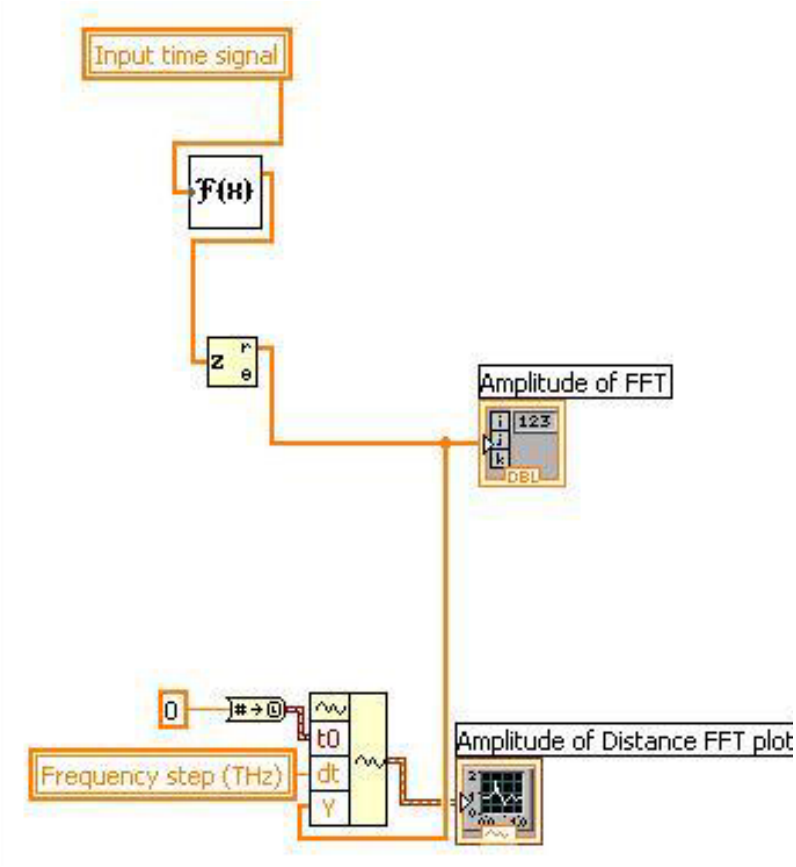

Figure A.4 Diagram 3 for FFT.

The next two diagrams (Figure A.5) perform the bandpass filtering of the input AC data. The user needs to manually select the cut-off frequencies of the bandpass filter by dragging the vertical cursors in the interactive graph of the frequency domain signal (Figure A.6a). The values of the cut-off frequencies, which are indicated below the graph, are inputted into the Bandpass sub-program, whose front panel is shown in Figure A.6b.

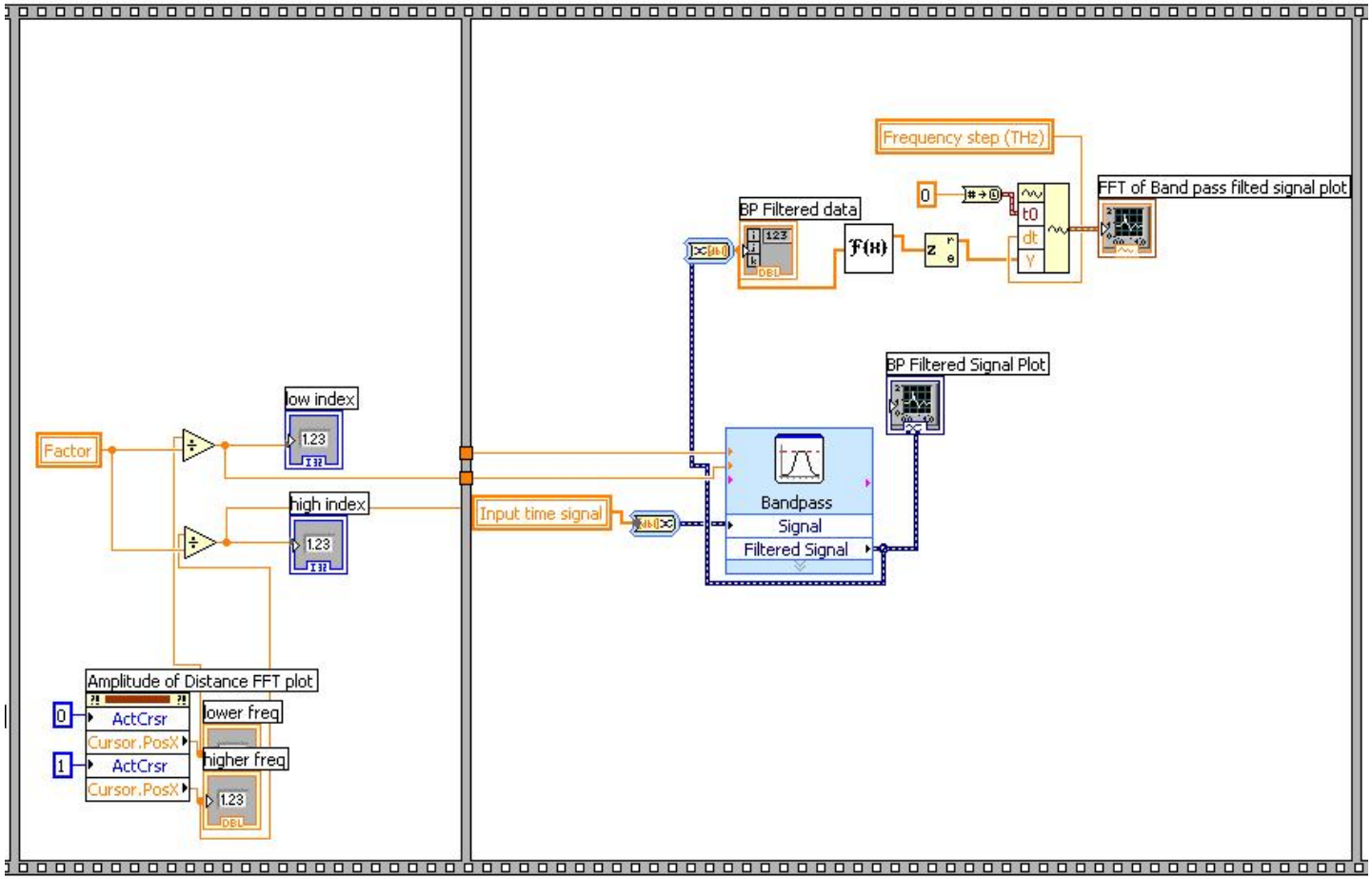

Figure A.5 Diagram 4 and 5 for bandpass filtering the input AC data.

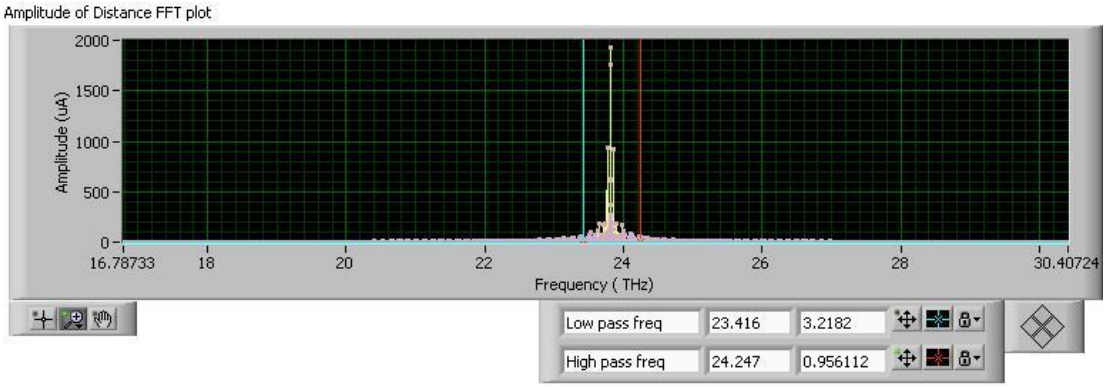

(a)

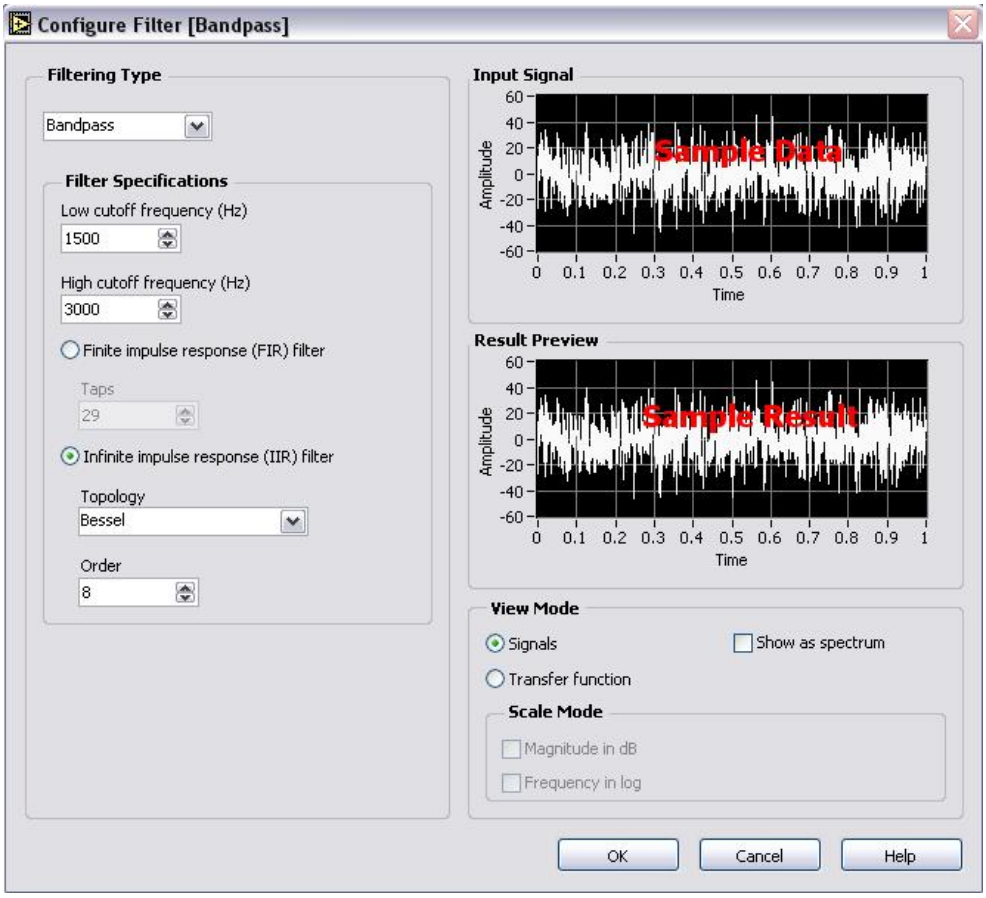

(b)

Figure A.6 Implementation of bandpass filter. (a) Interactive plot of frequency domain AC data; (b) front panel of the bandpass sub-program.

When we design the bandpass filter, we tried several topologies and choose the one that best resemble the original data. Figure A.7 gives some examples. The infinite impulse response (IIR) Bessel filter turns out to be the right choice, since it has maximally flat response in both magnitude and phase and nearly linear-phase response in the passband [114].

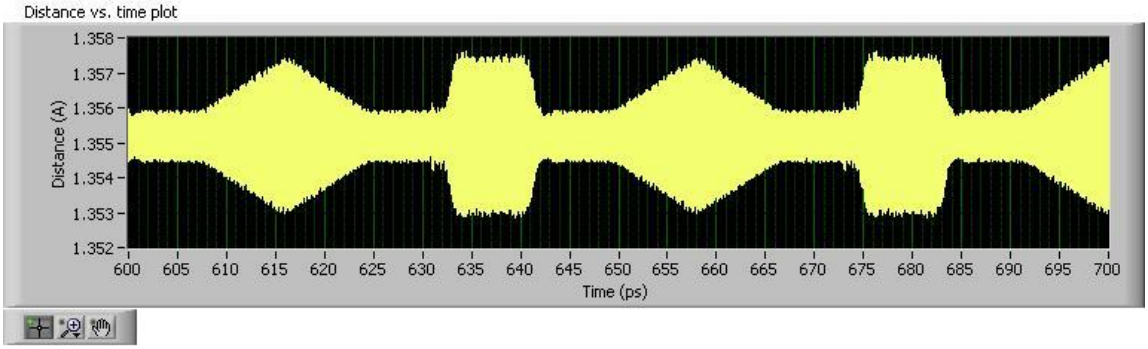

(a)

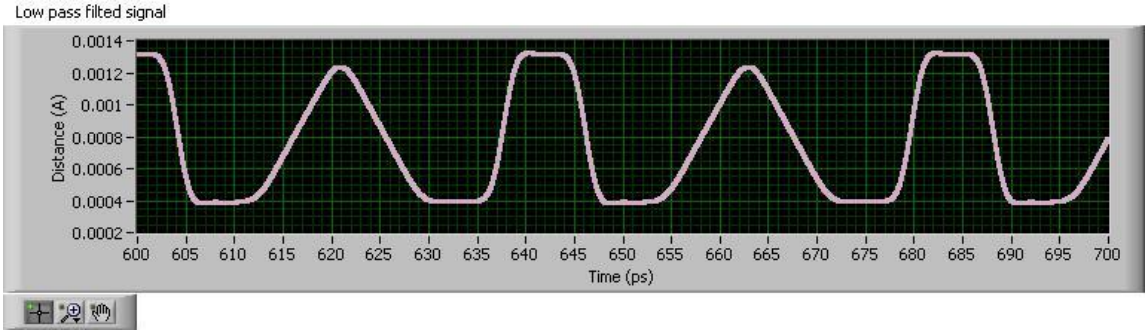

(b)

Figure A.7 Effects of different bandpass filter on output signal. (a) Input signal; (b) output signal from Bessel filter; (c) Butterworth filter; (d) Chebyshev filter; (e) Elliptic filter; (f) Finite impulse response (FIR) filter.

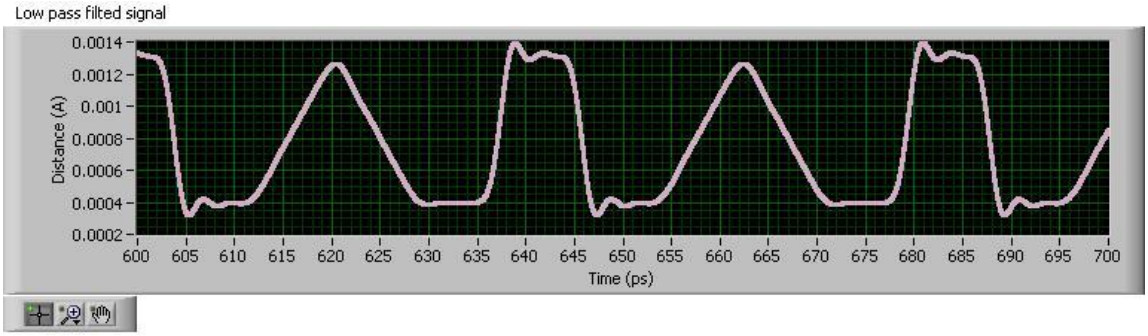

(c)

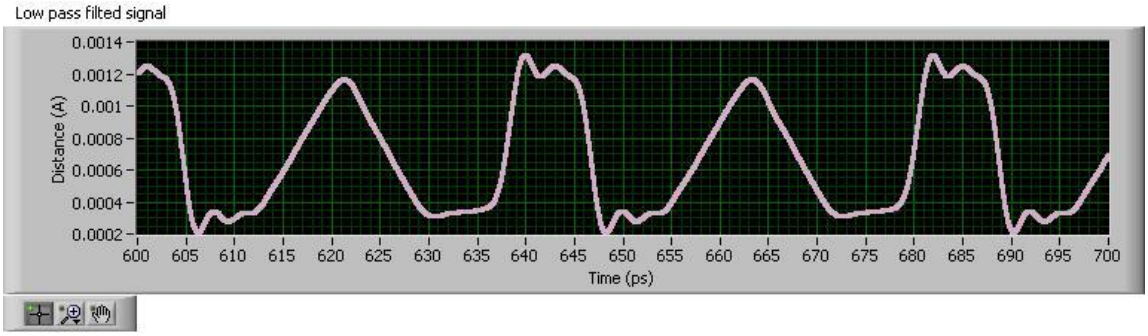

(d)

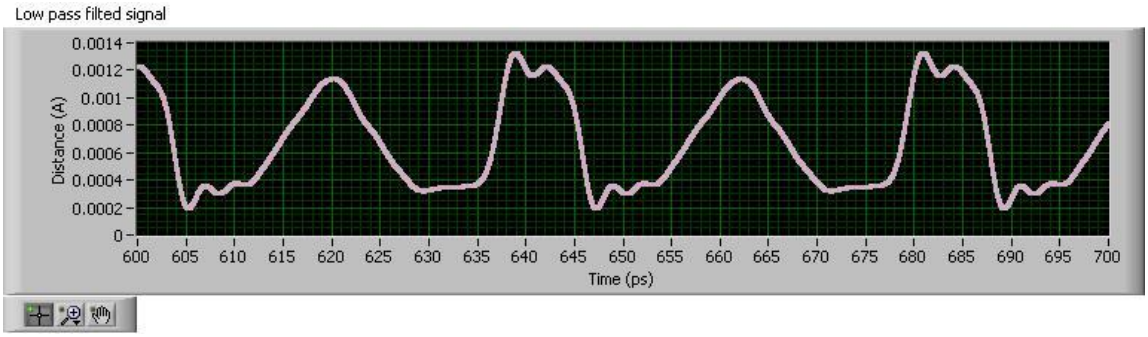

(e)

Figure A.7 (Continued)

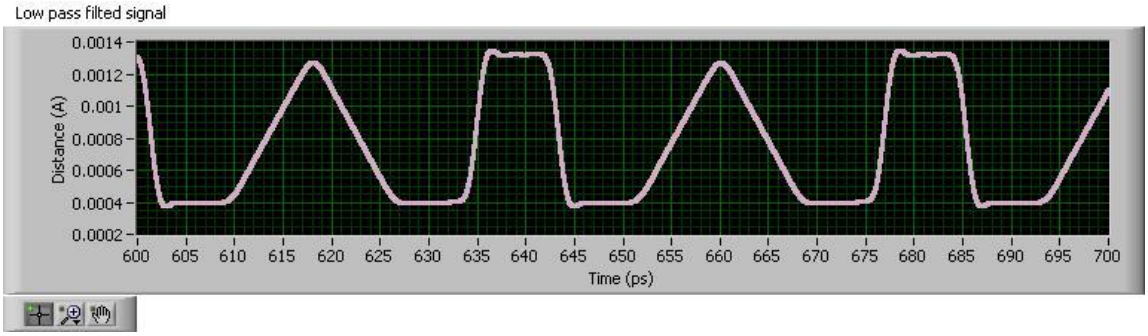

(f)

Figure A.7 (Continued)

Diagram 6 (Figure A.8) performs the rectification of the bandpassed signal. The rectification is realized by simply using a sub-program which returns the absolute value of each data point.

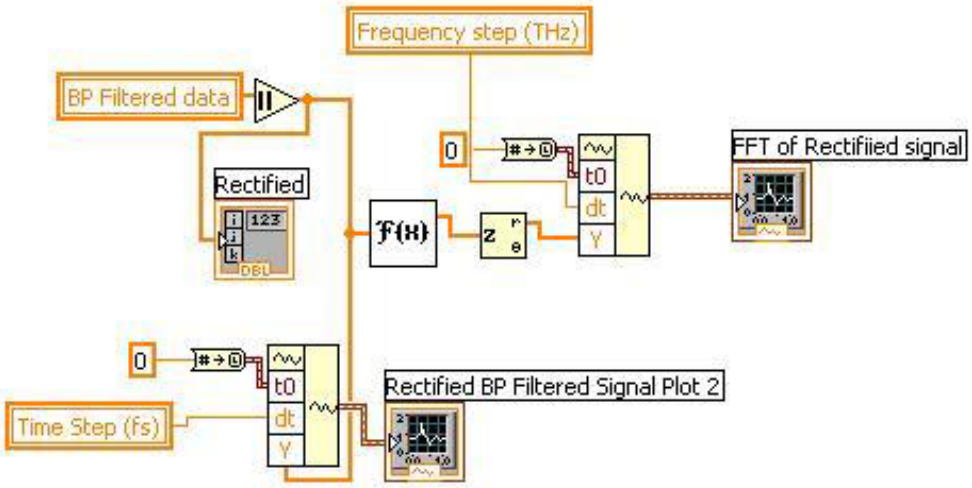

Figure A.8 Diagram 6 for signal rectification.

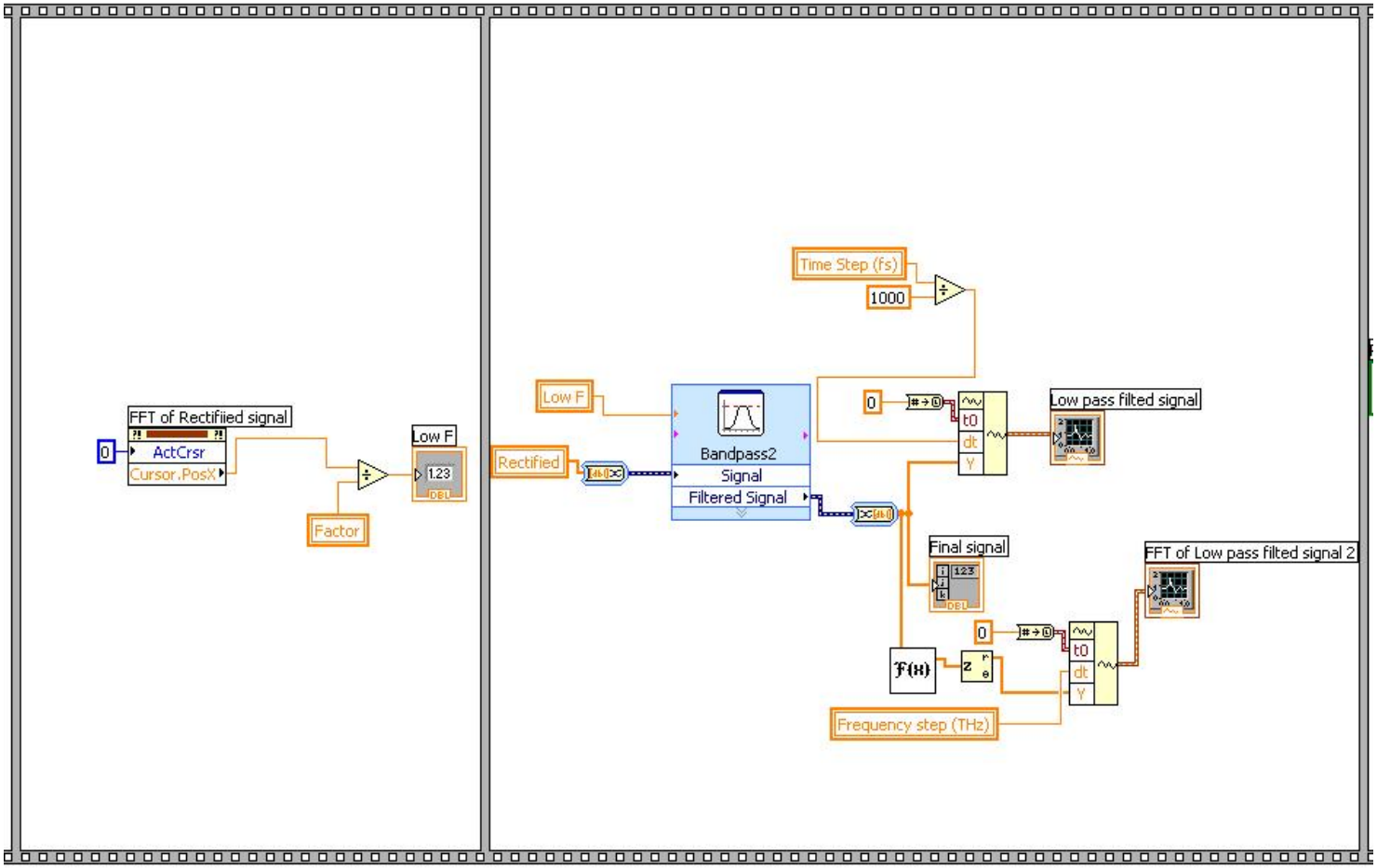

Figure A.9 Diagram 7 and 8 for lowpass filtering the rectified signal.

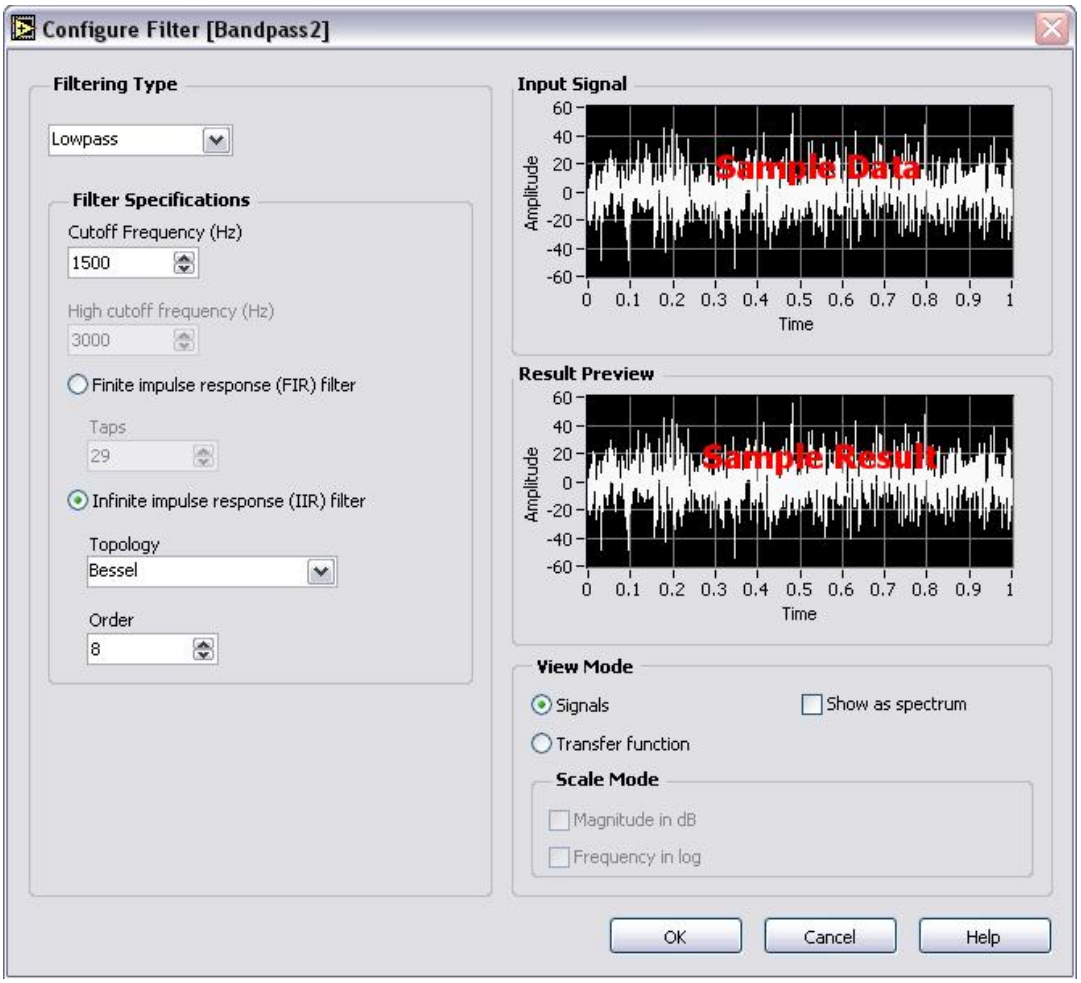

Figure A.10 Front panel of the lowpass sub-program.

Diagram 7 and 8 perform the lowpass filtering of the rectified signal (Figure A.10). This is similar to the bandpass filter in diagram 4 and 5. The topology of the lowpass filter is also the Bessel IIR filter. The difference is that the user only needs to select the high frequency limit for the filter.

The lowpass filtering can be replaced by a peak detector (Figure A.11) which finds the location and amplitude of the input signal. The resulting signal is similar to the lowpass filtered signal.

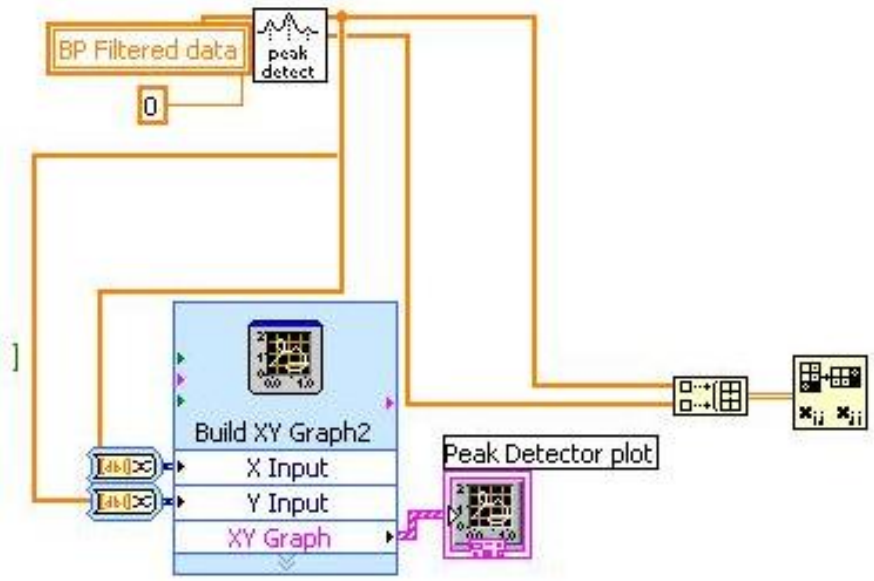

Figure A.11 Diagram for peak detector.

The last diagram (Figure A.12) saves the recovered signal to assigned location. It also provides other options to save more data. The saving option is realized by a case structure which is controlled by the switches located on the upper left of the front panel.

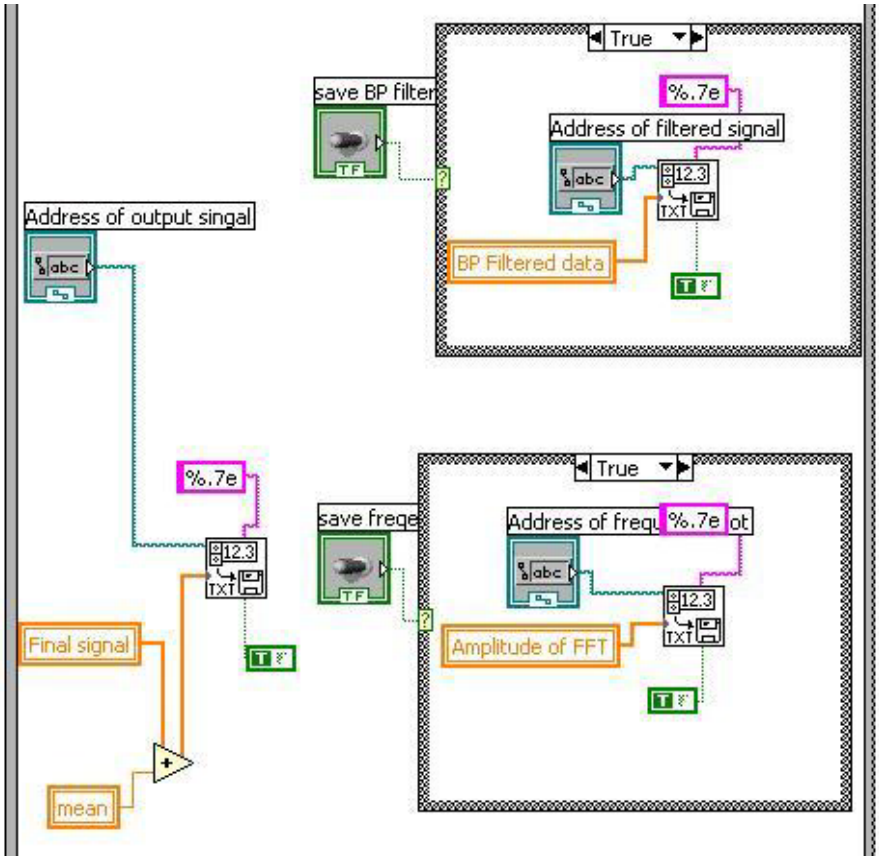

Figure A.12 Diagram 9 to save data.

A.3 Recovering frequency modulated signal

The Labview program to recover the frequency modulated signal is essentially similar to the amplitude modulated one with two additional steps. The first one is a clipper after the bandpass filter to eliminate excessive noise. The clipper is realized by a sub-program which clips the elements to within the boundary defined by upper and

lower limits (Figure A.13). The limits are set by the user in interactive waveform graph. If x_i represents the original data, a and b represents the upper and lower limits, respectively, the clipped data y_i is

$$y_i = \begin{cases} a & x_i > a \\ x_i & b < x_i < a \\ b & x_i < b \end{cases} \tag{A.2}$$

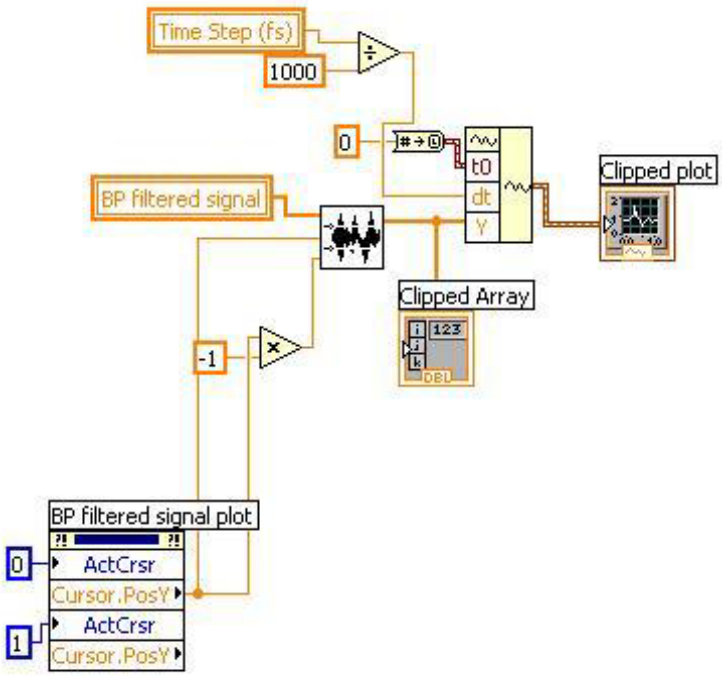

Figure A.13 Diagram of a clipper.

After the clipper, there is a demodulator to demodulate the frequency modulated signal. The demodulator is basically a Bessel bandpass filter. The difference between this filter and the filters in the previous section is that it has different center and bandwidth. Frequency response of the filter is necessary to find the correct bandwidth and center. Figure A.14 shows the Labview program for obtaining frequency response. By varying the frequency of the input sinusoidal signal, the amplitude of the filtered signal is recorded and plotted versus the input frequency.

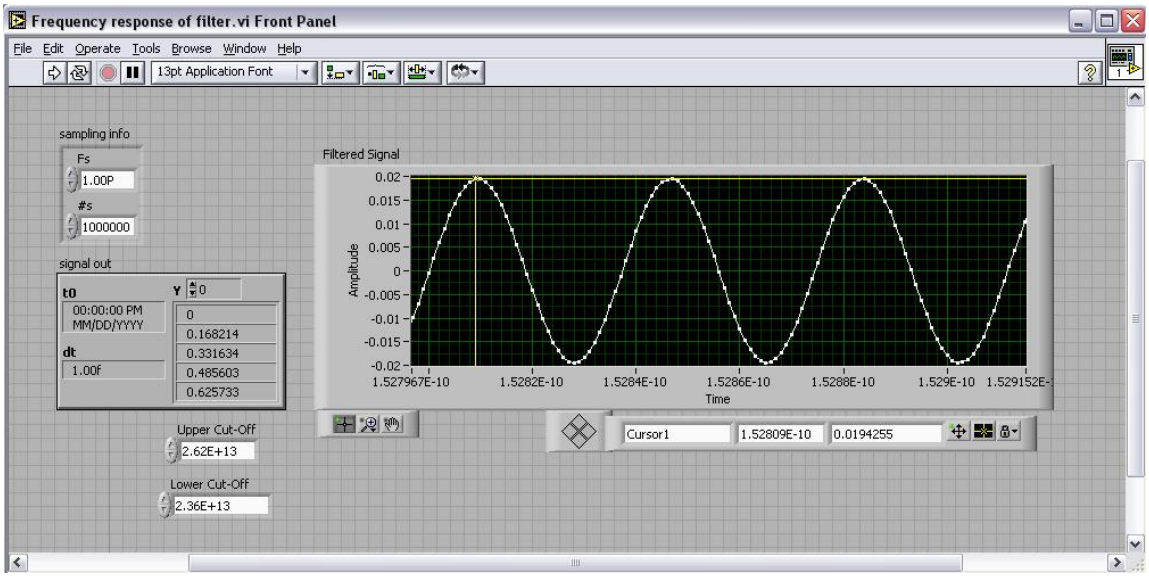

Figure A.14 Front panel of Labview program for obtaining the frequency response of a bandpass filter.

VITA

Yuefei Ma, was born in Beijing, People's Republic of China in 1977. She received the B.S. degree in material science from Fudan University, Shanghai, China, in 1999 and the M.S. degree in electrical engineering from the University of South Carolina, in 2004. Since 2003, she has been a research assistant at the Molecular & Nano Electronics group. From 1999 to 2001, she worked as a process engineer in Advanced Semiconductor Manufacturing Corp. in Shanghai. She received her Ph.D. in electrical engineering from Texas A&M university in May 2006. Her current research interests include molecular electronic device fabrication and testing.